The Connections Between Spatial and Temporal Variations of Hydrodynamic Conditions and Deposition Across a Marsh Surface Restored through Managed Realignment

By
Megan Elliott

A Thesis Submitted to
Saint Mary's University, Halifax, Nova Scotia
in Partial Fulfillment of the Requirements for
the Degree of Master of Science in Applied Science

April, 2023, Halifax, Nova Scotia

Copyright Megan Elliott, 2023

Approved: Dr. Danika van Proosdij
Supervisor
Department of Geography and Environmental Studies

Approved: Dr. Jeremy Lundholm
Supervisor Committee Member
Department of Biology

Approved: Timothy Milligan
Supervisor Committee Member
Faculty of Graduate Studies
Dalhousie University

Approved: Dr. Jeff Ollerhead
External Examiner
Department of Geography and Environment
Mount Allison University

Date: April 25, 2023

The Connections Between Spatial and Temporal Variations of Hydrodynamic Conditions and Deposition Across a Marsh Surface Restored through Managed Realignment

by Megan Elliott

Abstract

As sea levels rise and coastal flooding increases, our current hard engineering sea defences will get increasingly expensive to maintain. Nature-based solutions, such as salt marsh restoration with the managed realignment (MR) of dykelands, have the ability to provide flood protection as sea levels rise. This thesis measured hydrologic variables and sediment parameters across a MR site located within the Chignecto Isthmus in the Bay of Fundy. This data was used in conjunction with marsh surface data from a co-occurring study, Lewis (2022), to link site inlet conditions to surface sediment deposition. Varying hydrologic and topographic factors interacted, creating the spatiotemporal deposition patterns measured. These interactions guided statistical models of deposition prediction, which were assessed for their practicality and accuracy. This research will inform future MR restoration trajectory models.

April 25, 2023

Acknowledgements

First, I want to thank my supervisor, Danika whom I received all the support, guidance, and kindness I could have asked for from these past years. I want to thank Jeremy for his support on my supervisory committee and all the help with the statistics and modelling and helping me learn how to program in R. I want to thank Tim for all the help and guidance as a supervisor committee member and for being one of the reasons I pursued a masters after teaching me about flocs and the LISST instrument. I was very fortunate to have such support and kindness from my committee.

I want to thank Emma Poirier for being such a great lab supervisor and teaching me so much in the lab and in the field and always being there to help. I want to thank Samantha Lewis for ArcGIS help and being a great field buddy. Thank you, Julia, for the help with the ISCO plots and help with your ADV scripts. I also wouldn’t have most of the salt marsh plant knowledge I do if I hadn’t been able to tag along for Tasha’s data collection, or the accretion knowledge from helping with the RSET and marker horizon data collection with the CBWES team. I want to thank Greg Baker for technical support with the RTK, ArcGIS, and sparc7 and to Jubin Thomas for creating the wind rose tutorial. I also gained GIS mapping knowledge from Cam Lirette while working for SWEPS during my co-op term. I also wanted to thank all the others I had the privilege of getting to know and received help from in the field and lab including Élise, Maka, Sade, Brandon, Kayla, Caytlyn, Riccardo, Anna, Moira, and Chaz, and for being a part of the family with the rest of the In_Coast and associated teams.

I thank the Natural Sciences and Engineering Research Council (NSERC) for funding this research. Thank you to the Fred Smithers Center for assisting me on a huge part of my journey to discovering more about myself and becoming a better student and employee.

I want to thank my family for always encouraging me and asking about my work, sending news articles on the Chignecto Isthmus, and teaching me about my own family's history with the dyke systems and salt marshes around Amherst. I want to thank my D&D family for always encouraging me despite my missed sessions. Lastly, I want to thank my partner Chad Arsenault for IT support, coding help when I was stuck, encouraging me through the pandemic and yet another academic program, and all the love and support at home.

Table of Contents

Table of Figures

List of Tables

List of Equations

List of Acronyms

Acronym	**Meaning**
ADCP	Acoustic Doppler Current Profiler
ADV	Acoustic Doppler Velocimeter
CGVD	Canadian Geodetic Vertical Datum
DAV	Depth Averaged Velocity
Dc	Distance from channel (variable)
DEM	Digital Elevation Model
DFC	Distance from Channel (raster)
Di	Distance from inlet
DIGS	Disaggregated Inorganic Grain Size
DSM	Digital Surface Model
GNSS	Global Navigation Satellite System
Hydro/Topo	Hydrologic and Topographic variable (models)
MR	Managed Realignment
PMTH	Predicted Maximum Tide Height
RHT	Relative to High Tide
RPAS	Remotely Piloted Aircraft System
RSB	Rising Stage Bottle
RSLR	Relative Sea Level Rise
RTK	Real Time Kinematic
SLR	Sea Level Rise
SSC	Suspended Sediment Concentration
WGS	World Geodetic System
WSE	Water Surface Elevation

CHAPTER 1 INTRODUCTION AND LITERATURE REVIEW

Land and infrastructure around of the Bay of Fundy are being threatened by rising sea levels and other effects of climate change. Low-lying farmland surrounding the Bay of Fundy occupies former tidal wetlands, currently protected from tides and storm surges by dykes. Some of these dykes are at a high risk of erosion or overtopping, and maintenance costs are increasing (van Proosdij et al., 2018). In areas where the farmland behind the eroding dykes is underutilized, the preferred option may be managed realignment (MR). During this process new dykes are created further inland, sections of the old dykes are graded to natural marsh elevations, and tidal inlets and channels are created. This allows tides to inundate the former agricultural surface and deposit sediment (French, 2006), providing an opportunity for salt marsh species to re-establish, creating a restored salt marsh with room to migrate inland (Pontee, 2013; Torio & Chmura, 2016; van Proosdij et al., 2023). These processes may be limited by insufficient sediment deposition with respect to the rising sea levels (Gardiner et al., 2007; Singh et al., 2007; Valiela et al., 2018), causing these marshes to drown (Kirwan & Temmerman, 2009).

The landscape trade-offs between the agricultural dykelands and these new MR sites are being studied by the *Landscape 1 – Bay of Fundy Dykeland Futures*[1], part of the ResNET project funded by the Natural Sciences and Engineering Research Council (NSERC) (Sherren et al., 2021). One of the goals of Landscape 1 is to determine how long until marshes restored through MR are able to provide protective services and if they accrete enough to keep pace with sea level rise (SLR), continuing these services. As a part of the ResNET project, this thesis will explore the potential connections between the inlet hydrodynamics, topography, and sediment deposition

---

[1] *https://www.nsercresnet.ca/landscape-1---bay-of-fundy.html*

patterns on a MR site using visual and statistical analyses. The findings of this study aim to improve predictions of restoration trajectories and accretion modelling in relation to SLR. This chapter will cover literature on natural marshes describing hydrologic, topographic, and other variables affecting the availability, movement, and deposition of sediment. It will also include current MR salt marsh research, sedimentation modelling, and the specific questions this thesis will address.

1.1 Sea Level Rise Resilience with Salt Marshes and Managed Realignment Sites in the Bay of Fundy

Climate change has caused thermal expansion of the ocean and melting of vast amounts of ice from polar ice caps and land ice (Cazenave & Nerem, 2004; Le Bars, 2018; Mitrovica et al., 2001), driving sea levels to rise at an accelerated rate (Oppenheimer et al., 2019). The immediate danger of SLR is not the slow rise of mean water levels over time, but rather the influence of high-water levels on coastal flooding caused by storm surges. It is expected that 0.2-4.6% of global populations could flood annually by the year 2100 (Hinkel et al., 2014).

Areas of Nova Scotia and New Brunswick are currently subsiding, compounding SLR effects (James et al., 2014). During the last ice age this area was situated at the forebulge of the Laurentide ice sheet and was therefore higher than its current elevation. Since the glaciers have retreated, this area has been sinking due to isostatic adjustment. Combined with the eustatic sea level rise, the relative sea level rise (RSLR) for the area is estimated to be 0.8 to 1m by the year 2100, in a worst-case scenario for greenhouse gas emission rates (James et al., 2014), but could reach up to 1.4 to 1.6m by the year 2100 including higher contributions from the West Antarctic Ice Sheet (James et al., 2021). In the Bay of Fundy, with some of the highest tides in the world, tidal ranges are expected to expand with climate change, causing even greater flooding during storm surges (Greenberg et al., 2012). As a result, the Bay of Fundy area is at high risk for extreme flooding before the end of the century.

Coastal defences are needed to prevent damages from expected flooding associated with climate change. Current strategies being implemented include hard engineering solutions such as sea walls, breakwaters, and dykes or levees, all of which require high maintenance costs that are expected to increase with sea levels. New infrastructure will require even higher initial costs in anticipation of SLR (Narayan et al., 2016). In the Bay of Fundy, the cost of maintaining dykes could reach $12-71 billion by 2100 (Hinkel et al., 2014).

The research for this study was performed in the Chignecto Isthmus. As of 2022, SLR adaptation plan options in the area include raising or building new dykes, possibly building steel sheet pile walls, and building water control structures downstream of existing bridges. These options range from $200-300 million in initial costs with $7.31 to 10.98 million in operating costs (Government of New Brunswick et al., 2022). It may, however, be possible in some areas to transition from these current hard engineering practices into more resilient natural infrastructure that can provide additional co-benefits (Narayan et al., 2016).

Nature-based SLR defences could provide sustainable and cost-effective options, due to their ability to self-regulate and respond to environmental changes. Hybrid solutions such as MR combine hard engineering and nature-based solutions, where the benefits of dykes and salt marshes are combined. Salt marshes are known for their ability to protect coastlines from flooding, since their vegetation can attenuate waves and storm surges, preventing higher water levels (Anderson & Smith, 2014; Augustin et al., 2009; Gedan et al., 2011; Shepard et al., 2011).

This vegetation can also provide protection for new dykes on MR sites, reducing maintenance costs, and additional protection for the areas behind the dykes (French, 1999; Virgin et al., 2020).

There are, however, possible drawbacks of using salt marshes and therefore MR to combat SLR. If water levels increase to a critical threshold without accreting enough sediment to keep pace with SLR, vegetation will degrade and drown (Kirwan & Temmerman, 2009). Salt marshes must be able to adapt to these changes. Sediment must accrete and roots expand so the salt marsh surface, or platform, will rise. The marsh will also migrate inland to shallower areas as sea levels rise (Nyman et al., 2006; Singh et al., 2007). The ability of a salt marsh to adapt to SLR is limited by sediment accretion and barriers, such as dykes and sea walls, preventing inland migration (Pontee, 2013; Torio & Chmura, 2016), resulting in "coastal squeeze" (Doody, 2004). It is estimated that from 2 to 95% of salt marshes could drown or degrade from 2080 to 2100, depending on uncertainty of global SLR projections (Gardiner et al., 2007; Singh et al., 2007; Valiela et al., 2018). MR may mitigate coastal squeeze, however current research, especially in North America, is limited in understanding the morphological evolution and sediment dynamics of these sites.

1.2 Sediment Dynamics on Natural Marshes

1.2.1 Sediment Flux on Natural Salt Marshes

Vertical sediment accretion is the result of sediment travelling to an area, depositing, and accumulating over time (Figure 1.1). The amount of sediment travelling through a specific area carried by the tidal flow through tidal creeks, channels, or inlets, is referred to as the sediment flux (Murphy & Voulgaris, 2006; Poirier, 2014; van Proosdij, 2001). The sediment flux is used to calculate the sediment budget of an area, which is defined by the sediment flux into the area on the flood tide minus the sediment flux out of the area on the ebb tide (Poirier, 2014; van Proosdij, 2001). The vertical flux, or the settling or resuspension of the sediment, depends on sediment availability, settling velocities of the grains and flocculated particles, and the energy of the water (Green et al., 2014; Lund-Hansen et al., 1999; Wang et al., 2013). As water slows down around slack tide, more sediment will fall out of suspension, depositing on the bed, which may then resuspend on the ebb tide as the marsh drains (Hill et al., 2013; O'Laughlin, 2012).

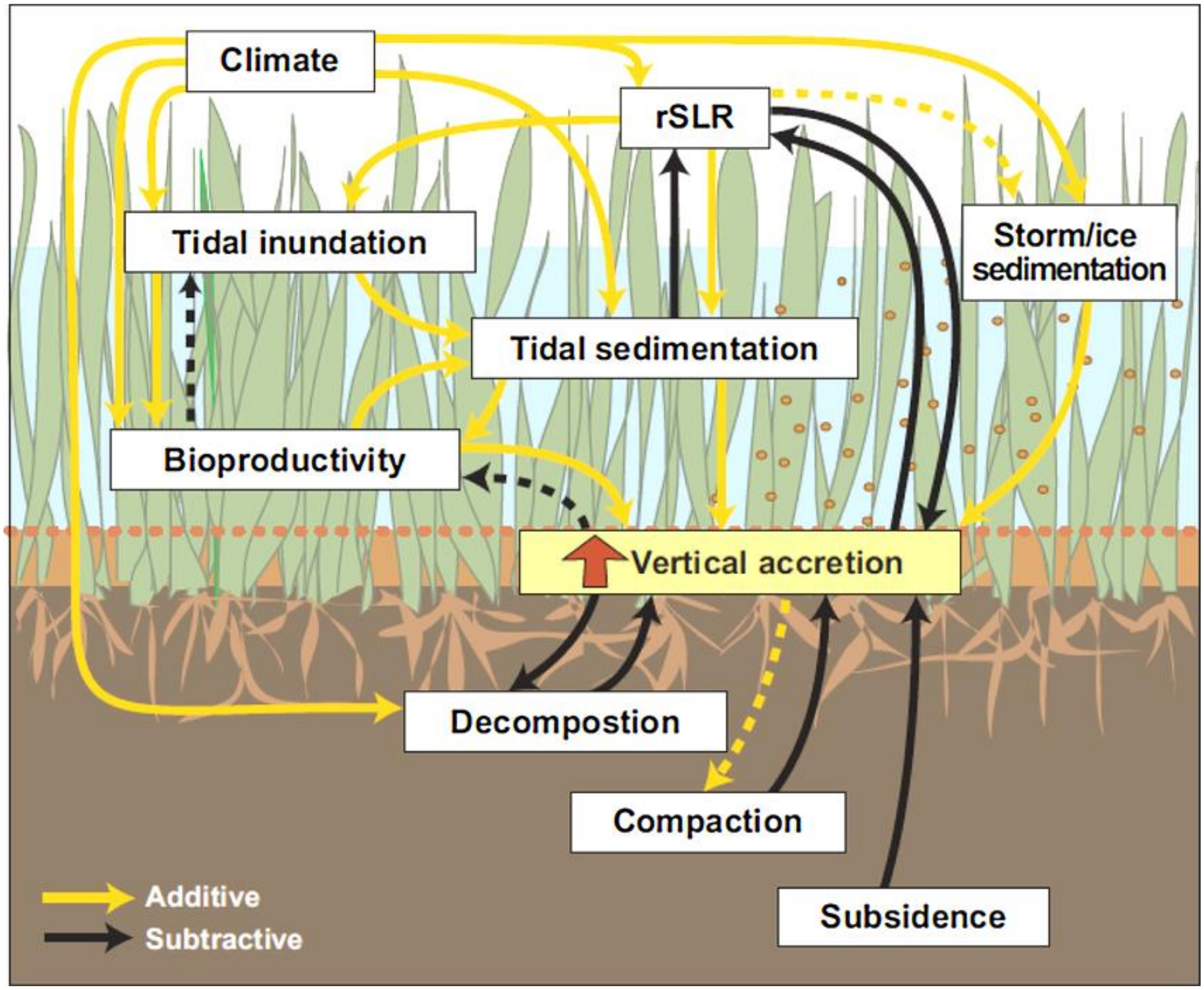

Figure 1.1. Flow chart of vertical accretion with associated variables (FitzGerald et al., 2008).

1.2.2 Effects of Hydrodynamics and Marsh Inlet and Channel Interactions on Sediment Flux

The interactions between the hydrodynamics of the tide and the topography of the marsh surface affect how sediment is dispersed and deposited around the marsh. Depending on the height of the tide, the head of the water being restricted by the inlet and channels creates changes in velocity across the site (Bayliss-Smith et al., 1979). Larger tides and narrower channels will result in higher velocities (Bayliss-Smith et al., 1979; Friess et al., 2014; O'Brien, 1969). These higher velocities create more turbulent energy causing scour (Friess et al., 2014) and resuspension of sediment which results in higher suspended sediment concentrations (SSC) (O'Laughlin & van Proosdij, 2013; Xie et al., 2010) and a higher sediment flux.

During high enough tides, the marsh surface will begin to flood after the channels are filled. As the water reaches marsh surface elevations, there is an initial rapid increase of velocity then a decrease in velocity, or a flood velocity pulse (Bayliss-Smith et al., 1979; Davidson-Arnott et al., 2002). These pulses can transport water and sediment further up onto the surface of the marsh (Bayliss-Smith et al., 1979). Also, pulses on the ebb tide can resuspend newly deposited sediment (Hill et al., 2013). This means larger tides transport more sediment further from the inlet and further from the channels, doing the most work in importing and redistributing sediment (O'Laughlin, 2012; Voulgaris & Meyers, 2004).

Flow restriction from a smaller cross-sectional area can cause a reduction of the tidal prism, or the total volume of water entering and leaving the site (O'Brien, 1969). A smaller tidal prism may mean less sediment is allowed to enter the site; however, the restriction could cause higher velocities and therefore higher SSC, promoting higher sediment flux. Smaller channels also promote flood dominance, resulting in infilling with imported sediment, further reducing the tidal prism (Friedrichs & Perry, 2001).

The grain size of the sediment also has an impact on sediment transport, where the smaller the grain size, the lower the settling velocities, and the more easily the grains will stay in suspension. This relationship is complicated by smaller particles such as silt and clay that can flocculate together from electrochemical forces (Green et al., 2014), increasing their settling velocity, making them more likely to settle (Guo et al., 2017; Kranck, 1980; Kranck & Milligan 1992; O'Laughlin et al., 2014; Winterwerp, 1998). High velocities can also cause higher SSC from the breakup of flocs due to turbulence (Curran et al., 2004; Hill et al., 2013). When velocity and therefore turbulence are low enough, flocculation occurs causing increased settling. Flocculation has a square dependency on particle concentration therefore high SSC can lead to greater vertical flux of sediment (Winterwerp et al., 2006).

1.2.3 Effects of Hydrodynamics and Marsh Surface Interactions on Sediment Flux

Sediment is deposited on the salt marsh platform during tides that are high enough to flood out of the channels. The amount of sediment deposited at a specific point on the marsh depends on elevation and the distance from the source of the water flooding the surface.

Deeper water over the marsh surface means there is a larger volume of water and therefore more sediment available for deposition above that point on the marsh. Also, longer inundation times allow more sediment to settle, resulting in higher deposition rates (Voulgaris & Meyers, 2004). Therefore, elevation can play a significant role in sediment deposition (Leonard, 1997), where sediment deposition decreases with increasing elevation (Chmura et al., 2001; Hill et al., 2013; Reed et al., 1999; Richard, 1978).

The distance the water has travelled from the water source, such as the distance to the tidal creek, or the distance to the marsh edge, reflects how far the water has travelled through the channels and over the marsh, losing velocity along the way. As the velocity decreases, sediment settles onto the marsh surface (Reed et al., 1999), affecting the amount of deposition further from the source (Butzeck et al., 2015; Davidson-Arnott et al., 2002; Temmerman et al., 2003; van Proosdij, 2001). Areas further from the water source also receive finer sediment, since the coarser material has fallen out of suspension (Poirier et al., 2017).

1.2.4 Seasonal, Atmospheric, and Biological Effects on Sediment Flux

Atmospheric conditions can also influence SSC and sediment flux by resuspending sediment on unvegetated surfaces. Dale et al. (2018) showed that SSC levels can be elevated for three days after a rainfall of 1 to 2 $mm \cdot hr^{-1}$. This effect increases when the precipitation occurs at low tide when mud flats are exposed (Murphy & Voulgaris, 2006). The winter months can bring more storms which have higher winds, contributing to more wave action, and more precipitation, which can increase suspended sediment levels (Law et al., 2019; Poirier, 2014). Wind can also resuspend sediment at shallower depths (van Proosdij, 2001), and resuspend flocs, resulting in lower amounts of finer deposited material (Law et al., 2019).

Vegetation can help promote deposition and prevent resuspension by dampening wave action and slowing tidal currents (Davidson-Arnott et al., 2002; Leonard & Luther, 1995; van Proosdij et al., 2006; van Proosdij et al., 2013). Microorganisms can also reduce erodibility on mud surfaces by forming biofilms (Carriére-Garwood, 2013; Garwood et al., 2015). This can increase resuspension in the winter when biofilms are lost. These seasonal factors affecting sediment merit research across a range of seasons.

1.3 Sediment Dynamics on Managed Realignment Sites

The initial agricultural surface of a MR site differs greatly from a natural marsh when a site is first breached. The marsh surface may experience rapid sedimentation after initial tidal water inundations (Virgin et al., 2020; Wollenberg et al., 2018). This means that in this period there will only be elevation gain from sediment accretion, or loss from compaction and decomposition of organic matter from the covered agricultural lands. In the first couple of years of restoration, a restoring marsh will not be fully covered in vegetation, possibly causing differences in hydrodynamics and sedimentation compared to a natural marsh including more resuspension and different deposition patterns. These differences could continue for an unknown amount of time which may also affect the time for these restored salt marshes to deliver protective services.

The old dykes surrounding the restored marshes may be advantageous, sheltering the restoring marsh from wave action, preventing resuspension, and promoting accretion (Vuik et al., 2019), though the effects would end after dyke erosion occurs. Erosion from the scour of the newly constructed inlets and channels (Friess et al., 2014) may also add to the sediment budget of the site, encouraging deposition on the marsh surface. These rates may change as the inlet, channels, and marsh surface move toward a morphological equilibrium. Models of sediment deposition and accretion and the morphological evolution of the sites in this environment are needed to quantify this in conjunction with MR site changes.

MR is relatively new in the Bay of Fundy and within the last decade studies have been performed to try and predict the restoration trajectories of the reclaimed marshes (Bowron et al., 2011; Byers & Chmura, 2007; MacDonald et al., 2010; Norris et al., 2022). A few of these studies focused on erosion and accretion (van Proosdij et al., 2010; Virgin et al., 2020). The high concentrations of fine-grained sediment in the macrotidal Bay of Fundy (Amos & Mosher, 1985; Poirier, 2014), may help marshes to keep pace with SLR, improving restoration trajectories.

1.4 Deposition and Accretion Models for Natural Marshes

Previous sediment and accretion models on natural salt marshes have used topographic variables such as elevation (D’Alpaos et al., 2011), distance to creek and marsh edge (Butzeck et al., 2015; Temmerman et al., 2003), and estimated SSC (Schile et al., 2014). These studies used hydrologic variables mostly limited to measured water depth and SLR estimations. Best et al. (2018) incorporated tidal hydrodynamics, wave action, and geomorphological changes, though these changes were limited to marsh elevation. Some of these past studies have large portions of the models dedicated to the effects of vegetation, however, MR sites take years to become fully vegetated (Wollenberg et al., 2018). To be applied to MR sites, this thesis will need to incorporate the unique, fast-paced changes caused by rapid erosion of inlet(s) and channels at these sites (Friess et al., 2014; Lewis, 2022; van Proosdij et al., 2010).

1.5 Purpose and Research Questions

This thesis will explore the connections between hydrology, topography, and sediment deposition on a restoring marsh surface through one year of restoration and create a simple statistical model to improve predictions of restoration trajectories and accretion modelling. Sediment accretion, or compounded deposition, is a result of sediment flux through these sites, which may be unique on MR sites in the Bay of Fundy. Sediment flux is affected by the hydrodynamics of the tide, the topography of the site, and other environmental factors such as weather and biological effects. These variables can potentially be used to create the statistical model to predict deposition at a specific point on the marsh. Three fundamental questions will be addressed in this thesis:

- How do the sediment flux and hydrologic factors at the inlet of a restoring salt marsh vary temporally?
- How does sediment deposition vary spatially and temporally on a restoring salt marsh?
- Can hydrologic factors measured at the inlet and topographic factors be used to model deposition across a restoring salt marsh?

CHAPTER 2 STUDY SITE AND METHODS

2.1 Managed Realignment Study Site

2.1.1 Converse Managed Realignment Site

This study was conducted within the Converse restoration site, a recently constructed managed realignment site located near Amherst, Nova Scotia, on the Chignecto Isthmus (Figure 2.1). This site is part of the *Making Room for Wetlands*[2] project, funded by Fisheries and Oceans Canada's Coastal Restoration Fund (2017-2022). The Converse restoration site sits near the mouth of the Missaguash river which empties into the Cumberland Basin, connected to the Chignecto Bay in the Upper Bay of Fundy.

As part of the realignment process, a new dyke was constructed with material from the old dykes as well as excavated material from the agricultural area beside the new dyke. This excavation created a borrow pit, which was studied separately to determine how fast the area would infill with new sediment from the incoming tidal water (Lewis, 2022). Areas of the dyke were graded to the natural surrounding marsh surface level to allow flooding over these areas. Finally in December 2018, the aboiteau was dug out, creating a tidal inlet, allowing water from the Missaguash tidal river to inundate the area. The pre-breach image in Figure 2.2a shows the aboiteau location and eroding dykes surrounding the site. Figure 2.2b shows the dug inlet and graded areas as bare ground during Year 1 of restoration. The predicted restored area of the site was ~ 15.4 ha (Bowron et al., 2020).

---

[2] *https://www.transcoastaladaptations.com/making-room-for-wetlands*

Figure 2.1. Location of Converse Restoration Site in the Chignecto Isthmus.

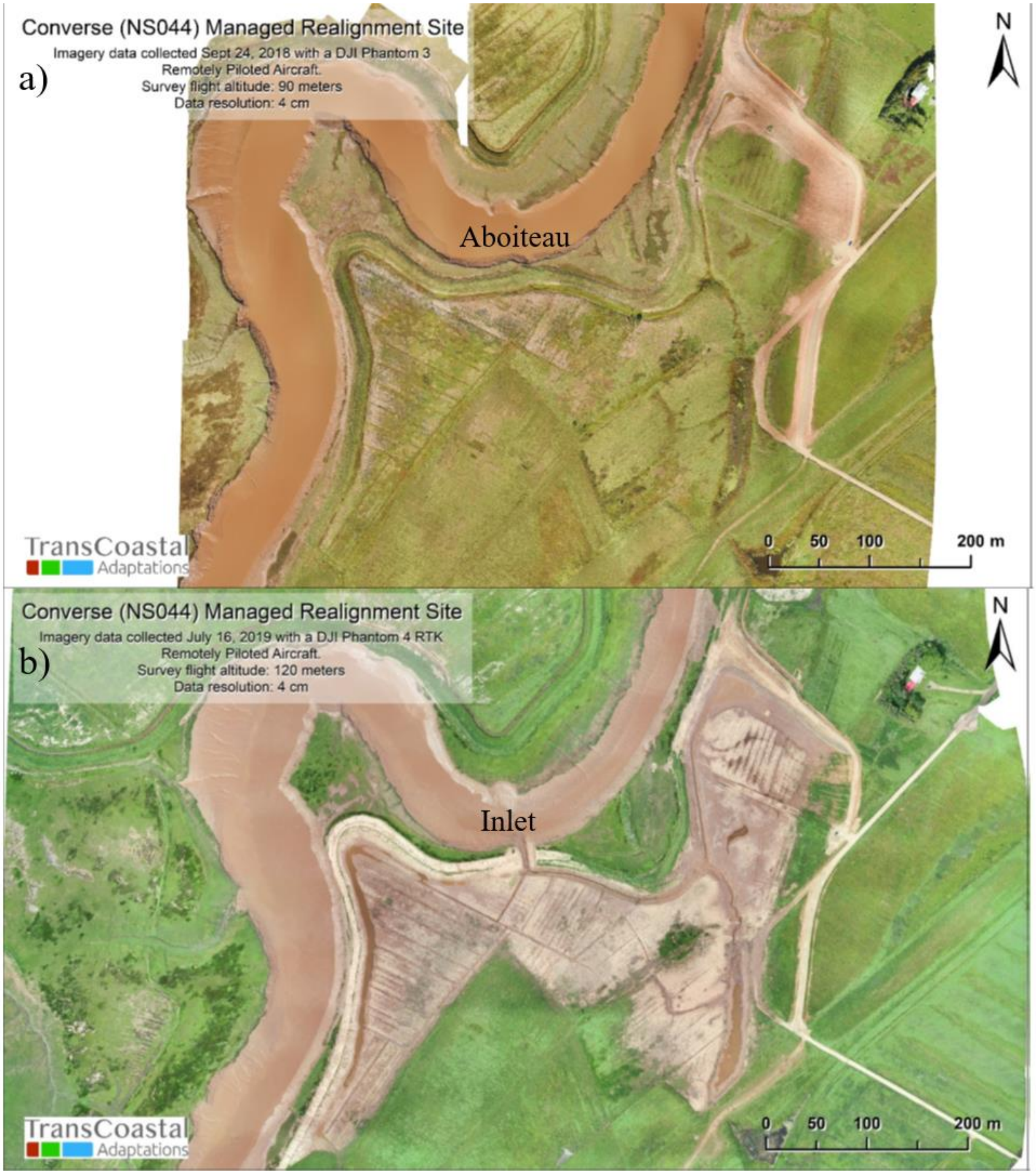

Figure 2.2. Pre-construction aerial image of the Converse managed realignment site in image a) (Bowron et al., 2020); post-construction aerial image of the Converse managed realignment site, Year 1, in image b) (Bowron et al., 2020).

2.1.2 Bay of Fundy Tides and Sediment Conditions

The Bay of Fundy tides are some of the largest in the world, reaching over 15m in the Upper Bay (Desplanque & Mossman, 2004) that can erode and resuspend bed sediment. Along with freshwater sediment input and cliff erosion, they have created sand flats that progress into shallow estuaries with silt and clay in Chignecto Bay (Amos et al., 1991). Estuaries and inlets in the Upper Bay of Fundy have very high concentrations of fine-grained sediment in suspension (Amos & Mosher, 1985; Poirier, 2014).

Tides can be separated into their harmonic constituents, caused by different astronomical gravitational forces, which create different sinusoidal variations in tide height over different cycle periods (Desplanque & Mossman, 2004). In the Bay of Fundy, the major harmonic constituents consist of 2 high tides per day (diurnal), 2 spring tides per month, and 1 perigee tide per month (Table 2-1). The spring and perigee tides line up every 206 days creating the largest tides of the year, the perigean spring tides (Desplanque & Mossman, 2004). During the study period of this thesis, in 2020 and 2021, the peaks of this cycle were in the fall and spring.

Table 2-1. Tidal harmonic cycle lengths in the Bay of Fundy (Desplanque & Mossman, 2004; van Proosdij & Page, 2012).

Cycle	Period (days)
Diurnal	0.517
Spring-neap	14.77
Perigee-apogee	27.55
Perigean-spring	206

2.1.3 Previously Collected Data

This research draws upon variables and data collected by others at the Converse site and is described as part of the site characterization. Sediment-related parameters were measured in December 2018 and August 2019, reported in Ellis et al. (2018) and Bowron et al. (2020), as part of a 5-year post restoration monitoring program associated with the *Making Room for Wetlands* project. The restoration area was mapped with orthophotos, and digital surface models (DSM) derived from Remotely Piloted Aircraft System (RPAS) surveys (Akyol, 2020; Lewis, 2022). RPAS flights were taken approximately monthly throughout the spring/summer/fall field seasons to monitor topographic changes on the marsh (Lewis, 2022). The drainage system including the inlet, constructed channels, agricultural ditching, and newly forming channels, seen in Figure 2.2b, were monitored and studied in Lewis (2022).

Elevation and accretion were monitored across the site using four Rod Surface Elevation Tables (RSETs) (Cahoon et al., 2002) and 30 marker horizons, installed across the site in summer 2018, and measured annually. Since elevation changes also depend on growing and decomposing vegetation, RSET measurements combined with cores from surrounding marker horizons show the amount of sediment accretion versus elevation changes due to decomposing organics and root system expansion (Lynch et al., 2015).

2.2 Overview of Methods

For this thesis, data were collected for five or six tides for each of three deployments that took place in August and November 2020 and July 2021 of Year 2 and Year 3 of restoration, respectively. Observations were taken at tide, season, and annual temporal scales. Variables measured in this study relate to the availability and movement of sediment, shown in the literature, and are summarized in the flow chart in Figure 2.3. Hydrologic variables including water depth, velocity, and SSC were measured over each tide at the inlet to capture the temporal variations of inlet conditions. Cross-sectional measurements of the inlet were also taken for each deployment as part of a co-occurring study in Lewis (2022). These hydrologic and cross-sectional measurements were also used to calculate the discharge and sediment flux at the inlet. Additional velocity and SSC measurements were taken in the channels to help understand the dispersion of sediment throughout the site.

Variables relating to deposition were measured for each tide at different surveyed stations to observe the spatial and temporal variations of deposition across the restoring marsh surface. These included deposition per tide, the grain size distribution of deposited sediment per tide, and at some locations, the initial suspended sediment concentration per tide. Once clear linkages were established between hydrologic and topographic variables and deposition, a selection process was performed to find the best model to predict deposition at a point on the marsh.

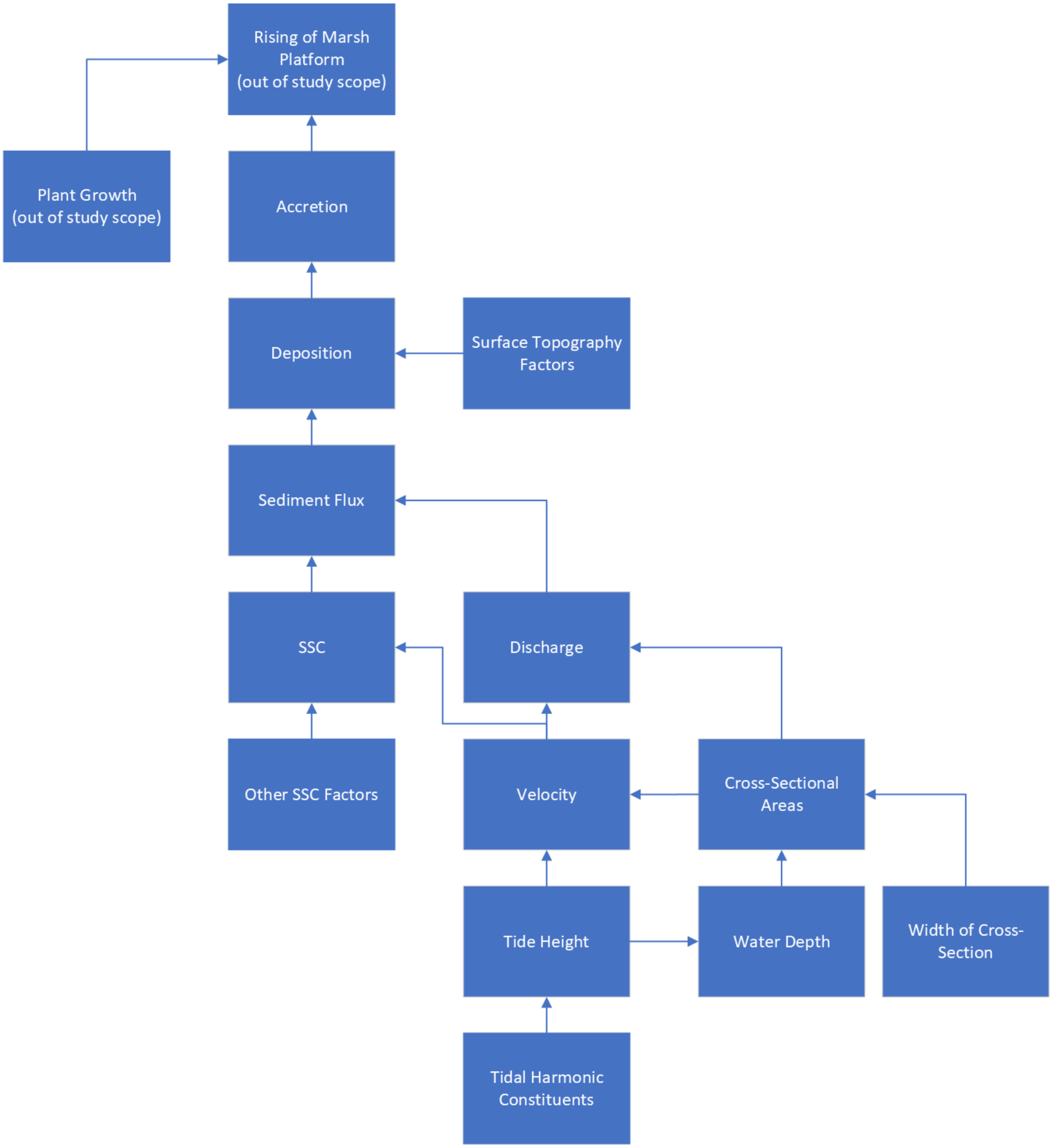

Figure 2.3. Flow chart of variables affecting deposition and sediment accretion measured in this thesis.

2.3 Spatial Layout and Setup of Instruments and Stations

To observe the spatial variations of deposition and sediment flux at the Converse site, instruments were placed in the inlet, channels, and on the surface of the marsh (Table 2-2, Figure

2.4). At the inlet, a Nortek Aquadropp Acoustic Doppler Current Profiler (ADCP) and ISCO automated water sampler were deployed. The ADCP was located on the floor of the inlet with the x axis pointing downstream, aligned with the flow direction (Figure 2.5). The ground and ADCP sensor height were measured with an RTK GNSS for each deployment. The ADCP was programmed to take measurements every 10 seconds for 30 cells above the ADCP, set to 0.2m in distance, with a 0.2m blanking distance from the ADCP to the first cell, totalling 6.2m above the ADCP sensor. This height purposely exceeded the top of the inlet and the highest potential tides. An ISCO automated water sampler pumped 500 ml water samples at 15-minute intervals, 9.5m to the pumping unit situated on the remnant dyke (Figure 2.6). The inlet nozzle was located 10 cm from the bed as close to the ADCP as possible (Figure 2.5).

Table 2-2. All Stations with instruments used and variables measured.

Station	Instruments/Equipment	Variables Measured
Inlet	• ISCO Automated Water Sampler • Acoustic Doppler Current Profiler (ADCP)	• SSC (grain size subsamples) • Velocity • Depth
V1, V3	• Acoustic Doppler Velocimeter (ADV) • Turbidity Sensor	• SSC • Velocity • Depth
V2	• ADV	• Velocity • Depth
R1	• Turbidity Sensor	• SSC
Marker Horizon (MH) Sediment Stations n=8	• Sediment Trap • Tile Sediment Trap	• Deposition • Grain Size
Rising Stage Bottle (RSB) Sediment Stations n=6	• Sediment Trap • Tile Sediment Trap • Rising Stage Bottle (RSB)	• Deposition • Grain Size • Initial flood SSC (grain size subsamples)

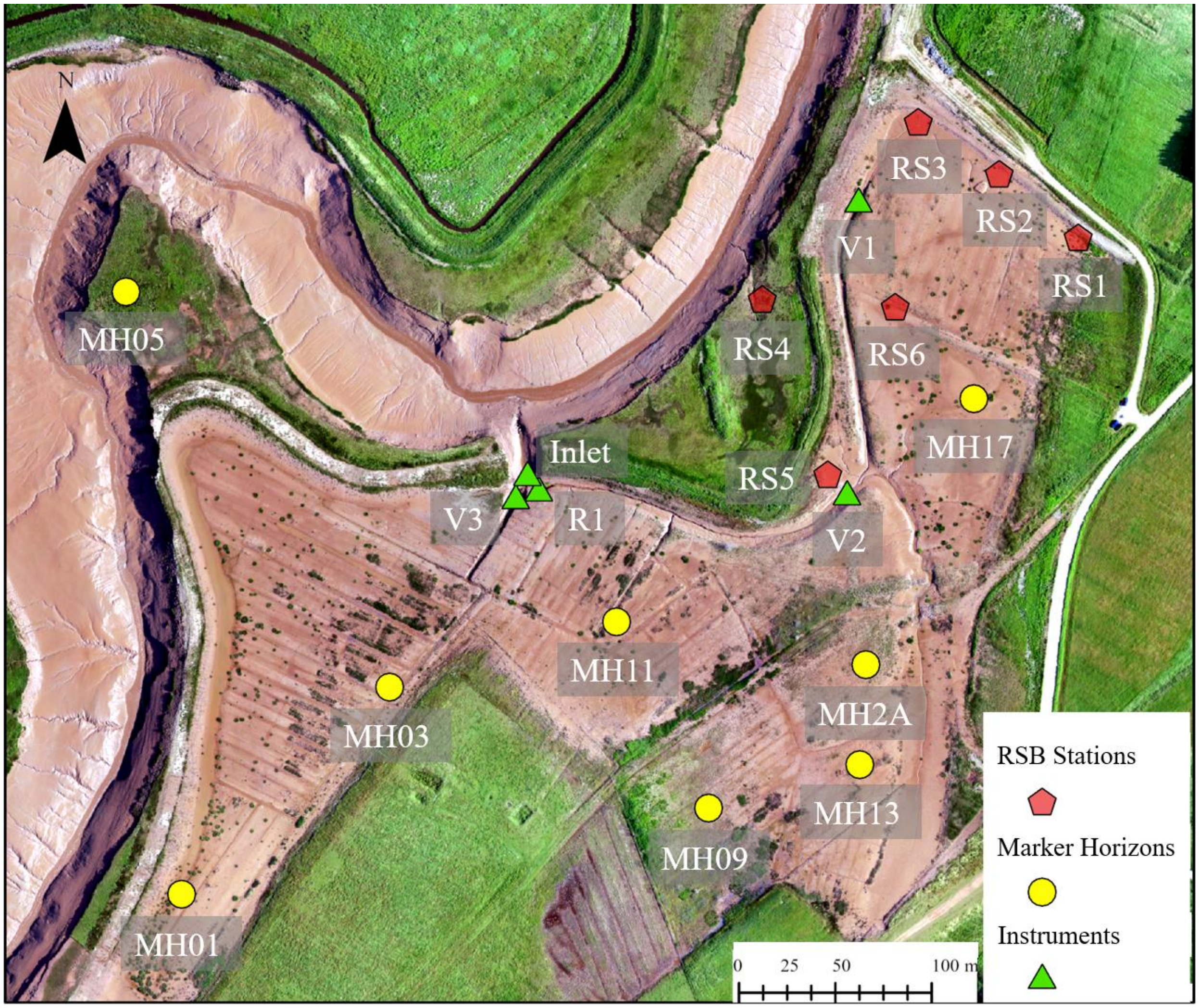

Figure 2.4. Converse deployment map with station legend. Orthomosaic created with imaging from a DJI Phantom 4 RTK Remotely Piloted Aircraft System (RPAS), piloted by Samantha Lewis on July 25, 2021, processed in Lewis (2022).

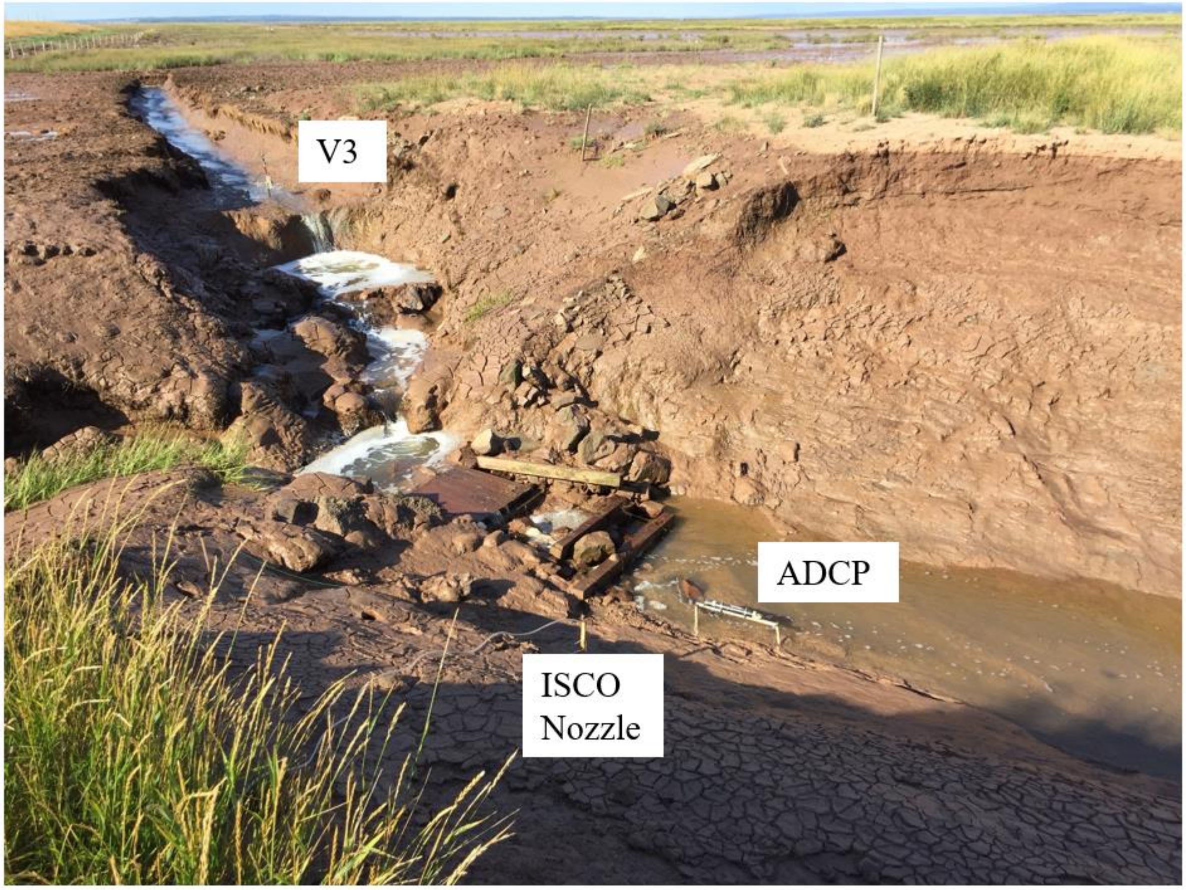

Figure 2.5. Acoustic doppler current profiler (ADCP) with ISCO automated water sampler nozzle to the left of the ADCP, taken August 23rd, 2020 (TransCoastal Adaptations, 2020).

Figure 2.6. ISCO automated water sampler body setup on dyke beside inlet, taken November 15th, 2020.

In the channels, Nortek Acoustic Doppler Velocimeters (ADVs) and Ruskin RBR turbidity sensors were used at the locations indicated in Table 2-2 and Figures 2.4 and 2.5. The ADVs were placed in the thalweg of their respective locations, with sensors located 25cm above the bed, taking a sample volume 10cm from the bed. The x axis was pointed downstream (Figure 2.7). The ADVs were programmed to sample at a rate of 16 Hz, with 4800 samples per burst (5 minutes) every 600 seconds (10 minutes). The ground and sensor height of each ADV was measured with an RTK GNSS for each deployment.

Figure 2.7. Acoustic doppler velocimeter (ADV) with RBR turbidity sensor setup in channel thalweg (station V3), taken August 21st, 2020 (TransCoastal Adaptations, 2020).

A Ruskin RBR XR-420 (Figure 2.8) was located at the R1 station and a Ruskin RBRsolo^3 was situated at station ADV3, and an additional RBRsolo^3 at V1 during the July deployment. These instruments were set on continuous mode, measuring every 10 seconds. All sensors were placed in the thalweg of the channel, with sensors placed 10cm above the bed.

Figure 2.8. Ruskin XR-420 RBR turbidity sensor in thalweg of channel (R1 station), taken August 21st, 2020 (TransCoastal Adaptations, 2020).

Deposition and grain size samples were collected for each tide at the sediment stations, surveyed with an RTK GNSS. Each sediment station had a sediment trap consisting of a numbered Whatman 90mm CAT5 filter paper set on top of a supporting sponge between 2 aluminum sheets with a 90mm circular cut out (Poirier, 2014; van Proosdij, 2001) (Figure 2.9). These were held together by long-shanked bolts and nuts, where the bolts were sunk into the ground with around 0.5 to 2cm clearance depending on how flat the area was. The traps were visually levelled upon deployment. After each tide the filter papers were transferred to petri dishes and swapped for clean traps and filter papers. These stations also had sediment trap tiles measuring 6”x6” that were laid rough side up to prevent sediment from sliding off the tiles and to better simulate the marsh surface. The sediment deposited from each tide was scraped off the tile into a sample vial and swapped for clean tiles. The traps and trap tiles were retrieved for cleaning to prevent contamination of the next tide’s deposited material.

The rising stage bottle (RSB) sediment stations had an RSB as well. The RSB consisted of a 500ml Nalgene bottle and a rubber bottle stopper with 2 tubes coming out of the top of the bottle, one to let water in, and the other to let air out, to only collect the initial tidal water (Graczyk et al., 2000) (Figure 2.9). The bottles were placed directly on the ground, attached to the stake by a hose clamp, with the intake tubes 20 cm above the bed.

Marker horizon station locations were chosen to be at the same locations as the pre-existing marker horizons, and MH2A was also co-located with an RSET station. The RSB station locations were the same as the previous borrow pit study on the Northeast section of the site. Due to limited resources, initial SSC was limited to these stations. Two stations, MH05 and RS4 (Figure 2.4) were located in foreshore marsh vegetation for comparison between natural foreshore and the restoration site.

Figure 2.9. Sediment station (pre-collection) with sediment trap, tile, and rising stage bottle (RSB), taken July 23rd, 2021 (TransCoastal Adaptations, 2020).

2.4 Data Processing and Variables for Analysis

2.4.1 Inlet Hydrologic Variables

2.4.1.1 Inlet Hydrologic Data Processing

Water level data from the ADCP was converted to the CGVD2013 datum, adjusted for the ADCP sensor height of each deployment. This gave the water surface elevation (WSE) relative to the DEM. The WSE was used to relate other recorded and calculated hydrologic variables to the site's topography. The current speeds resolved from the ADCP beams for the x, y, and z directions were used to calculate the velocity magnitude for each cell above the ADCP, using Equation 2-1. The Storm post-processing program (Nortek, 2018) was also used to visualize the average velocity for each submerged cell for each timestep over the tides.

Equation 2-1. Velocity magnitude using vector components.

$$U = \sqrt{{u_x}^2 + {u_y}^2 + {u_z}^2}$$

The cross-sectional area of each cell was calculated using the combined data points from the inlet shape from Lewis (2022) for each corresponding deployment, and the elevation points of the top and bottom of each ADCP cell. Horizontal trapezoid areas were calculated using this combined set of data points and summed for the total cross-sectional area of each ADCP cell. Discharge and sediment flux values were calculated from these pre-calculated cell areas using equations from section 2.4.1.2 and the SSC data from the ISCO for each timestep for each completely submerged cell. If the WSE was less than the elevation of the top of a given ADCP cell at a given timestep, the cell was considered not submerged during that timestep and all variables were set to zero for the cell. The average velocity of the submerged cells for each timestep was used for the depth averaged velocity (DAV). Discharge values were summed for all cells at each timestep to get the depth summed instantaneous discharge, and the sediment flux values were summed to get the depth summed instantaneous sediment flux values. These were calculated in and plotted against WSE using MATLAB.

The ISCO water samples were processed using suction with a measured volume of sample being filtered onto pre-weighed 0.8µm Millipore filter papers. Filters were then dried and reweighed to 0.001g precision. The net weight of the sediment filtered from the water samples and volume of samples were used to calculate the SSC of each ISCO sample. The SSC values were used to produce box and whisker plots of the SSC distribution over each available tide for all deployments. A set of ISCO samples from one tide from each deployment had subsamples taken for grain size analysis described in section 2.4.3.

2.4.1.2 Calculations for Discharge, Sediment Flux, and Sediment Budget

Sediment flux depends on the concentration of sediment in the water and discharge: the current velocity combined with the cross-sectional area of the given area. In tidal creeks, this is the submerged cross-sectional area of the creek. The instantaneous sediment flux through an inlet or channel can be written as Equation 2-2 (Poirier, 2014).

Equation 2-2. Instantaneous sediment flux using discharge.

$$Q_{st(xsa)} = Q_{wt} \times SSC_t$$

Where $Q_{st(xsa)}$ is the instantaneous sediment flux, Q_{wt} is the instantaneous discharge, and SSC_t is the instantaneous sediment flux. Q_{wt} can be broken down further in Equation 2-3 (Poirier, 2014). The variable $\overline{U}_t$ represents the velocity of the water and $A(h_t)$ represents the cross-sectional area of the channel. The SSC was assumed to be fully mixed throughout the water column for simplification and due to the results of this study showing high velocities and all particle grain sizes being below 64 µm (Nordin & Dempster, 1963).

Equation 2-3. Instantaneous sediment flux using velocity and cross-sectional area.

$$Q_{st(xsa)} = SSC_t \times \overline{U}_t \times A(h_t)$$

The cross-sectional area was broken down into the ADCP cells for the ADCP cell velocities as described in section 2.4.1.1 for these calculations. The cross-sectional area of the channel can also be represented in Equation 2-4 (Poirier, 2014).

Equation 2-4. Instantaneous sediment flux using velocity, width, and height.

$$Q_{st(xsa)} = SSC_t \times \overline{U}_t \times W \times h_t$$

The variable W represents the width of the water column and h_t is the depth of the water. The total sediment flux over a period of time is the sum of the average sediment flux between instances, represented in Equation 2-5 (van Proosdij, 2001). Where y is the instantaneous sediment flux, and x is the timestep.

Equation 2-5. Total time-averaged sediment flux.

$$Q_s = \sum_{i=1}^{n-1} \frac{(y_i - y_{i+1})}{2} (x_{i+1} - x_i)$$

The sediment budget was assumed to be the difference between the flood and ebb sediment flux values (Poirier, 2014; van Proosdij, 2001).

2.4.2 Channel Hydrologic Data Processing

A MATLAB script from Purcell (2020) was adapted to process the burst measurements of the ADVs, and then plot the velocity magnitude against WSE with the ADCP script described in section 2.4.1.1. The WSE was calculated from the pressure sensor readings and adjusted for the sensor height in mCGVD2013 of each ADV for each deployment. The data from the RBR turbidity sensors were converted to SSC units using an equation generated from the dry-sediment calibration process described in the Campbell scientific turbidity sensor user guide (Campbell Scientific INC., 2014).

2.4.3 Marsh Surface Deposited and Suspended Sediment Sample Processing

The filter papers from each sediment trap sample were dried and weighed to 0.001g precision to determine the deposition weight per unit of area, using the pre-weights of each numbered filter paper and the effective area of the sediment trap (the cut-out area) where the sediment settled (Poirier, 2014; van Proosdij, 2001). Deposition was plotted in MATLAB against topographic variables and mapped using ESRI ArcGIS Pro.

The tile trap scrape samples were subsampled for disaggregated inorganic grain size (DIGS) analysis, where the DIGS can show the aggregation and settling conditions of the sediment sample (Law et al., 2019; Milligan & Kranck, 1991; Milligan & Loring, 1997). The subsamples were dried and digested in 30% hydrogen peroxide to remove organic material. The samples were then disaggregated using an ultrasonic probe. The samples were processed through the Beckman-Coulter Multisizer III electroresistance particle counter to measure the grain size distribution. The samples were diluted depending on the aperture of the tube used (30 µm and 200 µm) to prevent coincidence error, where two particles enter the sensing zone at the same time. Samples were re-sonicated before processing with each aperture.

A MATLAB script called MergeProcessor with integrated folders and functions (Carriére-Garwood, 2013; Newgard, 2012) was used to merge the DIGS data from each aperture to get the entire spectrum of grain size data for the sample. Additionally, a MATLAB script (Curran et al., 2004) was used to calculate the floc fraction with the merged data files, where the floc fraction is a value from 0 to 1 used to describe the amount of material in the sample deposited in floc form, with 1 being fully flocculated. GRADISTAT, developed in Blott & Pye (2001), was used to determine the D50 value as a single representative value for the grain size of each sample. Scripts were adapted from the merge processor to plot and layer DIGS curves for further analysis. The D50 and floc fraction values were also mapped using ESRI ArcGIS Pro.

The RSB samples were processed using the same procedures as the ISCO samples in section 2.4.1.1 and plotted against inlet SSC and deposition in MATLAB. A set of RSB samples from one tide from each deployment (and all for July due to a lack of samples) were subsampled for the DIGS process described above.

2.4.4 Topographic Variables

The topographic variables elevation, distance from creek (Dc), and distance from inlet (Di) were obtained for each station. The elevation used was from the survey data of each station. The station survey coordinates, and a channel system map developed in Lewis (2022) were used to measure and calculate the Euclidian distance from the station to the nearest creek, and the distance of the station to the inlet, following the flow path of water, in ESRI ArcGIS pro. In the case of MH05 and RS4, Di was the distance to the marsh edge, following the path of water.

2.4.5 Predicted Tides and Weather Data

The predicted maximum tide heights (PMTH) were retrieved for deployment planning to ensure the tides would flood the marsh surface and to examine temporal placement of the deployments with respect to the tidal harmonic cycles. The PMTH was also assessed for its usefulness in predictive deposition models since this data is posted for every tide in a 12-month period. The data was retrieved from the Canadian Hydrographic Service[3]. The station used was Pecks Point (00190), located 19.3km from the Converse site. PMTH was plotted in MATLAB for 2020 and 2021 and compared to the deployment dates and used in statistical modelling.

Weather data was retrieved from Environment Canada historical weather and climate data[4]. The Nappan Auto station in Nappan, Nova Scotia was used, located 9.3km from the Converse site. Precipitation was plotted in MATLAB for 2020 and 2021 and compared to the deployment dates. A wind rose using the maximum wind gust data was also plotted with this data using a MATLAB script from Pereira (2023).

---

[3] *https://tides.gc.ca/en/tides-currents-and-water-levels*

[4] *https://climate.weather.gc.ca/historical_data/search_historic_data_e.html*

2.5 Statistics and Modelling

2.5.1 Statistical Models Overview

Three statistical models were proposed, each using the deposition weight per unit area and a different set of variables to determine the best formula for predicting deposition at a point on the marsh surface. This was to create a map of sedimentation, based off the methods of Temmerman et al. (2003), where the model formula was applied to rasters of topographic variables to create the map. The first model was from Temmerman et al. (2003) used as a known, working reference model. The development of the other two models was theorized based on the visual data analysis of this study and literature review. One model included the hydrologic and topographic variables measured in this study and the other used PMTH and the topographic variables. The best model formula can be applied to the digital elevation model (DEM) and distance from channel model (DFC) rasters that were developed in Lewis (2022) for the Converse site, making a similar map as Temmerman et al. (2003).

2.5.2 Working Reference Model

The formula from Temmerman et al. (2003) is shown in Equation 2-6, that predicts the sedimentation rate at a point on a marsh. SR is the sedimentation rate per spring-neap cycle ($g \cdot m^{-2}$), H is the tidal intensity (the elevation of the marsh point adjusted with the cumulative depth), Dc is the distance to the creek, and De is the distance from the marsh edge, following the creek system. The coefficients are k, l, m, and n, calculated in Temmerman et al. (2003), using SAS/STAT software and field data. The field data included water level and sedimentation measurements of 15-day spring-neap cycles at points across a marsh surface. The equation was applied to each raster cell of the study’s marsh, each cell having an H, Dc, and De value.

Equation 2-6. Temmerman et al., (2003) sedimentation rate model formula.

$$SR = ke^{lH}e^{mD_c}e^{nD_e}$$

The sedimentation rates used in this thesis would be single-tide marsh surface deposition, having the same g·m^{-2} units as the 15-day cycle sedimentation rates. The tidal intensity in Temmerman et al. (2013) was calculated with the elevation of a point adjusted with the cumulative depth over the tide. This would need to be calculated for every point on the marsh, or every cell in the DEM, for each tide. On large scales over many varying tides this would require additional software modules to make these calculations. For simplicity, only elevation was used for the purpose of this study, however, a post-analysis model was tested with the H variable to determine the impact of only including elevation. The De value used was the distance to the inlet (Di) following the flow path of water, as there is no marsh edge on the MR site. With these substitutions, Equation 2-7 was used for the Temmerman et al. (2003) adjusted model as a working reference model to compare to the new models.

Equation 2-7. Adjusted Temmerman et al., (2003) sedimentation rate model formula.

$$Deposition = ke^{lE}e^{mD_c}e^{nD_i}$$

2.5.3 Hydrologic Topographic Model

2.5.3.1 Model Theory

Deposition depends on the influx of sediment and the distribution of that sediment through the channels and across the marsh surface. This means that if the marsh, channels, and flow across the marsh were uniform, the sediment would be distributed uniformly. This would result in the net sediment (influx of sediment minus outflux, Equation 2-8) divided by the surface area of the marsh in Equation 2-9.

Equation 2-8. Net sediment equation.

$$Sediment\ in - Sediment\ out = Net\ Sediment$$

Equation 2-9. Net sediment equally distributed on marsh surface.

$$Deposition\ over\ uniform\ marsh\ for\ uniform\ tide = \frac{Net\ Sediment}{Surface\ Area\ of\ Marsh}$$

In reality, the marsh has channels with varying cross-sections and three-dimensional variations in the marsh surface. The sediment laden water, with varying times of entry, will encounter different topographic features, experiencing different losses of energy (Bayliss-Smith et al., 1979), where sediment will settle along the way. This results in variations in sediment available for deposition at different points on the marsh, changing throughout the tide. On the ebb tide, as the marsh drains, sediment can be resuspended, redistributing, and/or carrying it out of the marsh (Hill et al., 2013; Traynum & Styles, 2007). A simplified version of this can be described in Equation 2-10 below, where the hydrology, topography, and their interactions are both needed to determine sediment distribution across the site, where the deposition is represented as the final deposition of the tide at a point on the marsh surface.

Equation 2-10. Hypothesized point deposition formula.

$$\begin{aligned} &Deposition_{point} \\ &= Hydrologic\ factors\ over\ time\ (sediment\ carrying\ and\ driving\ factors) \\ &* Topographic\ factors\ of\ marsh\ channels\ and\ surface\ (dividing\ factors) \end{aligned}$$

2.5.3.2 Model Variables

The hydrologic and topographic variable (Hydro/Topo) models used all hydrologic inlet and topographic variables mentioned in section 2.4, including the cross-sectional area, water depth and inlet width used in the inlet variable calculations (Figure 2.10). For this study there were seven hydrologic and three topographic variables that were tested.

Deposition was measured on a tidal basis, where hydrologic variables were measured throughout the tide, and topographic variables were constant. To choose a single value for each tide for each hydrologic variable, it was hypothesized that the most representative value would be the sum of the variable over the tide, validated by the results of this study. The cumulative depth was used for the same logic in Temmerman et al. (2003), to reflect the magnitude and frequency of the variables. The width of the inlet was calculated using similar logic. Since the width of the inlet at the water surface does not uniformly increase as the water rises, the cumulative sum of the submerged widths was used, calculated with the lines dividing the trapezoids used for calculating the cross-sectional area.

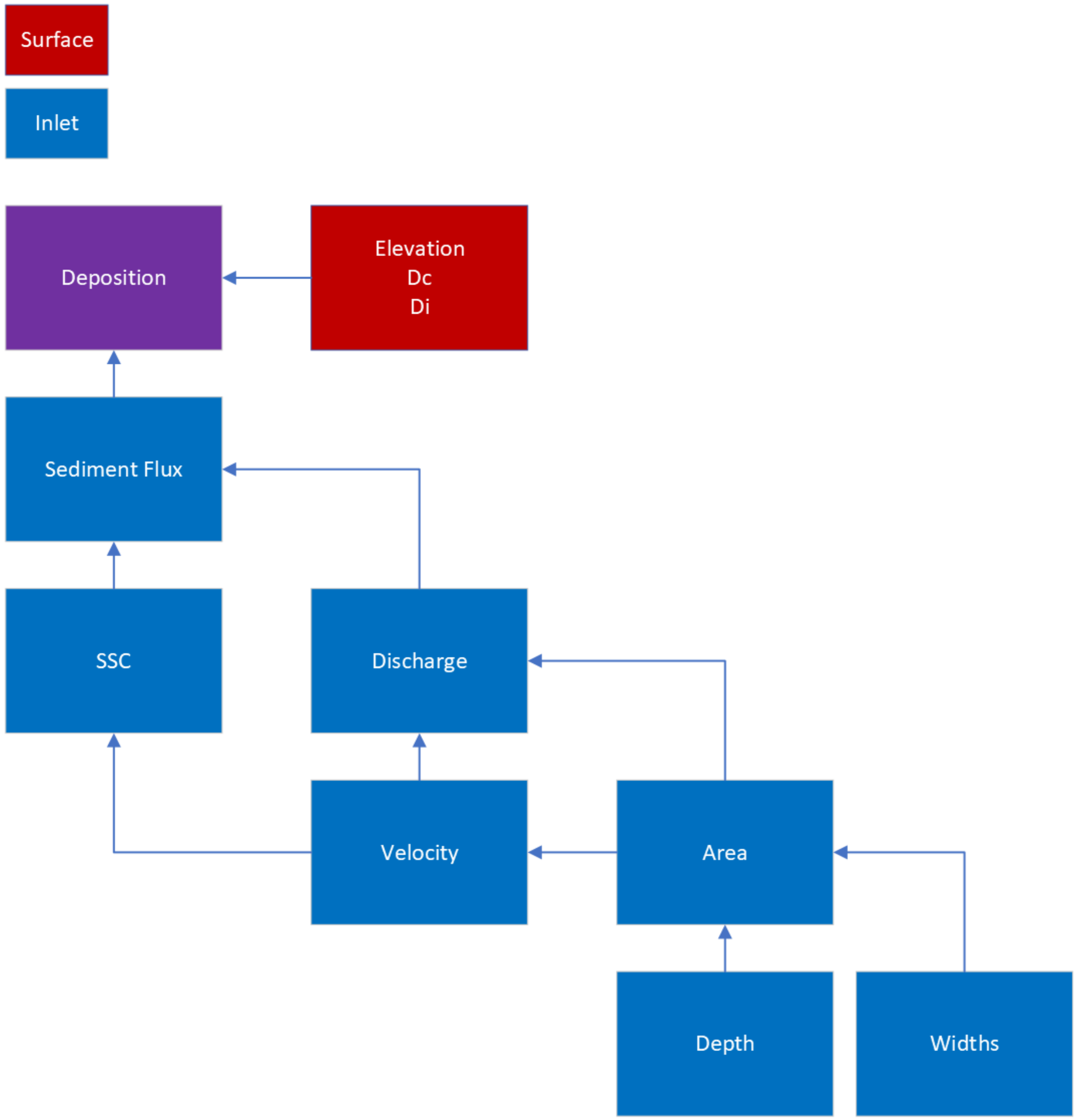

Figure 2.10. Model variables contributing to deposition, divided into marsh surface and MR site inlet variables.

2.5.4 Predicted Maximum Tide Height Model

In this model, instead of using the hydrologic variables measured, the variable used in conjunction with the topographic variables was the predicted maximum tide height from the

Canadian Hydrographic Service tidal predictions. The topographic variables and model theory remained the same as the Hydro/Topo models. The PMTH models were assessed alongside the Hydro/Topo models.

2.5.5 Model Selection Process

2.5.5.1 Model Setup and Selection Process Overview

The three proposed formulas were evaluated in models where deposition was the response variable, which had groupings, or random effects variables, in this dataset that included the tide and station location of samples (Table 2-3). Additionally, this data had fixed effects variables (predictors) such as the hydrologic and topographic variables. Because there were random and fixed variables in this dataset, mixed models were used in R with the lme4 library (Bates et al., 2015). Individual models and results were organized in Excel between steps to manage the large number of models. The variables were also scaled, and deposition data was normalized. A mixed linear model using only the month of the deployment, representing the time of year, was tested against a null model, to determine if the time of year was significant.

Akaike Information Criterion (AIC) values were used to determine the best fitting model for the least number of unknowns (Bolker et al., 2009; Portet, 2020; Vrieze, 2012), where AIC values are a calculated measure of fit that penalizes models for having more parameters (Bolker et al. 2009). AIC is a value with no maximum or minimum limit and no value the models are aiming for, as it is only used to compare models to each other. These are the best comparative model values to use when determining models for predictions (Bolker et al., 2009).

Table 2-3. Proposed models with random and fixed variables.

Model	Random variables	Fixed variables	Formula
Temmerman et al. (2013)	Location	Elevation, Dc, Di	$Deposition = ke^{lE}e^{mD_c}e^{nD_i}$
Hydro/Topo	Tide, Location	Depth, Widths, Area, Velocity, Discharge, SSC, Sediment Flux, Elevation, Dc, Di	$Deposition = (Hydrologic\ variables) * (Topographic\ variables)$
PMTH	Tide, Location	PMTH, Elevation, Dc, Di	$Deposition = PMTH * (Topographic\ variables)$

The Hydro/Topo and PMTH models had an additional series of selection stages to find the optimal combination of variables for the final model testing. There were many ways to combine the 10 variables in a model: using different levels of combinations (e.g., using velocity and area versus discharge), adding versus multiplying, regression type (linear, polynomial, etc.), and other considerations. However, combining some of these options (e.g., multiplying 10 polynomial variables) would create too many terms with regard to the number of independent variables, which would create models that are overfitted (Portet, 2020; Vrieze, 2012). For this reason, the number of terms that could be used to create a working model was limited. A structured analysis (Figure 2.11) was designed to assess hydrologic and topographic variable interactions among themselves, and then between these groups to create a model balancing accuracy and the number of terms.

2.5.5.2 Selection Process Steps

The first step in the analysis was to test the best regression with deposition for each individual predictor variable, based on the R^2 values. The hydrologic variables were then assessed in a three-part analysis to test each of the resulting variables (sediment flux, discharge, and area) against their constituents, shown in Figure 2.12 where each level corresponds to a different coloured box. For example, discharge was tested against velocity and area, but also against velocity, depth, and widths. Alternative combinations were also tested, such as only velocity and widths. These combinations were tested with the cumulative flood, cumulative ebb, and the net and average of these flood and ebb values with linear, polynomial, added, and multiplied versions. Each set of flood, ebb, net, or average variables was only tested with itself, e.g., average variables were only tested with other average variables, to simplify the process. The models with the lowest AIC from each level of the hydrologic variables was taken as the best model, along with the alternative model with AIC values within this range.

Topographic variables were then tested for their interactions with each other, with the same combination factors as the hydrologic variables (Figure 2.12, corresponding to orange). Individual topographic variables were then tested against each individual hydrologic variable (including PMTH), using the same combinational factors (Figure 2.12, corresponding to red). This was used in the next step to determine how the formulas should be combined. For example, if the only two interactions were Di and Dc (Equation 2-11a) and Dc and Area (Equation 2-11b), the resulting formula encompasses both the interactions (Equation 2-11c), where Dep is deposition.

Equation 2-11. Example of combining topographic and hydrologic formulas, where a) is the topographic formula, b) is the hydrologic formula, and c) is the combination if Dc interacts with all hydrologic variables and Di.

a) $$Dep \sim Dc * Di + Elevation$$

b) $$Dep \sim Area$$

c) $$Dep \sim Area * Dc + Di * Dc + Elevation$$

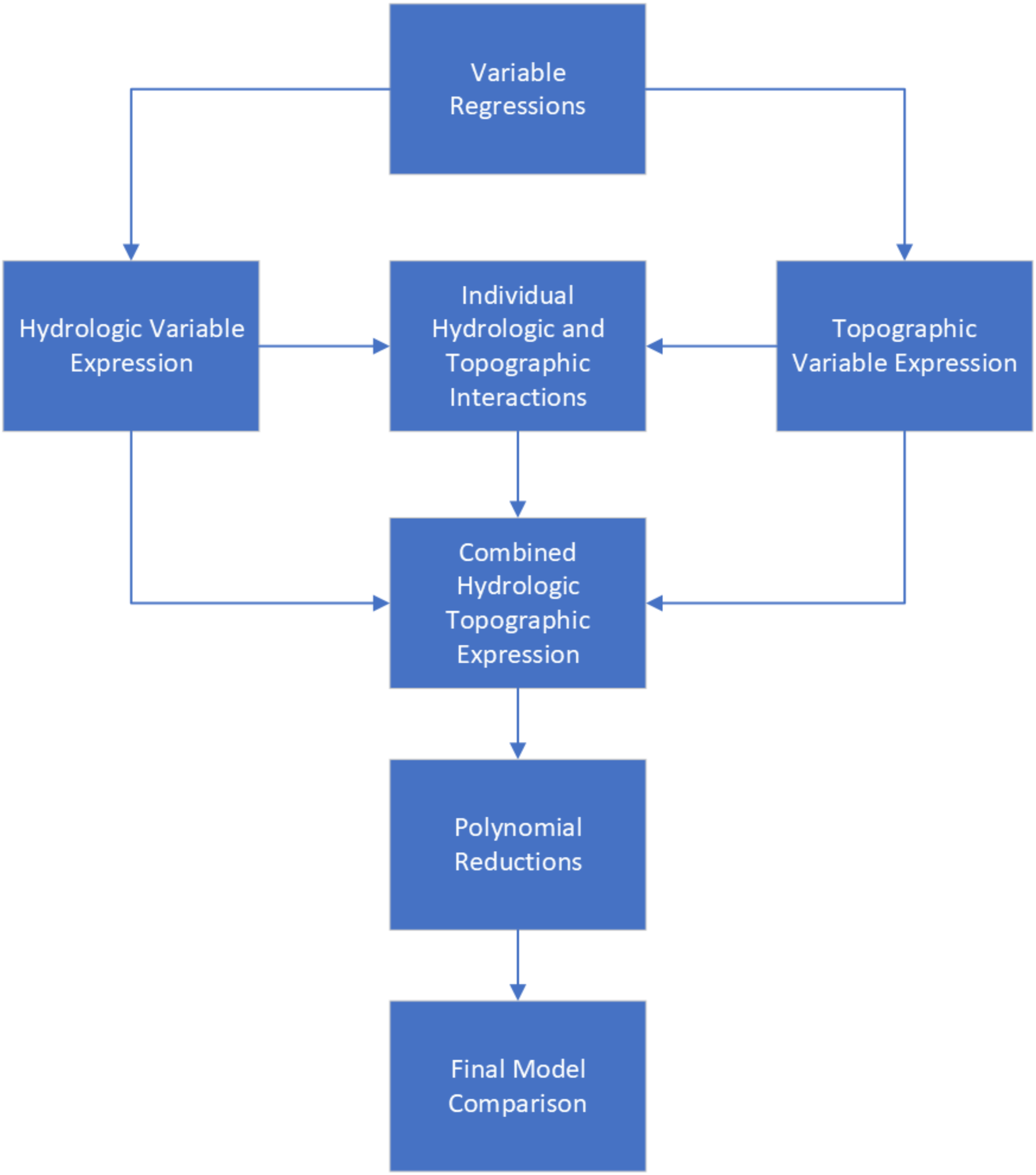

Figure 2.11. *Statistical model development process structure.*

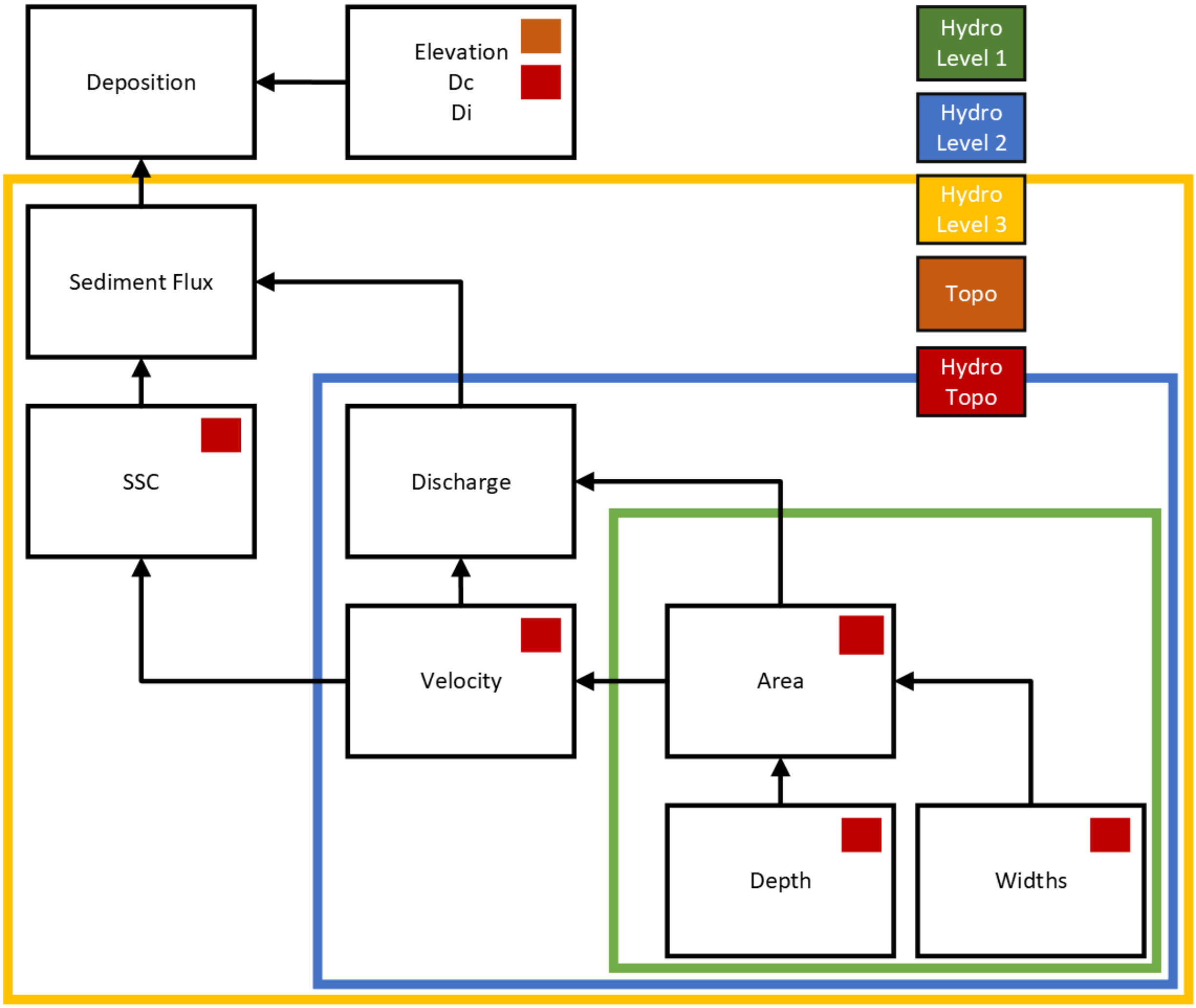

Figure 2.12. Model variables contributing to deposition with associated model development steps indicated. Hydrologic variables were tested in 3 levels with respect to sediment flux and its contributors, then topographic variables were tested, then hydrologic and topographic variables against each other.

Since some formulas included polynomials of variables, some polynomial terms (e.g., Dc, Dc^2, and Dc^3) needed to be eliminated to reduce the overall number of terms when hydrologic and topographic formulas were combined. This is why the step combining the formulas was paired with a polynomial reduction. Each pair of polynomial terms were tested together as well as each individual term, to find the best combination for a working model.

The best combined Hydro/Topo and PMTH models were then selected using an ANOVA test, where the models are listed according to the number of terms, and models significantly better than the next model (based on AIC) on the list are given a significance value based on a Chi-squared test. A process of elimination was performed using these values to find the significantly best models, where the models remaining were equivalent models, not significantly better than the other. The modified Temmerman et al. (2003) model was introduced in this step. The conditional and marginal R^2 values were then found for the models and the coefficients of each term for each model were determined and analyzed.

CHAPTER 3 RESULTS

Data were successfully collected for a total of 16 spring tides: six in August 2020, and five each in November 2020 and July 2021, though not all tides had full sets of data. Restrictions associated with the COVID-19 pandemic resulted in the cancellation of the spring 2021 deployment. At the inlet, the ADCP did not capture the last two tides of August and the last tide of July, due to the battery dying (Table 3-1). Technical issues were encountered for the ISCO for two of the July tides. This allowed sediment flux at the inlet to be calculated for only 11 tides. In the channels, ADVs and RBRs were able to capture most tides (Table 3-2). The extra RBR at V1 was only deployed in July due to previous turbidity sensors having technical difficulties.

One tide of each deployment had deposition data that was contaminated or not collected due to weather or time constraints with rising tides, where the proportions of successfully collected samples is shown in Table 3-3. Tide heights allowed most of the 14 stations to have data collected for most tides, however two stations with the highest elevations had few samples. These two stations only had one scrape sample, collected during the highest tide: Tide 4 in November. A total of nine tides that had both deposition and sediment flux data available were used for the statistical models.

Table 3-1. Inlet and deposition data per tide available for sediment flux and statistics.

	August 2020						**November 2020**					**July 2021**				
	T1	**T2**	**T3**	**T4**	**T5**	**T6**	**T1**	**T2**	**T3**	**T4**	**T5**	**T1**	**T2**	**T3**	**T4**	**T5**
ADCP	x	x	x	x			x	x	x	x	x	x	x	x	x	
ISCO	x	x	x	x	x	x	x	x	x	x	x		x	x		x
Sediment Stations		x	x	x	x	x	x	x	x	x			x	x	x	x
Sediment Flux	x	x	x	x			x	x	x	x	x		x	x		
Statistics		x	x	x			x	x	x	x			x	x		

Table 3-2. Channel instruments data available per tide.

	August 2020						November 2020					July 2021				
	T1	**T2**	**T3**	**T4**	**T5**	**T6**	**T1**	**T2**	**T3**	**T4**	**T5**	**T1**	**T2**	**T3**	**T4**	**T5**
V1	x	x	x	x	x	x	x	x	x	x	x		x	x	x	x
V2	x	x	x	x	x	x	x	x		x	x	x	x	x	x	x
V3	x	x	x	x	x	x	x	x	x	x	x	x	x	x	x	x
RBR V3	x	x	x	x	x	x	x	x	x	x	x	x	x	x	x	x
R1		x	x	x	x	x	x	x	x	x	x	x	x	x	x	x
RBR V1													x	x	x	x

Table 3-3. Sediment station samples acquired versus planned, per deployment.

Deployment	Deposition Samples	Grain Size Samples	Incoming SSC Samples
August 2020	67/70 (5 tides)	49/70 (5 tides)	28/30 (5 tides)
November 2020	53/70 (4 tides)	42/70 (4 tides)	29/30 (4 tides)
July 2021	48/70 (4 tides)	34/70 (4 tides)	19/30 (4 tides)

3.1 Temporal Variations of Inlet Sediment Flux and Hydrodynamics and Interactions with Site Topography

Temporal variations were observed for the duration of the tide, individual tides, position in harmonic cycles, and restoration year of deployments. The water surface elevation (WSE), velocity, discharge, and sediment flux over the tide all showed expected interactions between the marsh topography and tide hydrology. Velocity and cross-sectional area changes both had visually noticeable effects on the discharge, as well as sediment flux along with changes in suspended sediment concentrations (SSC). The SSC and therefore sediment flux were also affected by rainfall during the July deployment.

3.1.1 Water Surface Elevation at Inlet

The change in water surface elevation (WSE) over time did not follow a smooth sinusoidal tidal curve, showing interactions between the tide and the topographic features of the site (Figure 3.1). At elevations around 5.8m CGVD2013 water floods outside the main channels and starts to flood secondary channels (Figure 3.2), referred to as “bankfull” level. At 6.2m, the entire marsh surface is flooded, referred to as “full site” level. WSE within this range does not change as fast with time (Figure 3.1), resulting in distortions in the curve, more easily seen in the velocity data. Tides with a maximum WSE of around full site level to 6.6m, in Figure 3.1, appear to have similar total tide inundation times, possibly indicating interactions before reaching the site as the tide moves up the Bay of Fundy and Missaguash River. For example, the lowest tide in November (6.2m) appears to have the same total inundation time as the 6.6m November tide. This means the maximum WSE and inundation time would be poorly representative of the tide for statistical modelling, so cumulative hydrologic variables were used in the statistics to capture the entire tide in one variable.

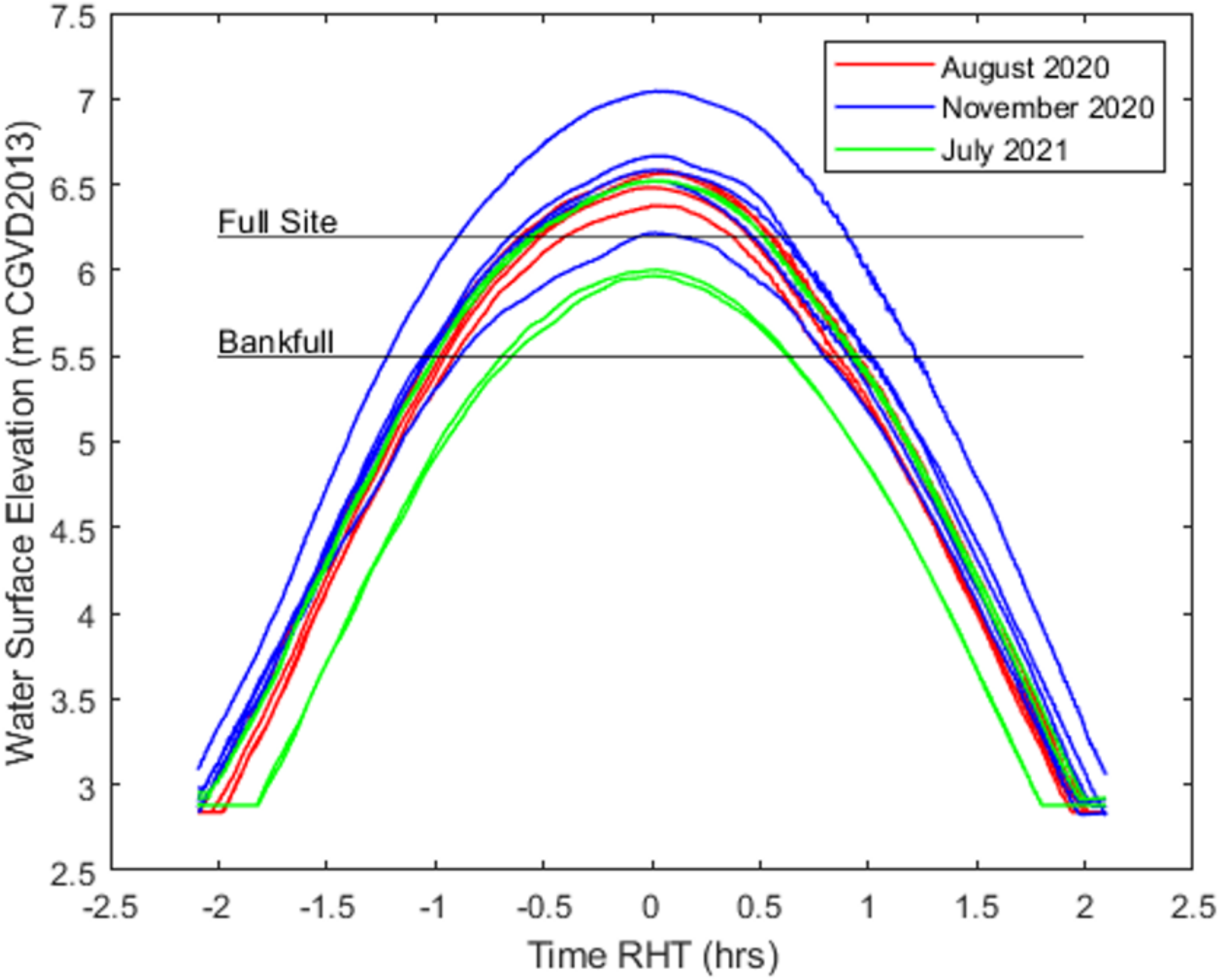

Figure 3.1. Water surface elevation (WSE) relative to high tide (RHT) at inlet for each available tide, overlayed from all deployments with bankfull and full site elevation levels indicated.

Figure 3.2. Site flooded to bankfull level (5.8 m CGVD2013). Orthomosaic and DEM for flood map created with imaging from a DJI Phantom 4 RTK Remotely Piloted Aircraft System (RPAS), piloted by Samantha Lewis on a) June 1, 2020, and b) July 25, 2021, processed in Lewis (2022).

3.1.2 Tidal Harmonic Cycles and Predicted Tides

The PMTH showed the deployments in relation to the tidal harmonic cycles, reflecting the heights of the tides seen in the deployments. The November deployment was almost at the height of the 206 day, perigean-spring cycle, shown in Figure 3.3, where November had the highest tides recorded, also seen in Figure 3.1. August was closer to the middle of this cycle and July closer to the trough, but still in their spring tides of their respective months. July had some of the lowest tides recorded; the only tides not to flood the entire site. Based off of the PMTH of the tides recorded, around 15% of tides during the study period flooded the entire marsh surface.

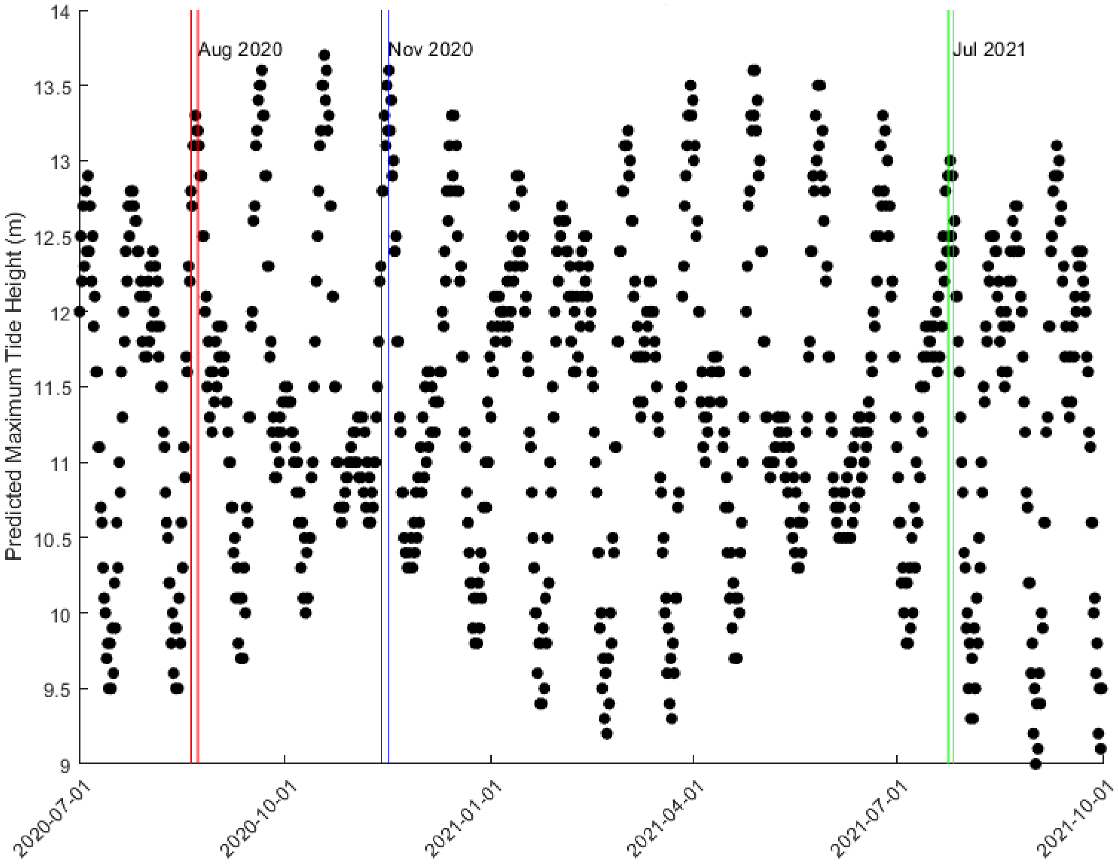

Figure 3.3. Predicted maximum tide height (PMTH) (chart datum) over study period, using data from the Canadian Hydrographic Service.

3.1.3 Current Velocities at Inlet

Velocities at the inlet were sensitive to the marsh elevation, showing interactions with the topography of the marsh. Velocity rapidly increased up to around 0.5 $m \cdot s^{-1}$ after the tide reached bankfull levels. The velocity is seen increasing at different rates, with changing WSE in Figure 3.4, where velocity is represented as depth averaged velocity (DAV). When the WSE reached full site levels the velocity suddenly dropped before increasing again back to the same velocities. There was a rapid shift from flood to ebb velocity with some depth averaged velocities on the ebb tide reaching 1 m·s^{-1}. These patterns, however, were not seen in the two lowest tides in July which did not reach full site levels and had little change in velocity over the entire tide. During the highest tide in November 2020, velocity decreased as water levels reached around 6.7m to 7m. At this elevation, observed in the field, the water was able to flood over the sections of the dyke that were graded to natural marsh platform elevations in the dyke realignment process.

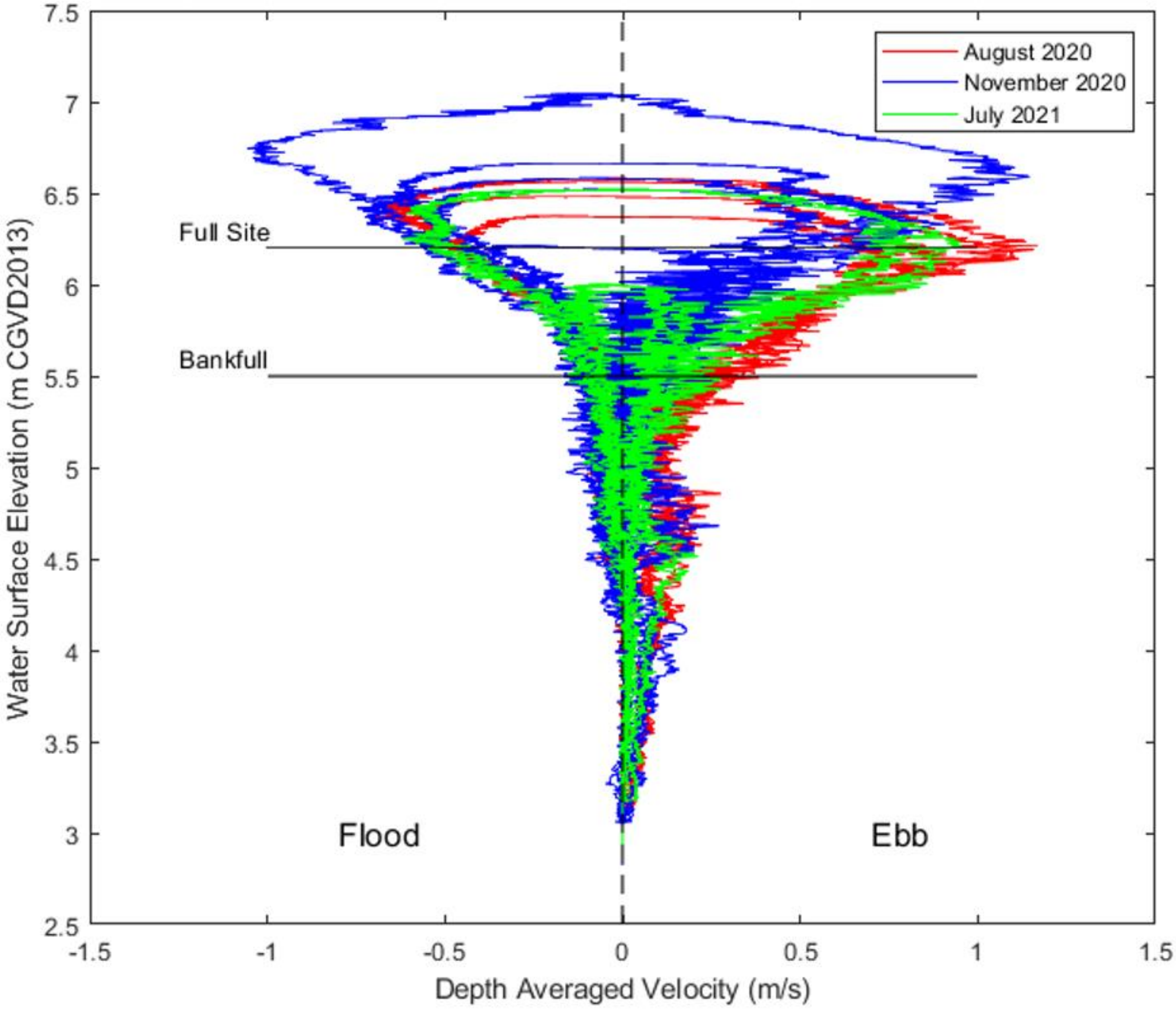

Figure 3.4. Depth averaged velocity (DAV) versus WSE over each available tide, overlayed from all deployments with bankfull and full site elevation levels indicated.

Within deployments, the higher the maximum WSE of the tide, the faster the maximum flood and ebb velocities were. In August, the inlet current velocities on the ebb tide differed greatly compared to November 2020 and July 2021, reaching a DAV of 1 $m \cdot s^{-1}$, matching the highest November tide, a half a metre higher (Table 3-4). August had the highest individual cell velocities of 2 $m \cdot s^{-1}$ at the surface, almost reaching the thalweg. November Tide 4 matched these velocities, reaching 2 $m \cdot s^{-1}$ at the thalweg (Figure 3.5), possibly creating scour. The flood and ebb velocities grew weaker after the August deployment, with the exception of the 7m November tide.

Table 3-4. Average and maximum depth averaged velocity (DAV) values for flood and ebb of each deployment.

Deployment	**Flood**		**Ebb**	
	Avg DAV($m \cdot s^{-1}$)	Max DAV($m \cdot s^{-1}$)	Avg DAV($m \cdot s^{-1}$)	Max DAV($m \cdot s^{-1}$)
Aug. 2020	0.248	0.696	0.257	1.170
Nov. 2020	0.229	1.053	0.181	1.150
Jul. 2021	0.157	0.620	0.139	0.952

3.1.4 Cross-sectional Area of Inlet

There were changes in the cross-sectional area of the inlet between each deployment, as it eroded and evolved, growing toward an equilibrium form as observed in the field and reported in Lewis (2022). The inlet was smallest in August 2020, then slightly widened in the two and a half months leading to the November 2020 deployment (Figure 3.6). There was more noticeable widening and change in shape in the eight and a half months leading up to the July 2021 deployment.

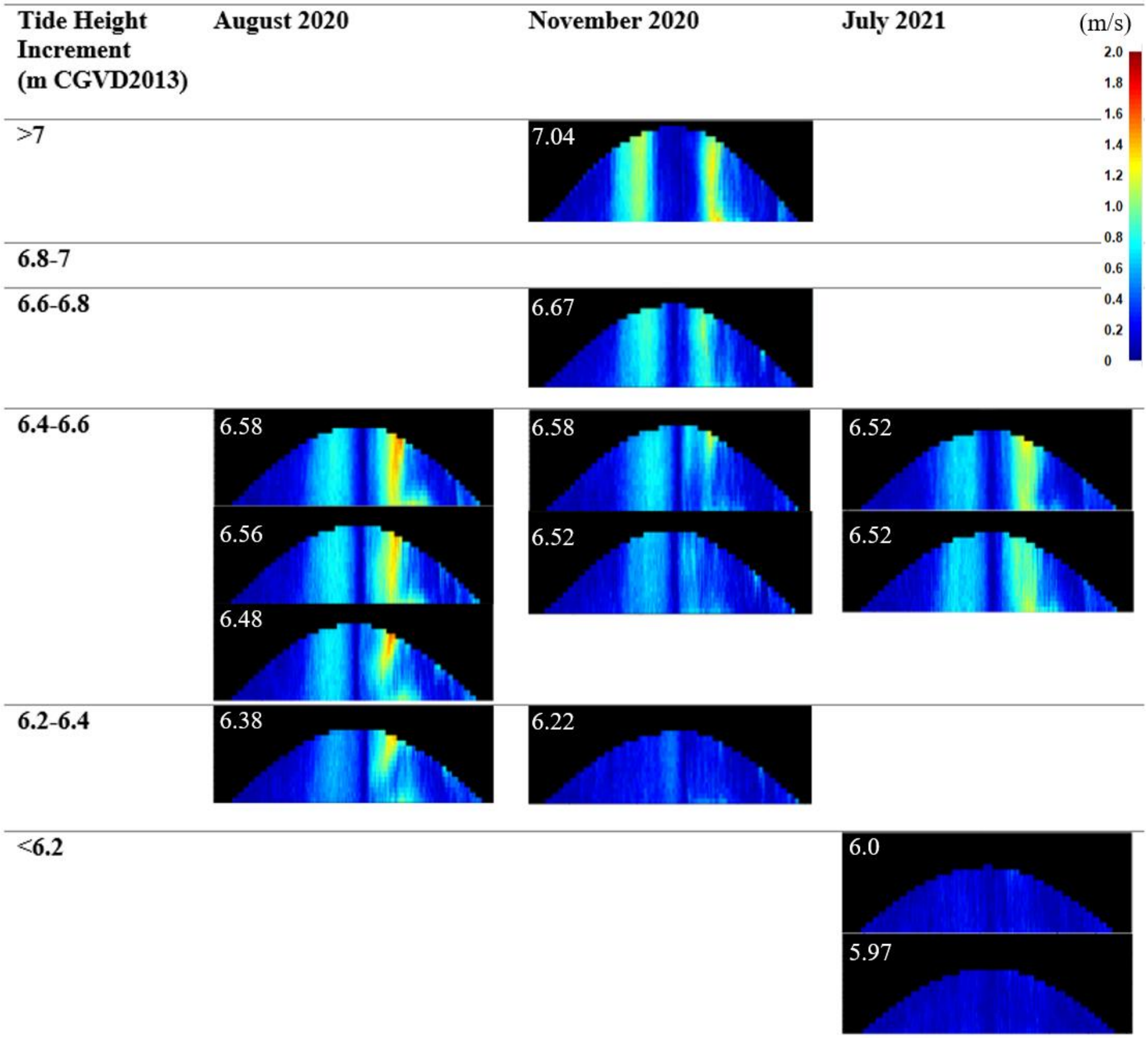

Figure 3.5. Velocity plots from the Storm64 program showing velocity of the rising and falling water. Plots are divided into maximum tide height increments with maximum tide height in the upper left of each plot.

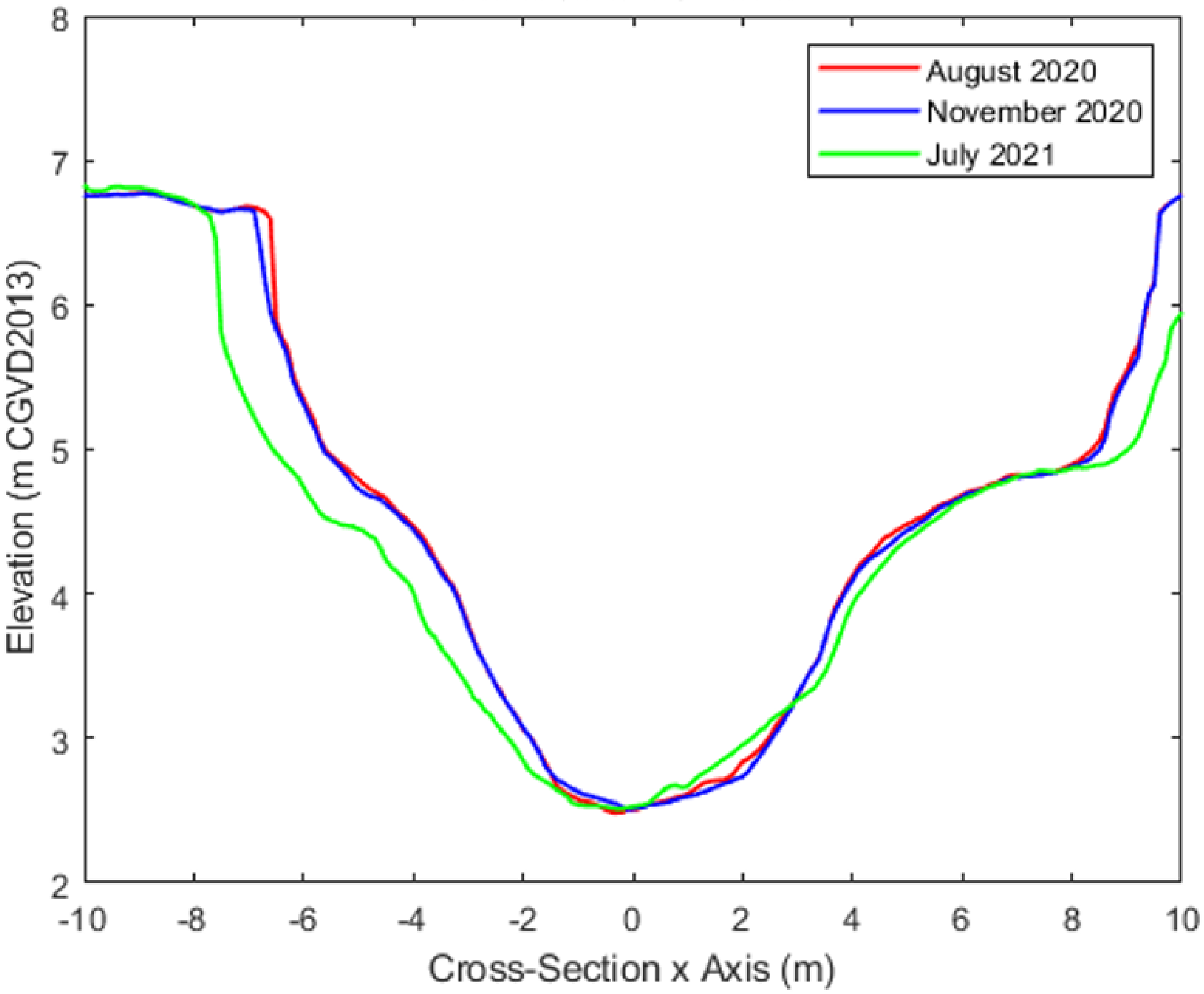

Figure 3.6. Cross-sectional data of inlet for each deployment (Lewis, 2022).

November had the largest tides of all deployments, promoting high velocities, being near the peak of the 206-day perigean-spring tidal cycle (Desplanque & Mossman, 2004), however, the general velocity reduction after August showed the effects of the change in cross-sectional area of the inlet. Figure 3.7 visually shows the evolution of the inlet/V3 area and V3 channel over the study period, where the area widens and becomes more smoothly sloped toward the inlet. This demonstrates the fast-paced morphological changes of MR site inlets and channels caused by the hydrodynamics as the site moves toward a stable equilibrium.

Figure 3.7. Inlet/V3 area for: a) August 2020, b) November 2020, and c) July 2021 deployments (TransCoastal Adaptations, 2020; TransCoastal Adaptations, 2021).

3.1.5 Discharge Rates at Inlet

Comparing the discharge patterns to the velocity patterns, the effects of the cross-sectional area can be seen. Looking at the discharge versus WSE in Figure 3.8, the same patterns can be seen as observed in the velocity curves. Instantaneous discharge rapidly increases from <10 to >20 $m^3 \cdot s^{-1}$ after the WSE reaches bankfull level but did not have the same decrease and increase around full site level as the velocity data did. Generally similar tides had similar discharge values, regardless of velocities, indicating interactions with the cross-sectional area. November 2020 had the highest average and maximum discharge for the flood and ebb tide (Table 3-5). August 2020 and July 2021 had similar maximum flood and ebb discharge values, but August had higher average values, though this is not visually apparent in Figure 3.8.

3.1.6 Suspended Sediment Concentration at Inlet

All deployments had higher SSC values on the flood tide, except for the end of the November tides (Figure 3.9). SSC was highest in November on the flood and ebb tides, where the maximum flood SSC was around 1390 $mg \cdot L^{-1}$ (Table 3-6). July had nearly the same maximum flood values as November, but low ebb values like August. In all deployments, larger tides had higher SSC values, except for the two largest tides in August which had the lowest SSC. The SSC values over the tide were most consistent between the July deployment tides. August had the most variable concentrations between tides, particularly on the flood tide, possibly indicating erosion. The very first value measured in July was not included since it was around twice the value of the highest measurement of all deployments, uncharacteristic of July and other deployments. This may have been a result of contamination upon setup, being the first sample after the setup of the instrument.

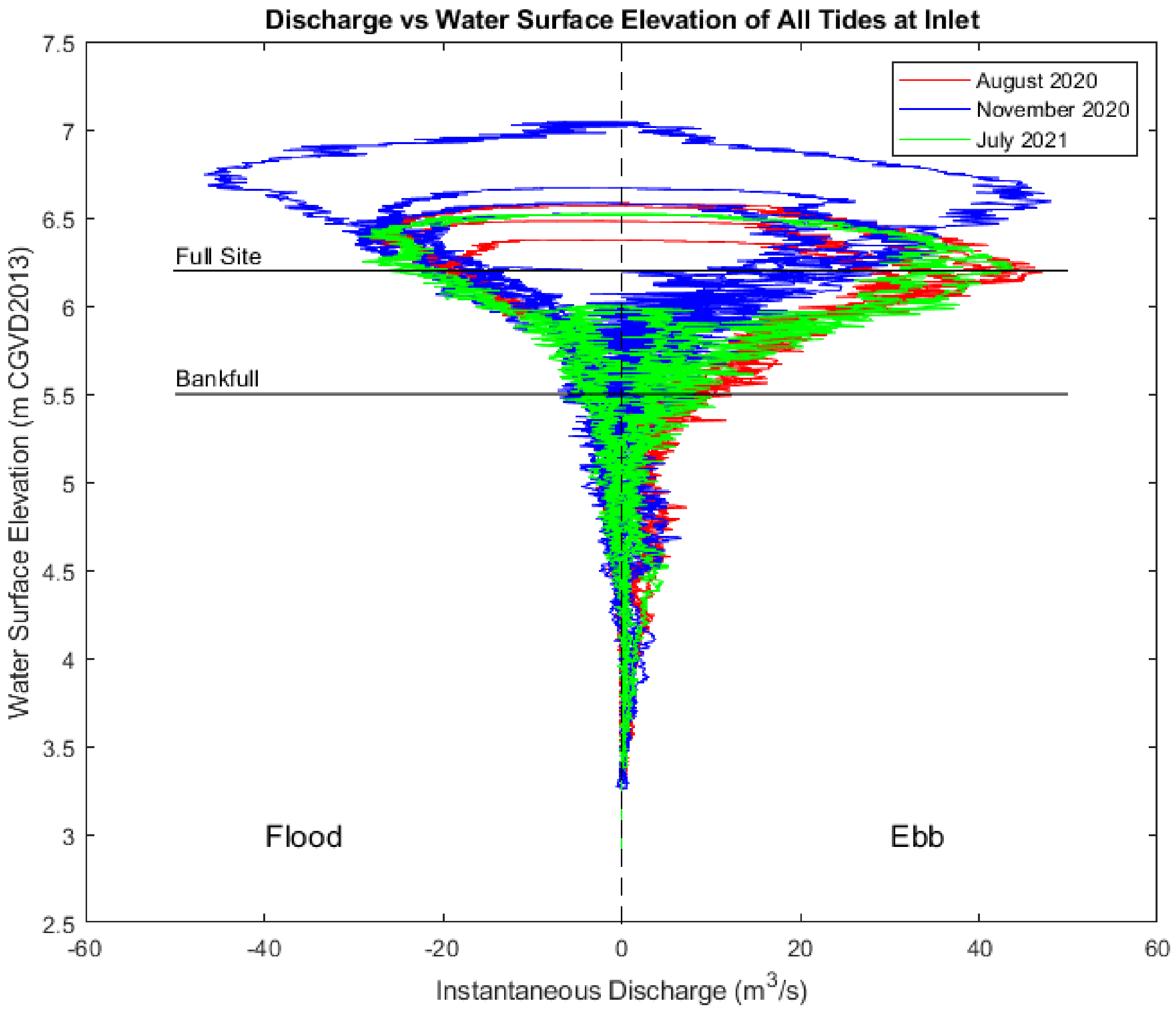

Figure 3.8. Instantaneous depth summed discharge versus WSE over each available tide, overlayed from all deployments with bankfull and full site elevation levels indicated.

Table 3-5. Average and maximum instantaneous discharge values for flood and ebb of each deployment.

Deployment	**Flood**		**Ebb**	
	Avg Discharge ($m^3 \cdot s^{-1}$)	Max Discharge ($m^3 \cdot s^{-1}$)	Avg Discharge ($m^3 \cdot s^{-1}$)	Max Discharge ($m^3 \cdot s^{-1}$)
Aug. 2020	9.63	29.40	10.30	47.10
Nov. 2020	9.17	46.60	7.43	48.20
Jul. 2021	6.84	29.10	6.20	43.90

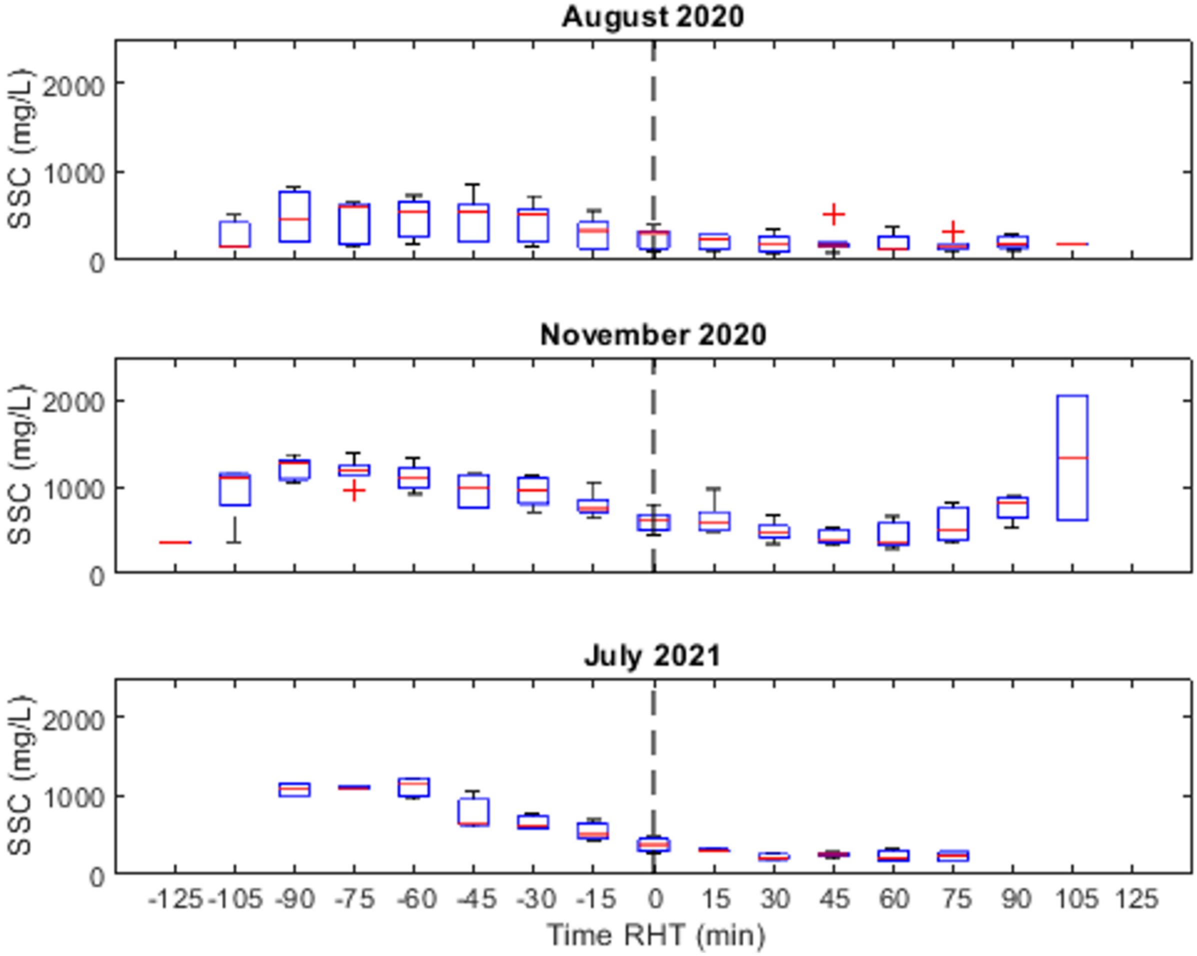

Figure 3.9. Box and whisker plots of inlet SSC distribution of all tides relative to high tide (RHT) for each deployment, with y axis scaled to channel instrument SSC levels.

Table 3-6. Minimum, maximum, and average SSC values of flood and ebb for each deployment.

Deployment	**Flood**			**Ebb**		
	Min SSC (mg·L^{-1})	Max SSC (mg·L^{-1})	Mean SSC (mg·L^{-1})	Min SSC (mg·L^{-1})	Max SSC (mg·L^{-1})	Mean SSC (mg·L^{-1})
Aug. 2020	131	858	455	80.0	526	201
Nov. 2020	358	1390	1010	289	2060	583
Jul. 2021	434	1230	850	161	338	248

3.1.7 Precipitation and Wind

There was little precipitation before or during the August and November 2020 deployments, except for a rainstorm on the last tide of the November deployment, where deposition samples were washed away and/or contaminated. In July 2021 there was no precipitation during the deployment (Figure 3.10), however, the highest precipitation event of the study period occurred two days before. The maximum precipitation rate was 7.9 mm·hr^{-1} and there were 10 hours of consecutive rain greater than 1 mm·hr^{-1}, with eight hours of rain above 2 mm·hr^{-1}, where the 1 to 2 mm·hr^{-1} rainfall threshold increases SSC levels for three days, reported in Dale et al. (2018). This was a 42mm rainfall with 19mm the previous day for a total of 61mm over two days.

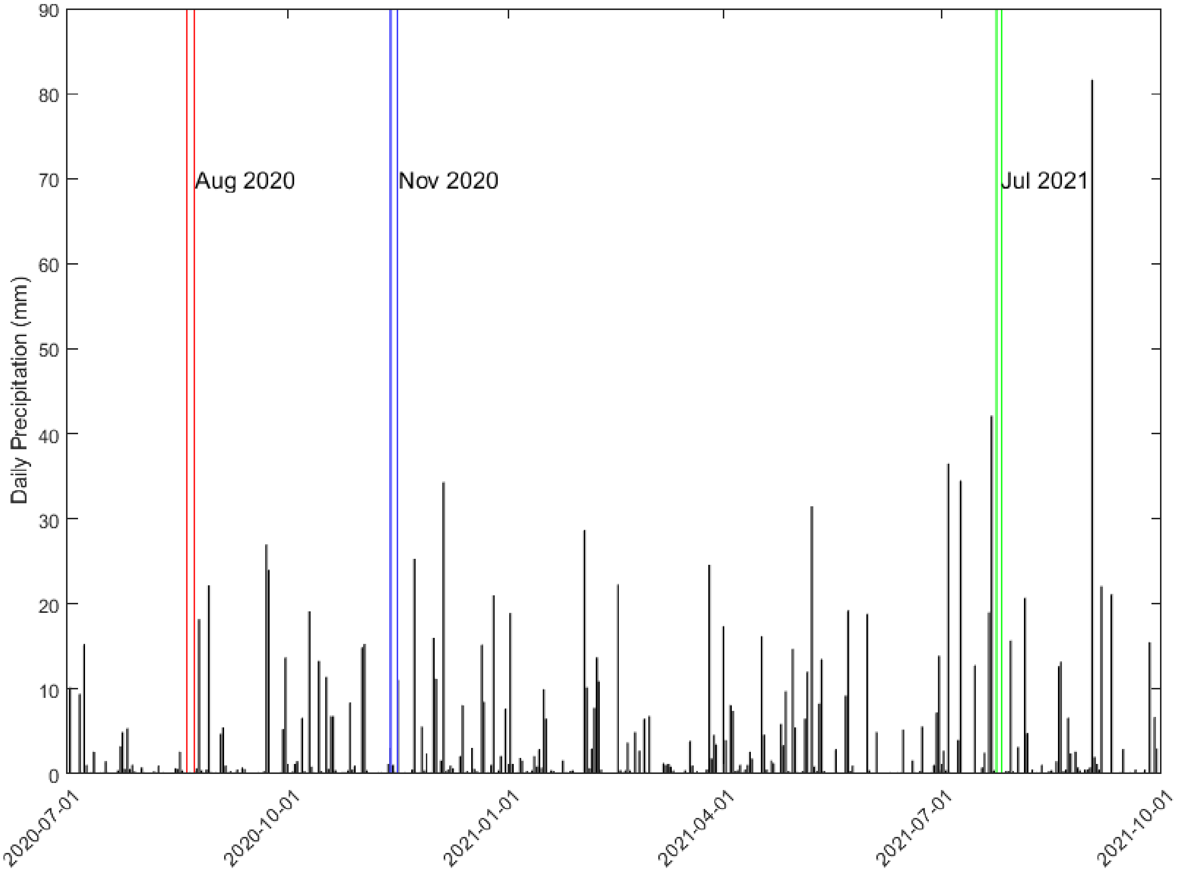

Figure 3.10. Daily precipitation over the study period from Nappan Auto weather station, using data from Environment Canada.

Wind was not directly measured in this study, due to a lack of instrument availability, however wind gust data was available at the Nappan Auto station (Table 3-7). July experienced the lowest maximum wind gusts, and the November deployment experienced the highest. Wind direction was fairly similar for all deployments, predominantly coming from the Southwest (Figure 3.11). In Figure 2.4, the Southwest direction lines up with the longest fetch length of the site, causing small waves observed in the field. This also lines up with the Cumberland basin, causing waves to propagate up the Missaguash river to the site, possibly through the inlet.

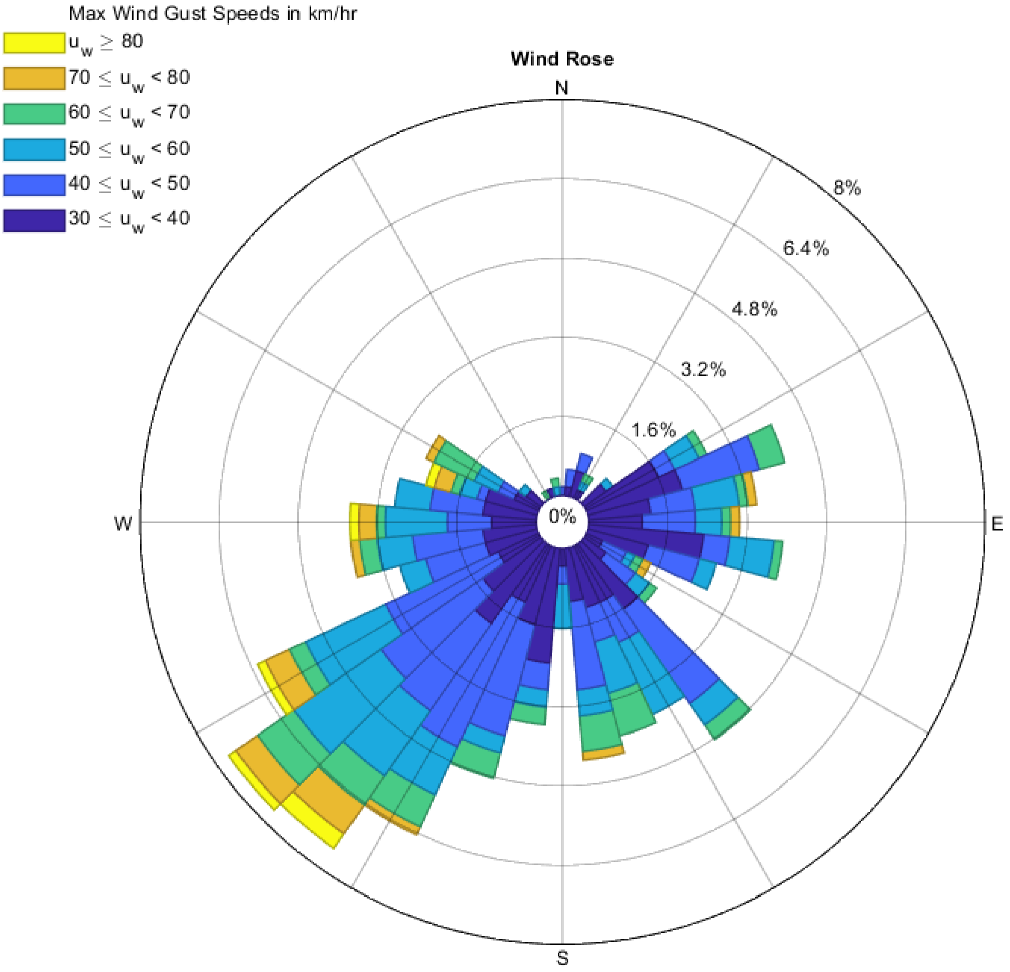

Figure 3.11. Wind Rose of 2020-2021 Nappan, NS maximum wind gust data using MATLAB script from Pereira (2023), using data from Environment Canada.

Table 3-7. Wind data for each deployment, from Nappan Auto weather station, using data from Environment Canada.

Date	**Direction of Max Wind Gust (° from North)**	**Speed of Max Wind Gust (km·hr^{-1})**
Aug 20, 2020	240	48
Aug 21, 2020	230	38
Aug 22, 2020		
Aug 23, 2020	240	48
Nov 13, 2020		
Nov 14, 2020	320	34
Nov 15, 2020	310	42
Nov 16, 2020	150	65
Jul 23, 2021		
Jul 24, 2021		
Jul 25, 2021	170	31
Jul 26, 2021		

3.1.8 Sediment Flux at Inlet

The instantaneous sediment flux compared to the change in WSE exhibited the same patterns as velocity and discharge, though SSC variations between tides had a more noticeable impact in some cases. Over the study period the instantaneous sediment flux varied from a low average of approximately three to four kg·s^{-1} in August to approximately five to nine kg·s^{-1} in November on the flood and ebb tides (Figure 3.12, Table 3-8). All tides had a positive calculated sediment budget (Table 3-9), meaning sediment was imported, except for Tide 1 in August. This and the other tide in August with relatively low instantaneous sediment flux patterns had similar discharge to other tides, but this was overshadowed by low SSC values. The November tides imported the highest amounts of sediment, where Tide 4, the highest tide, imported the most. With only a 0.5m maximum WSE difference from the other tides, it was an order of magnitude higher than the other tides in its influx of sediment. There was also a spike at the end of this tide corresponding with the last SSC value of the tide (the second highest SSC value of all deployments) as the channels drained.

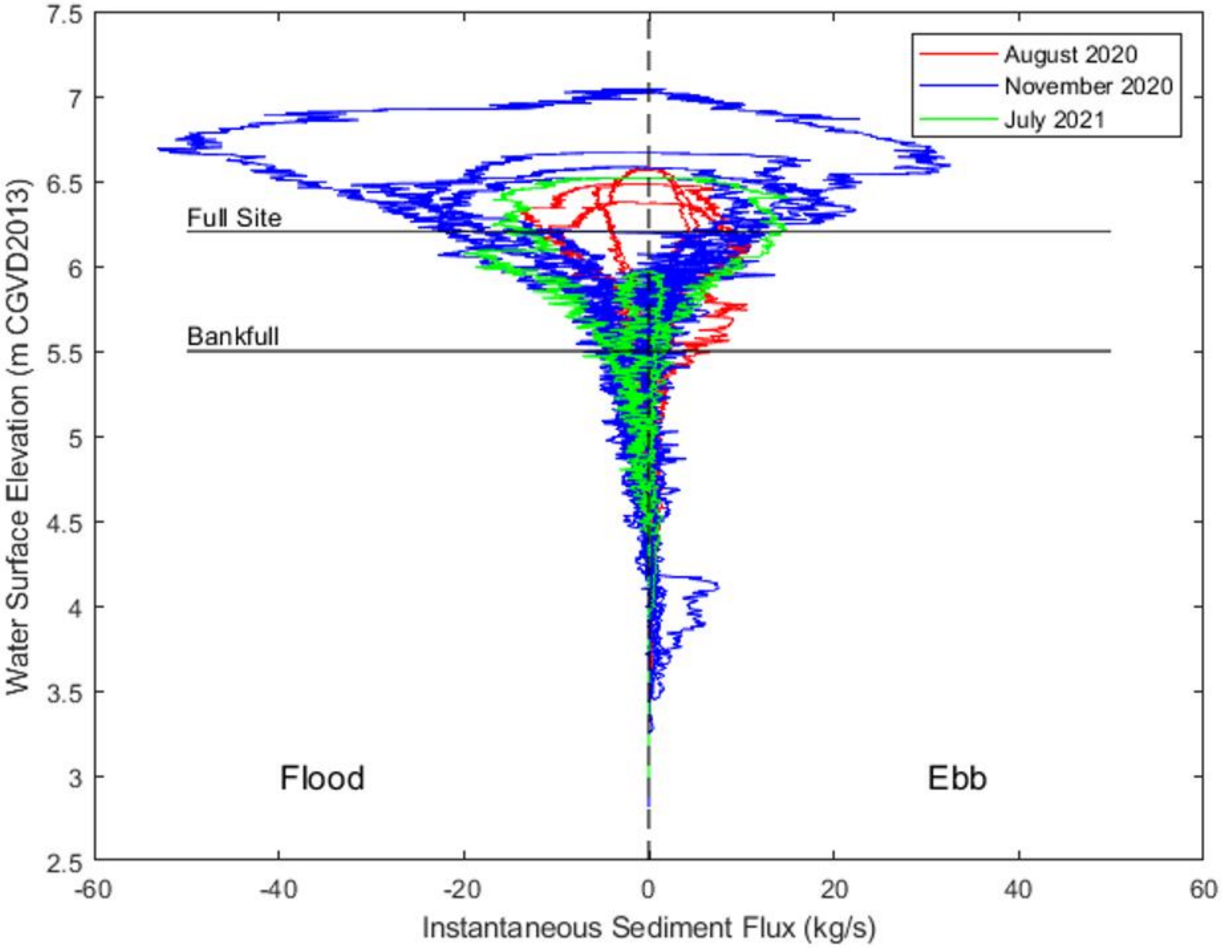

Figure 3.12. Instantaneous sediment flux versus WSE over each available tide, overlayed from all deployments with bankfull and full site elevation levels indicated.

Table 3-8. Average and maximum instantaneous sediment flux values for flood and ebb of each deployment.

Deployment	**Flood**		**Ebb**	
	Avg Sediment Flux (kg·s^{-1})	Max Sediment Flux (kg·s^{-1})	Avg Sediment Flux (kg·s^{-1})	Max Sediment Flux (kg·s^{-1})
Aug. 2020	3.64	14.00	2.61	11.30
Nov. 2020	8.96	53.00	4.82	32.70
Jul. 2021	5.13	20.00	2.86	15.00

Table 3-9. Maximum water surface elevation, total sediment input, output, and sediment budget of each available tide for each deployment.

Tide	Max WSE (m CGVD2013)	Total Sediment Input (kg)	Total Sediment Output (kg)	Sediment Budget (kg)
Aug. T1	6.38	21600	26200	-4580
Aug. T2	6.58	12800	9460	3330
Aug. T3	6.48	30200	22100	8060
Aug. T4	6.56	12700	9680	3040
Nov. T1	6.21	34900	9760	25200
Nov. T2	6.57	72900	35200	37800
Nov. T3	6.51	54700	20100	34600
Nov. T4	7.03	118000	57200	60500
Nov. T5	6.66	75600	34600	41000
Jul. T2	5.97	9670	4850	4820
Jul. T3	6.92	51000	30900	20200

3.2 Channel Conditions versus Inlet Conditions

3.2.1 Current Velocities in Channels

The ADVs in the channel showed similar patterns as the inlet velocity. Station V3, showing the DAV closest to the inlet, has the same rapid shift of flood velocity to ebb velocity as the inlet data (Figure 3.13). The station also showed similar peak flood and ebb velocities of around 0.6 to 0.8 $m \cdot s^{-1}$. The two lowest July tides, however, show very low velocities from 0 to 0.2 $m \cdot s^{-1}$ on the flood and ebb tides, which changed very little over the tide. Station V2, about halfway to the borrow pit, showed similar velocities and patterns, except for the two lowest July tides displaying similar velocities and patterns as the rest of the tides. There was also a slight reduction in velocity before and after high tide at this station. At station V1, furthest from the inlet, and closest to the borrow pit, there was a much more prominent reduction of velocity before and after high tide. This shows that velocity progressively reduces as water gets further from the inlet, where stations were not consistently higher or lower than the other, mostly with only a ~0.2m difference in elevation.

In conjunction with the reduction in velocity, the WSE gets progressively lower, further from the inlet as well during all deployments. There was approximately a 0.5m difference of maximum WSE between the inlet and station V1. This shows that there is a slope in the water surface during the tide, in the channels across the marsh.

3.2.2 Suspended Sediment Concentrations in Channels

The turbidity measured in the channels showed different concentrations of sediment reaching different parts of the site, but with similar tidal patterns as the inlet. The V3 station leading to MH01 and MH03 in Figure 2.4 shows clear differences in SSC patterns between the August and November deployments (Figure 3.14a,b). In this data, high spikes of SSC can be seen during and past the ebb tide, as the site continues to drain, further referred to as “post-ebb”. These spikes in Figure 3.14a were consistent for all August tides.

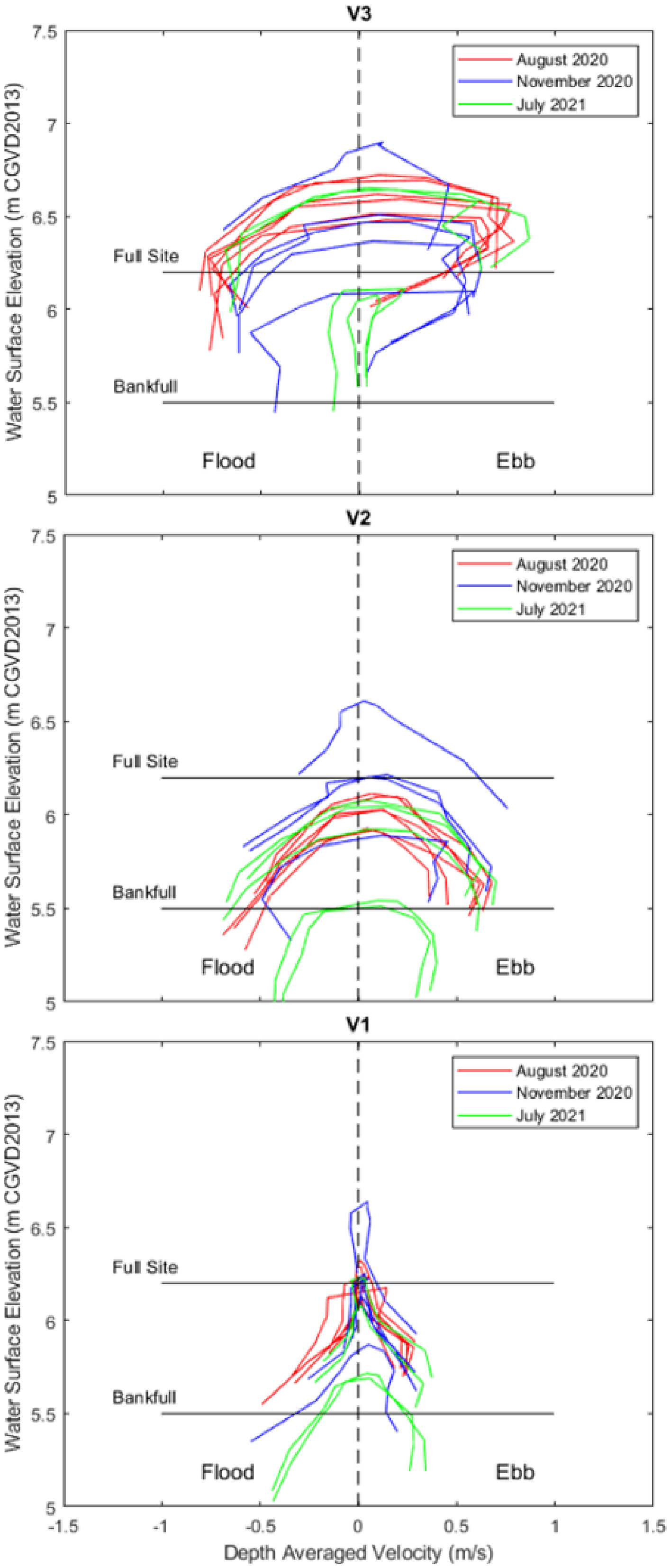

Figure 3.13. DAV versus WSE at channel stations ordered from closest to furthest from the inlet.

These three post-ebb spikes in the August deployment tides correlate to three different surfaces draining. From bankfull to full site level, there are three distinct layers of elevation in this area. The lowest stage being the channels, the second being the agricultural drainage ditching, and the third being the flat sections of previously agricultural field separated by the ditches. In Figure 3.15a, the flood map was made using the June 2020 digital elevation model (DEM), which clearly shows these three layers of elevation. In Figure 3.15b, the flood map was made using the July 2021 DEM, where there has been clear sediment infilling and far less post-ebb SSC spikes in the July 2021 V3 data. Infilling of ditches would reduce the amount of water draining from this location, therefore reducing velocity and erosion, resulting in a reduction of suspended sediment over the deployments in the V3 data.

The R1 station, located close to the inlet, shows the same change in SSC trends as the V3 RBR data (Figure 3.16). However, R1 does not show the same ebb tide and post-ebb patterns, though there are still spikes in all deployments. In July, the readings continue for much longer, as the sensor was at a lower elevation, capturing the post-ebb tide readings and marsh surface drainage SSC levels. Both the V3 and R1 stations had higher SSC than the inlet (Figure 3.9).

The RBR at V1 was located closer to the borrow pit, furthest from the inlet, showing that only a portion of the concentration of sediment travelled to this area of the site (Figure 3.17). The rest likely fell out of suspension due to a reduction in current velocity as the water travelled through the site (Poirier et al., 2017; Reed et al., 1999). V1 also had a shorter inundation time, but the same shaped SSC curve as the other channel stations and inlet. This shows that further from the inlet, SSC is greatly reduced, but maintains the same patterns.

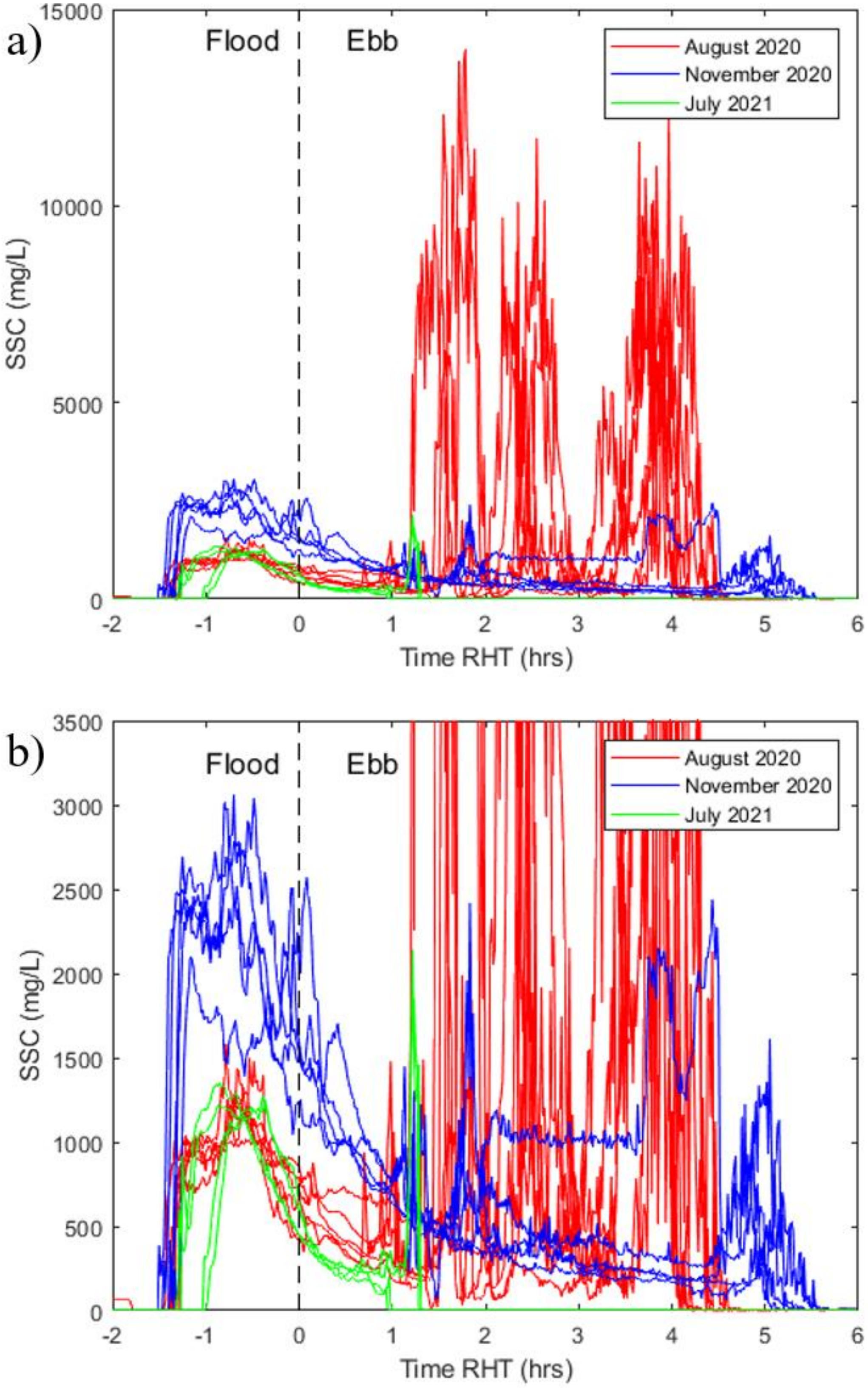

Figure 3.14. Change in SSC over time at V3 for all deployments where a) is scaled to 15000 mg·L^{-1} to show spiking and b) is scaled to 3500 mg·L^{-1}, relative to other SSC scales presented.

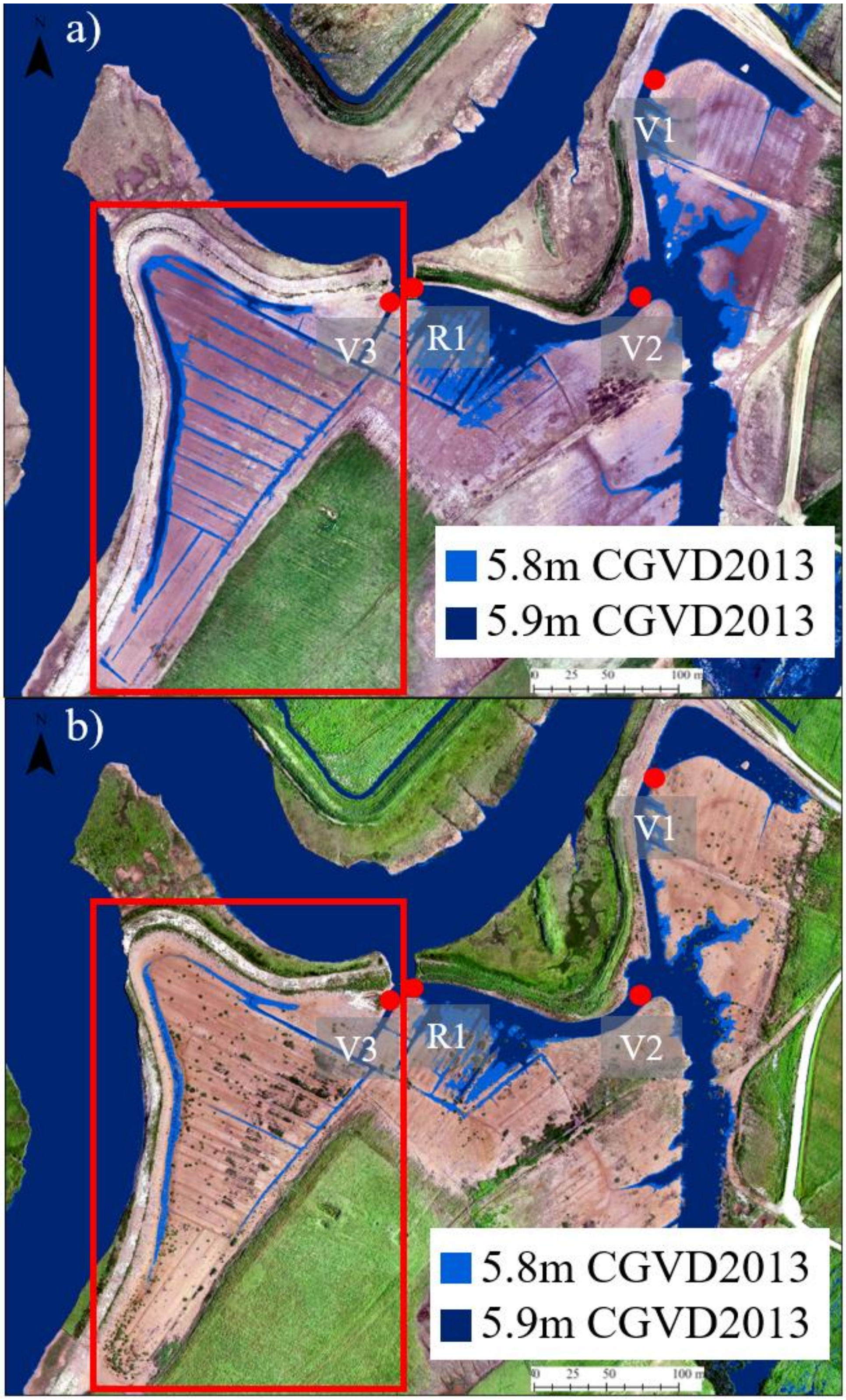

Figure 3.15. Flood maps of 5.8 and 5.9m CGVD2013. Orthomosaic and DEM for flood map created with imaging from a DJI Phantom 4 RTK Remotely Piloted Aircraft System (RPAS), piloted by Samantha Lewis on a) June 1, 2020, and b) July 25, 2021, processed in Lewis (2022).

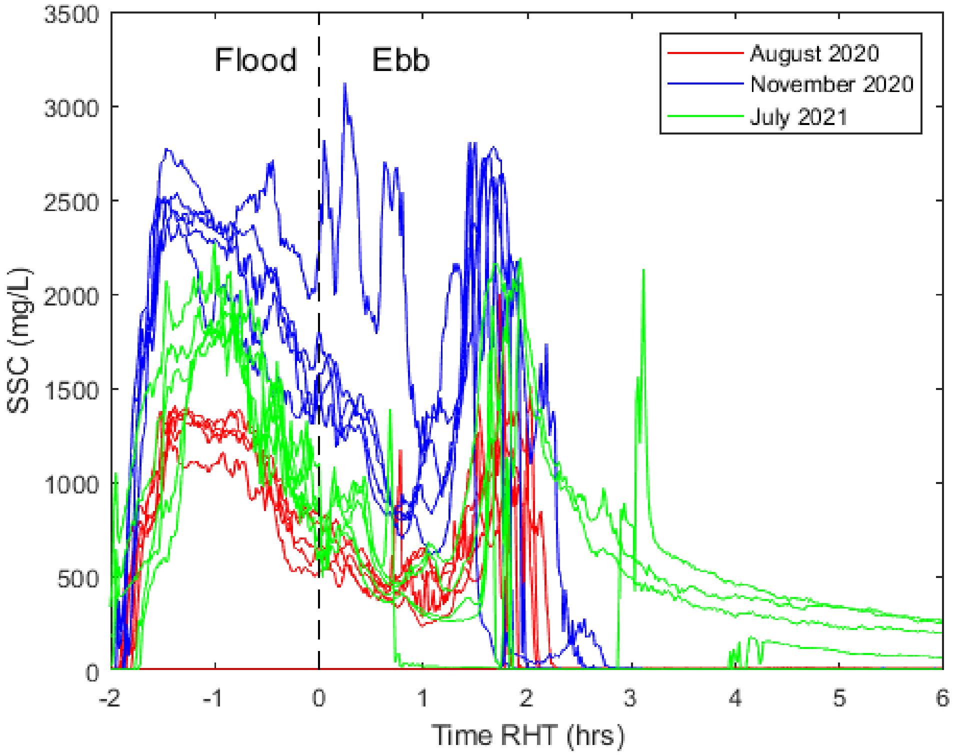

Figure 3.16. Change in SSC over time at R1 station for all deployments.

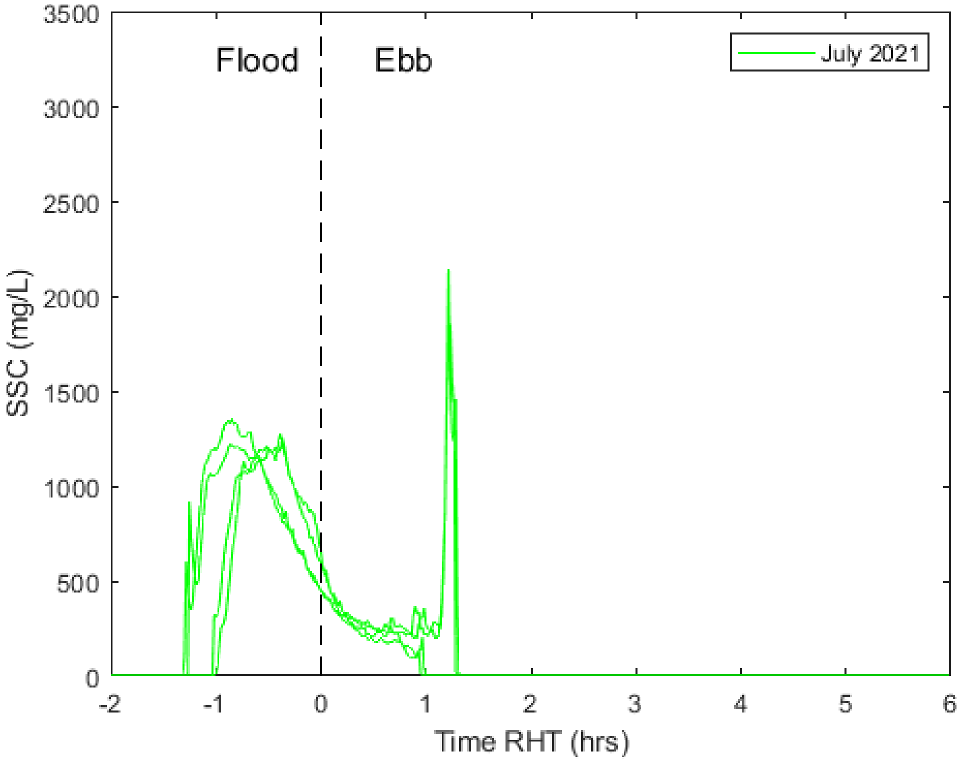

Figure 3.17. Change in SSC over time at V1 for July deployment.

3.3 Temporal Variability of Marsh Surface Deposited and Suspended Sediment

3.3.1 Inlet versus Marsh Surface Suspended Sediment Concentrations

Since the RSBs collected one measurement per tide as the marsh flooded, these values were compared to the average SSC of the flood tides at the inlet (Figure 3.18). The RSB SSC stayed constant until the inlet SSC reached around 800 mg·L^{-1}, where the RSB SSC began to increase. There are few RSB SSC values comparable to the inlet SSC values, except the two tides in August. This showed a decrease in SSC between the inlet and stations, indicating there is settling before the tide reaches the stations. Both the RSB SSC and inlet SSC showed November having the highest SSC, July the second highest, and August the lowest. There are clear connections between the inlet and station SSC levels, however, there are likely other variables influencing this connection.

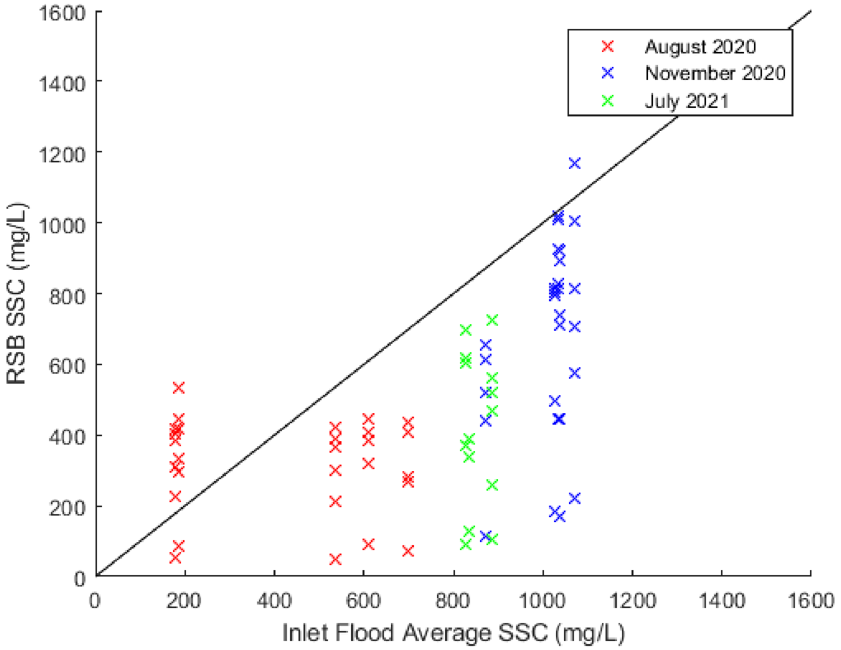

Figure 3.18. Flood Average SSC at inlet versus all RSB SSC stations, separated by deployment with 1:1 ratio line.

3.3.2 Temporal Variations of Marsh Surface Deposited and Suspended Sediment

Deposition from sediment traps varied between tides and deployments, where Figure 3.19a,b are examples of high deposition, and Figure 3.19c is an example of little deposition. Values between stations ranged from 5.2 to 1400 $g{\cdot}m^{-2}$ per tide (Table 3-10) depending on the tide and topographic variables of the stations. Depending on the tide height, some stations were not inundated, and therefore had no deposition or RSB SSC samples. The lowest tide inundated 57% of stations and 6 of the 13 tides inundated the whole site, covering all stations. The lowest tide deposited sufficient sediment for a tile scrape sample for 21% of stations, where only one tide, November Tide 4, deposited enough sediment for a scrape sample for all stations. The two highest elevation stations, MH05 and MH09, only received enough deposition for tile scrape samples after Tide 4 in November, where they received 140 and 250 $g{\cdot}m^{-2}$. November received the most deposition on average and August received the least.

Table 3-10. Maximum, minimum, and average deposition values for each deployment ($g{\cdot}m^{-2}$) per tide.

	August 2020	**November 2020**	**July 2021**
Max	590.0	1400.0	870.0
Min	21.0	5.2	15.0
Average	180.0	310.0	230.0

Deposition had a strong relationship with the RSB SSC, including the temporal variations between tides and deployments. This relationship was also observed to compare how much of the sediment making it to the stations was deposited. As initial SSC increased, deposition increased as well (Figure 3.20), where variations between tides and deployments were similar. One station did not fit this trend; RS6 had the highest initial SSC, but the lowest deposition. November had the highest SSC and deposition, July the second highest, and August the lowest.

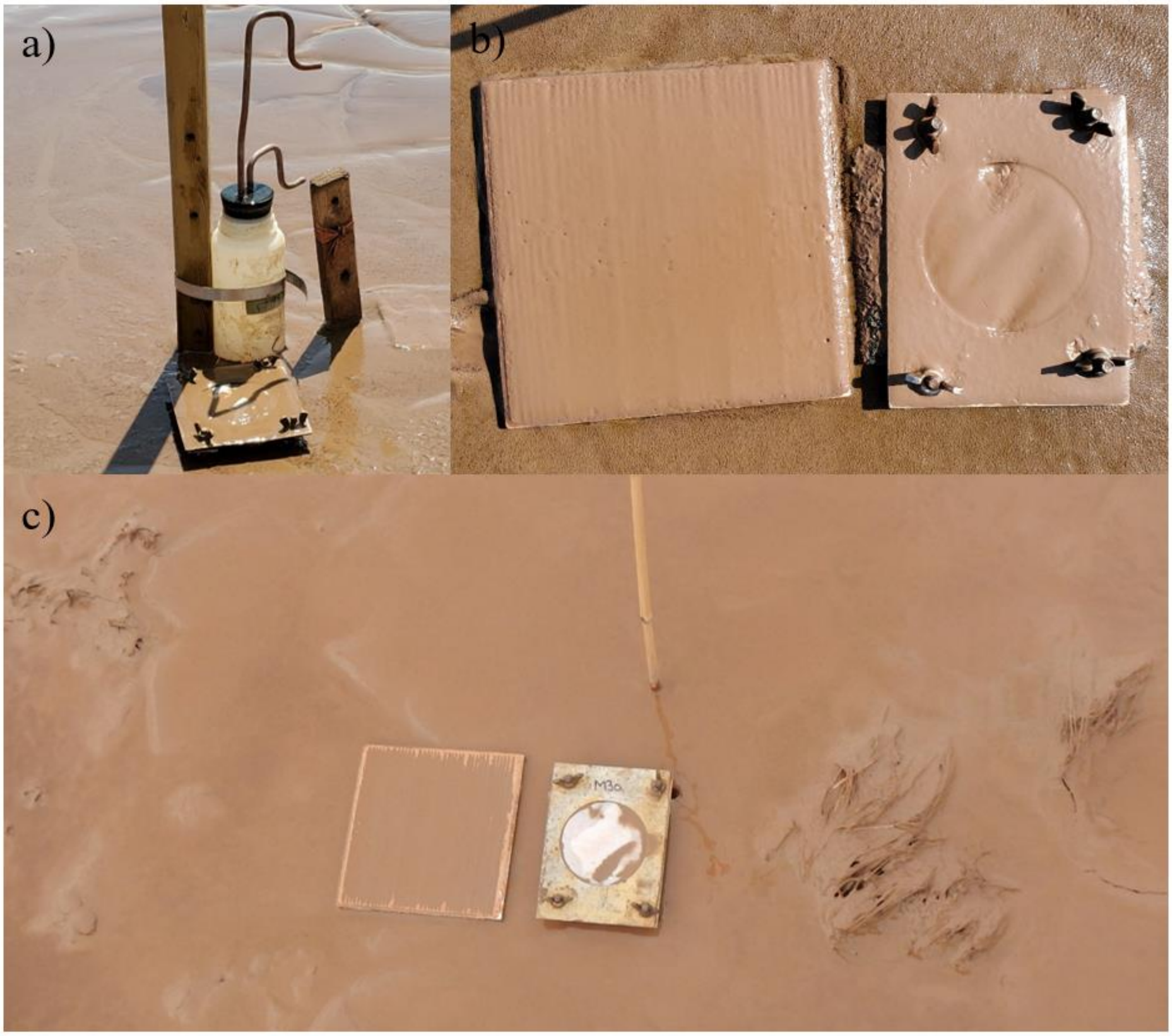

Figure 3.19. Examples of sediment stations with a and b) high amounts of deposition and c) low amounts of deposition. Picture a) was taken at RS2 after July Tide 1, b) taken at MH11 after July Tide 3, and c) taken at MH13 after November Tide 2 (TransCoastal Adaptations, 2020; TransCoastal Adaptations, 2021).

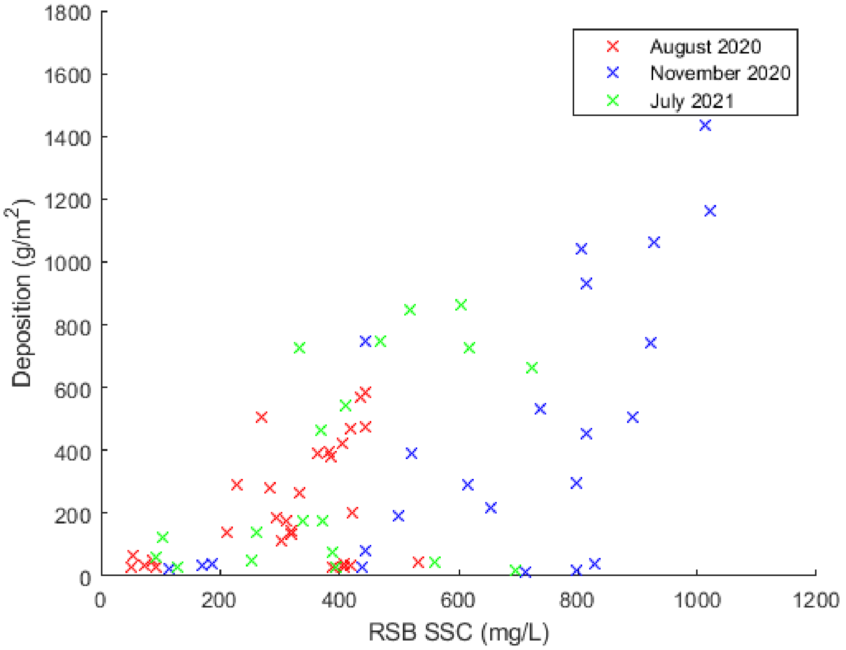

Figure 3.20. Deposition versus RSB SSC of all RSB sediment stations, separated by deployment.

3.4 Spatial Variability of Sediment Deposition and Marsh Surface Suspended Sediment Concentrations

3.4.1 Spatial Variability of Deposition

Stations across the site had varying amounts of deposition with spatial variations and features visualized when mapped. The higher the depositional average, the higher the variability in deposition values at the station seen in Figure 3.21, with the channel system developed in Lewis (2022). The borrow pit, at the northeast side of the site shows progressively less deposition further into the borrow pit, between RS3 and RS1. Stations RS6 and MH17, on the east side of the restoration site, had consistently lower deposition than other stations. These stations were located in an area with few channels. These few channels were classified in Lewis (2022) as relic channels from the historical salt marshes before the dyking of the area.

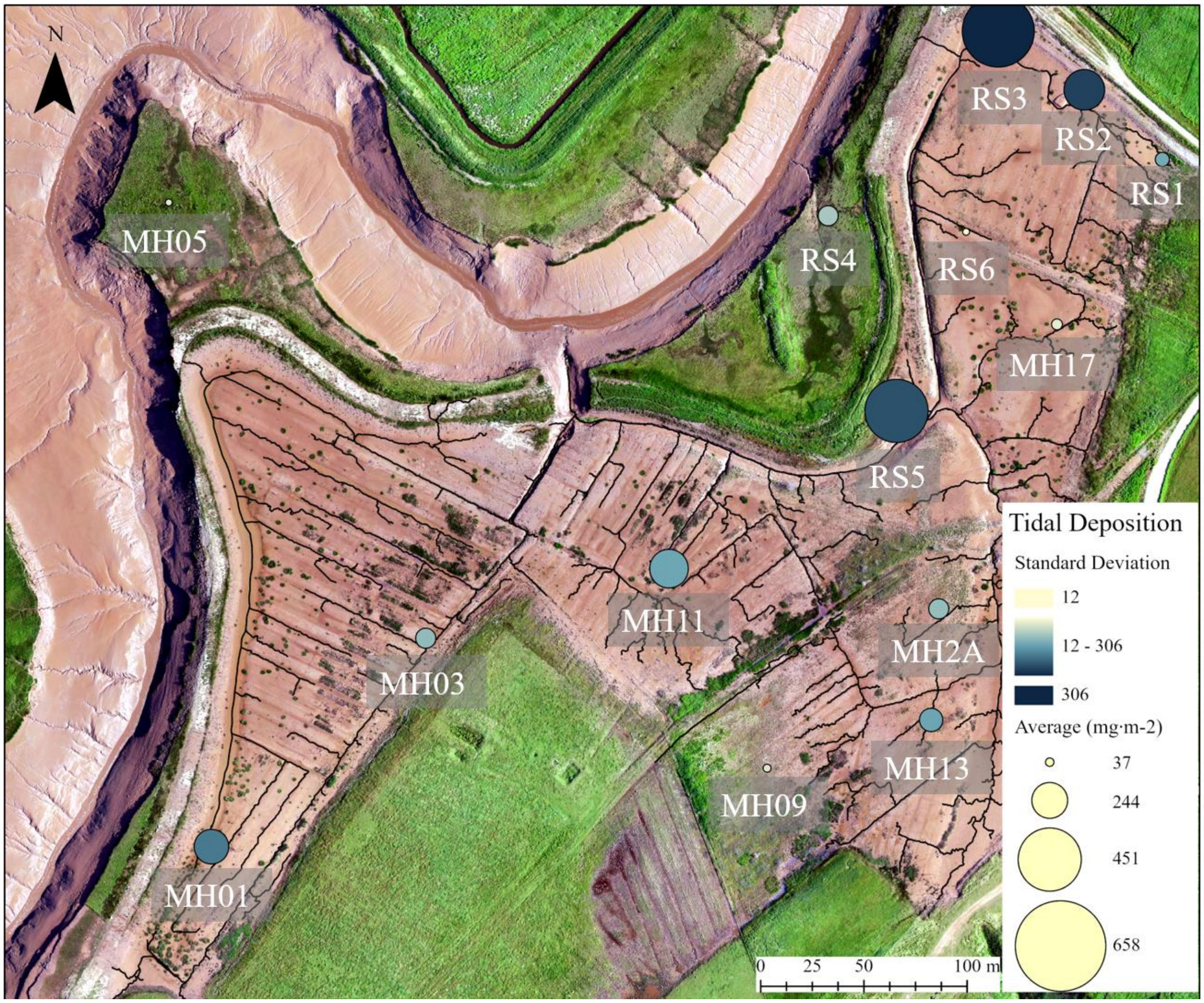

Figure 3.21. Average deposition in g·m^{-2} and standard deviation for all deployments. Orthomosaic created with imaging from a DJI Phantom 4 RTK RPAS, piloted by Samantha Lewis on July 25, 2021, processed in, with channel system shape from, Lewis (2022).

The average D50 and floc fractions from the tidal deposition scrape samples in Figure 3.22 represent the characteristics of the material deposited by the tides at each station. Most stations have similar D50 and floc fraction values, in the medium to coarse silt range around 0.7 to 0.9 mm with 78% to 91% flocculated material. MH05 and MH09 had only 1 scrape sample each out of all deployments: Tide 4 in November, where the D50 and floc fraction values were both very low. The stations RS6 and MH17 had very high D50 values and low floc fractions.

There were also variations seen in the grain size distributions between tides and deployments (Appendix A). In November the grain size was coarser for all stations and in July the grain size was finer than August and November for all stations.

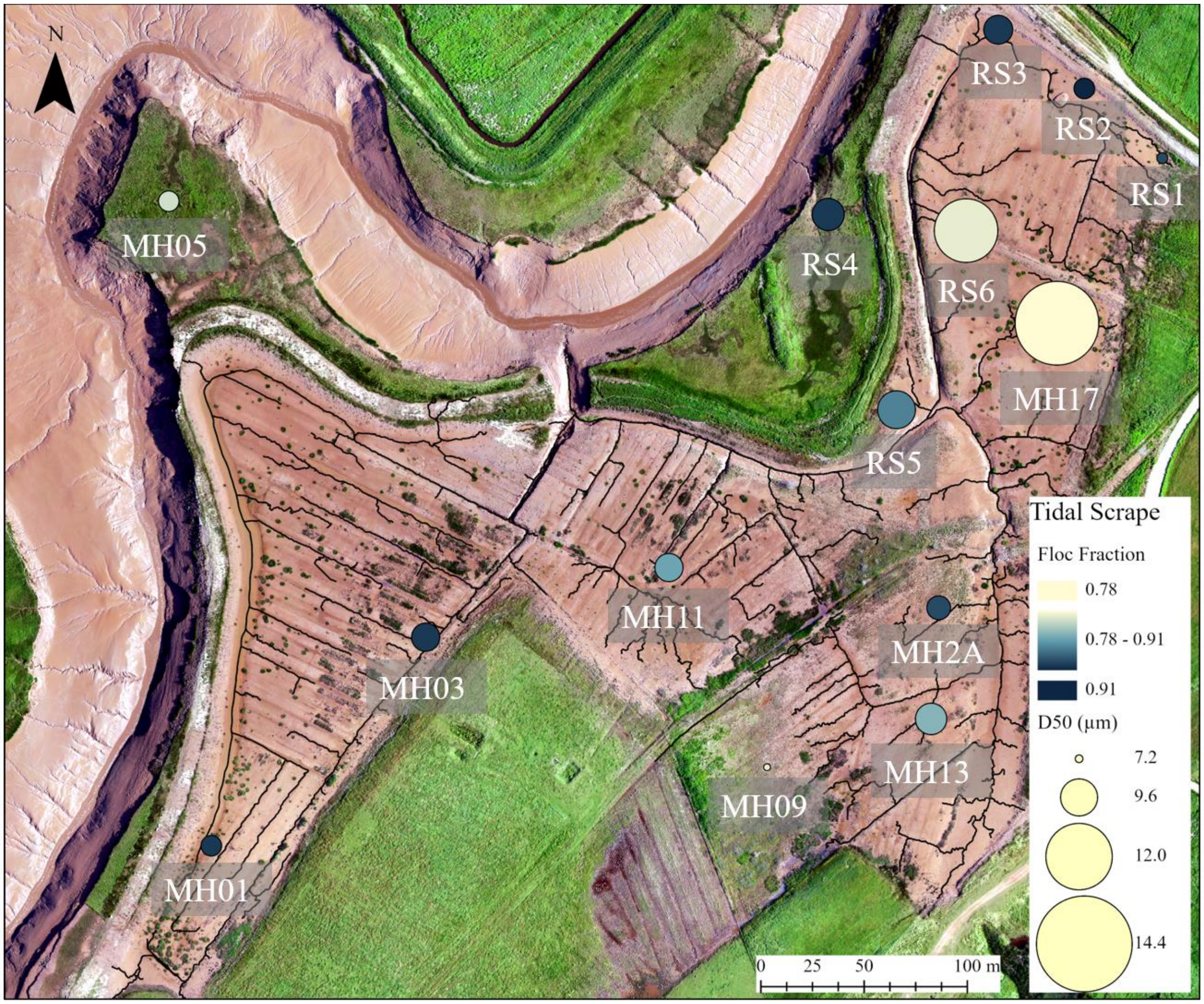

Figure 3.22. D50 (µm) and floc fraction averaged for all deployments. Orthomosaic created with imaging from a DJI Phantom 4 RTK RPAS, piloted by Samantha Lewis on July 25, 2021, processed in, with channel system shape from, Lewis (2022).

3.4.2 Suspended and Deposited Grain Size Distributions

Grain size distributions and floc fractions of the inlet and RSB suspended sediment and the deposited material allowed comparison between the characteristics of the incoming sediment, the sediment reaching the stations, and the deposited material. The grain size was coarsest at the inlet (Appendix A), the RSB sediment was finer and finally, the deposited sediments had a coarser distribution than the corresponding RSBs (Appendix A). The grain size distribution of the deposited sediment was proportional to the distribution of the RSB sediment at the station, where coarser RSB samples had coarser deposition. This pattern was the same for all RSB stations, except RS6, where the RSB grain size and floc fractions were similar to other stations, but the deposited sediment was very coarse with low floc fractions. RS5 had the smallest difference between the deposited sediments and SSC. At the inlet for August and November, there was coarser material on the flood tide, and coarser material overall in November.

3.4.3 Topographic Variables and Deposition

Deposition depended on a number of topographic factors including elevation, distance from channel (Dc), distance from inlet (Di), and surrounding topography. In Figure 3.23, all deposition values for each deployment are displayed compared to the station elevation, where the amount of deposited sediment is shown to decrease with increasing elevation. Dc and Di appeared to have curved, nonlinear relationships with deposition, where deposition was highest within a certain range (Figure 3.24). The nearest and farthest stations from the channels had the lowest deposition and stations three to eight metres from the channel had the highest deposition. Deposition increased with distance from inlet until it peaked around 350m, where deposition decreased with increasing distance from the inlet (Figure 3.25). RS6 did not follow the same trends for elevation or Di and MH17 followed none of the same topographic variable trends as the other stations.

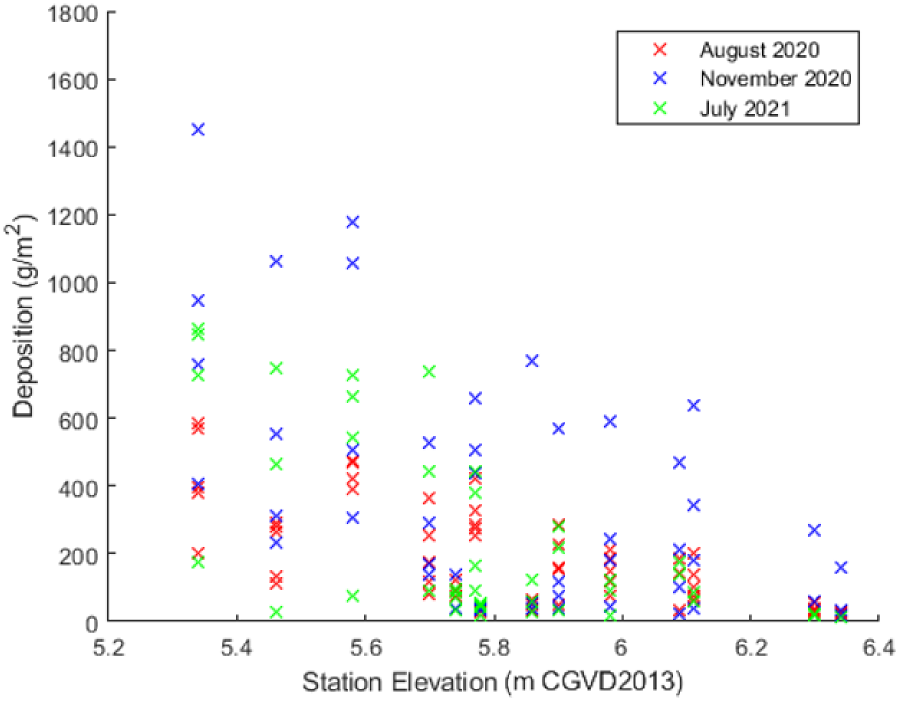

Figure 3.23. Deposition per tide versus station elevation, separated by deployment.

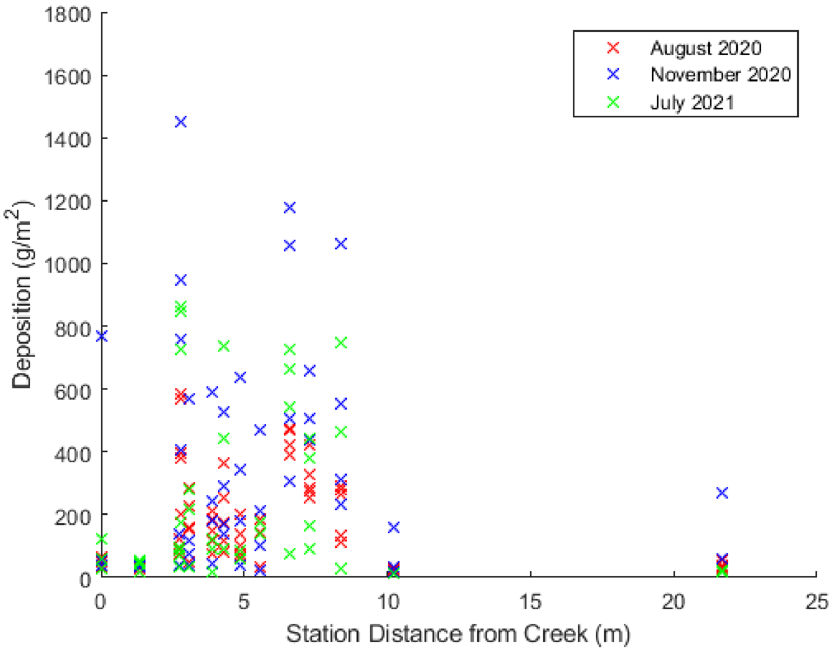

Figure 3.24. Deposition per tide versus Euclidean distance of station from channel, separated by deployment.

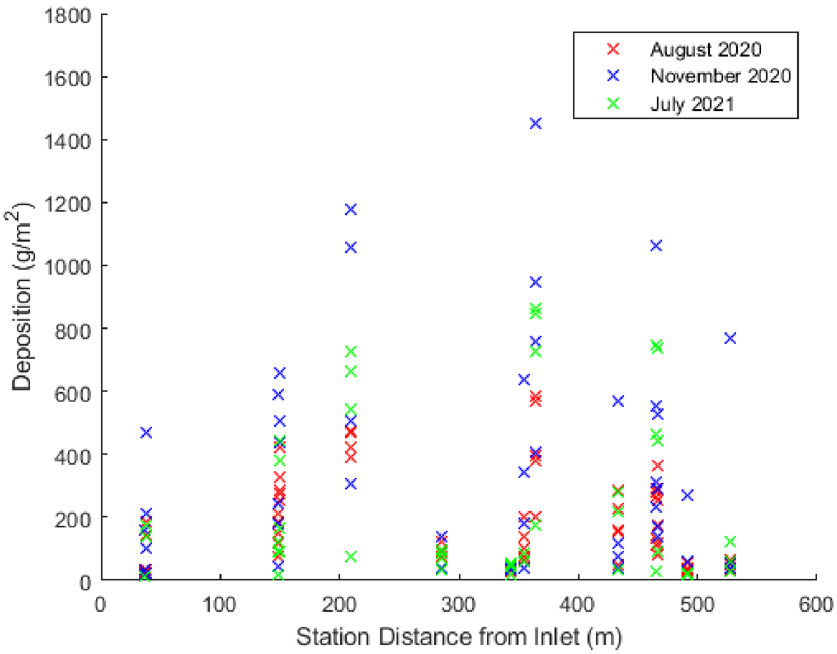

Figure 3.25. Deposition per tide versus distance of station from inlet, following channel system, separated by deployment.

3.5 Statistical Models of Predicting Deposition

In the statistics portion of this analysis, three models were proposed: the modified Temmerman et al. (2003), hydrologic and topographic variable (Hydro/Topo) model and the PMTH model. The Hydro/Topo and PMTH models resulted in the best variables to use and the best interactions between them for predicting deposition for the proposed variables of the models. The modified Temmerman et al. (2003) model was a working model as well, providing comparison for the other models, though it was not as predictive with this dataset as the other models.

There were 16 planned tides, with 14 stations, resulting in 116 deposition samples measured with all hydrologic variables available. RS6 and MH17 stations were removed from the statistical analysis, as they did not follow any of the topographic trends, which left 98 deposition data points. For all steps combined, there were 820 official models tested (Appendix B Table B-1 to Table B-8), with more models tested while steps were formulated and adjusted.

3.5.1 Singular Variable Regressions

Topographic variables Dc and Di had nonlinear, curved patterns when plotted with deposition, so polynomial and similar shaped regressions were tested. Additionally, since some variables affect other variables that contribute to the sediment flux (Figure 2.10), therefore multiplying their effects, it was hypothesized that polynomial regressions would be the best regressions. For example, cross-sectional area affects velocity and velocity affects SSC, where all these variables affect sediment flux. If velocity and SSC are a function of cross-sectional area, then cross-sectional area goes into sediment flux three times, meaning sediment flux is a function of the cross-sectional area cubed. Initially, each variable for the Hydro/Topo and PMTH models was tested for their conditional R^2 values for each regression to determine what regression should be used in the models. Most of the highest R^2 regressions were third order polynomials, as seen previously in the visualization of Dc and Di. To simplify the models, only polynomial regressions were used, however, because of overfitting from too many terms, linear model alternatives were tested as well. This allowed models with more variables and multiplication of variables to be tested, broadening the analysis.

3.5.2 Hydrologic Variables

The model with the lowest AIC from each level of hydrologic variables and the alternative formulas that had AIC values within the same range, were taken as the best hydrologic formulas (Table 3-11). The formulas with only one variable had polynomial regressions since models with more than one polynomial variable were overfitted and did not converge. Models with more than two variables needed the variables to be added to work. In all hydrologic variable levels, the constituents were favoured over the resultant, e.g., discharge and SSC were favoured over sediment flux, except for the cross-sectional area, which was always favoured.

Table 3-11. Best hydrologic variable formulas, judged by AIC value.

Hydrologic Formula		**AIC**
$Dep \sim Area + Area^2 + Area^3$	*	98.7
$Dep \sim Area * Velocity$	*	98.9
$Dep \sim Widths + Depth + Velocity + SSC$	**	99.4
$Dep \sim Area * SSC$	*	98.9
$Dep \sim Widths + Depth + SSC$	*	100.8

*Average of cumulative flood and cumulative ebb of each variable
**Net of cumulative flood and cumulative ebb of each variable

3.5.3 Topographic Variables

Since there were so few topographic variables and elevation had a linear correlation in the singular variable regression step, elevation was kept linear, while Dc and Di were tested, mixed as linear and polynomial. Equation 3-1 was the best overall topographic formula with the lowest AIC value. In the first step of the statistical analysis, Di and Dc were strongest as polynomial regressions. In the best topographic formula Di had a linear regression, since Dc had a stronger polynomial regression and only one variable could have a polynomial regression for the model to work.

Equation 3-1. Best topographic formula, judged by AIC value.

$$Dep \sim Elevation + (Dc + Dc^2 + Dc^3) * Di$$

3.5.4 Individual Hydrologic and Topographic Variables

This step showed how each topographic variable combined best (added or multiplied) with each hydrologic variable for the variables found in the best hydrologic formulas (Table 3-12). These results showed that elevation and Di were best added to all variables, and therefore were best added to all the hydrologic formulas, except for PMTH. Dc was better either added or multiplied depending on the hydrologic variable, so models were produced for each option, adding or multiplying Dc to the entire formula. Di was also best added to any formula, so when formulas were combined, Dc was multiplied by both the hydrologic formula and the added Di, explained in section 2.5.5.2.

Table 3-12. Best combinations individual topographic and hydrologic variables.

	Elevation	**Dc**	**Di**
Area	add	multiply	add
Depth	add	multiply	add
Widths	add	add	add
Velocity	add	multiply	add
SSC	add	add	add
PMTH	multiply	multiply	multiply

3.5.5 Final Models

The Hydro/Topo and PMTH models were constructed using the hydrologic and topographic formulas and their interactions from the previous step. There were two models that were equivalent and had significantly better fit than all other models (Table 3-13). The Hydro/Topo models had the best (lowest) AIC values of 58.8 and 66.2, followed by the PMTH model with an AIC of 107.7. The Hydro/Topo models and the PMTH model were all statistically significantly better than the modified Temmerman et al. (2003) model, which returned as overfitted. Because of this, the modified Temmerman et al. (2003) was removed from further consideration. The post-analysis test of the Temmerman et al. (2003) model using the tidal intensity (H) instead of just elevation was slightly better, but the Hydro/Topo and PMTH models were still statistically significantly better. The Hydro/Topo models were significantly better than the PMTH model, since the PMTH model is unique, only using topographic and predicted variables, the model was kept for analysis.

The marginal R^2 was 0.799 and 0.786 for the Hydro/Topo models, accounting for around 79-80% of the variation in deposition for just the fixed effects. This value was 0.643 for the PMTH model, accounting for 64.3% of deposition. The conditional R^2 values of the Hydro/Topo models were 0.817 and 0.801, meaning they both accounted for around 80-82% of the variation in deposition for both fixed and random effects. The PMTH model had a value of 0.749, accounting for 74.9% of the variation in deposition.

Table 3-13. AIC and R^2 values of best Hydro/Topo models and best PMTH model, judged by significance.

	AIC	**Conditional R^2**	**Marginal R^2**
Area/Velocity	58.8	0.817	0.799
Area/SSC	66.2	0.801	0.786
PMTH	107.7	0.749	0.643

The two equivalent Hydro/Topo models were the same formula and variables, but one had velocity and the other had SSC in the equation (Equation 3-2, Equation 3-3). The other variables in these models were area, elevation, Dc, and Di. The PMTH model had PMTH as a polynomial, multiplied by elevation plus Di and Dc^3 (Equation 3-4), which was the best polynomial term for Dc in this model. PMTH was stronger than Dc as a polynomial.

Equation 3-2. Area/SSC model formula.

$$Dep \sim Area_{avg} * Velocity_{avg} * (Dc + Dc^2 + Dc^3) + Di * (Dc + Dc^2 + Dc^3) + Elevation$$

Equation 3-3. Area/Velocity model formula.

$$Dep \sim Area_{avg} * SSC_{avg} * (Dc + Dc^2 + Dc^3) + Di * (Dc + Dc^2 + Dc^3) + Elevation$$

Equation 3-4. PMTH model formula.

$$Dep \sim (PMTH + PMTH^2 + PMTH^3) * Elevation + (PMTH + PMTH^2 + PMTH^3) * Dc^3 * Di$$

3.5.6 Final Model Interactions of Variables

In both Hydro/Topo models, elevation, Dc polynomial terms, and SSC had negative correlations with deposition, where deposition decreased with the increasing variable. This is shown in Figure 3.26 visualizing the Area/Velocity model as an example with all terms and interactions. Also in both models, the area, velocity, and Di had positive correlations; as the variable increased, deposition increased as well. In the PMTH model, the PMTH polynomial terms had both positive and negative correlations, and elevation, Dc^3, and Di all had negative correlations. Dc interacted with all variables except elevation. Area interacted with SSC and velocity as well. Di only interacted with Dc, and elevation interacted with no variables. In the PMTH model, all variables interacted with PMTH.

The largest coefficients in both Hydro/Topo models were the Dc*Di (positive correlation) and Dc polynomial terms (negative correlation) (Tables B-9 to B-11, Appendix B).

These terms have the largest impacts on predicting deposition for this dataset. In the PMTH model, Di*Dc*PMTH^2 and the PMTH*Dc terms had the largest, positive correlations, and Dc*PMTH^2 had the largest negative correlation.

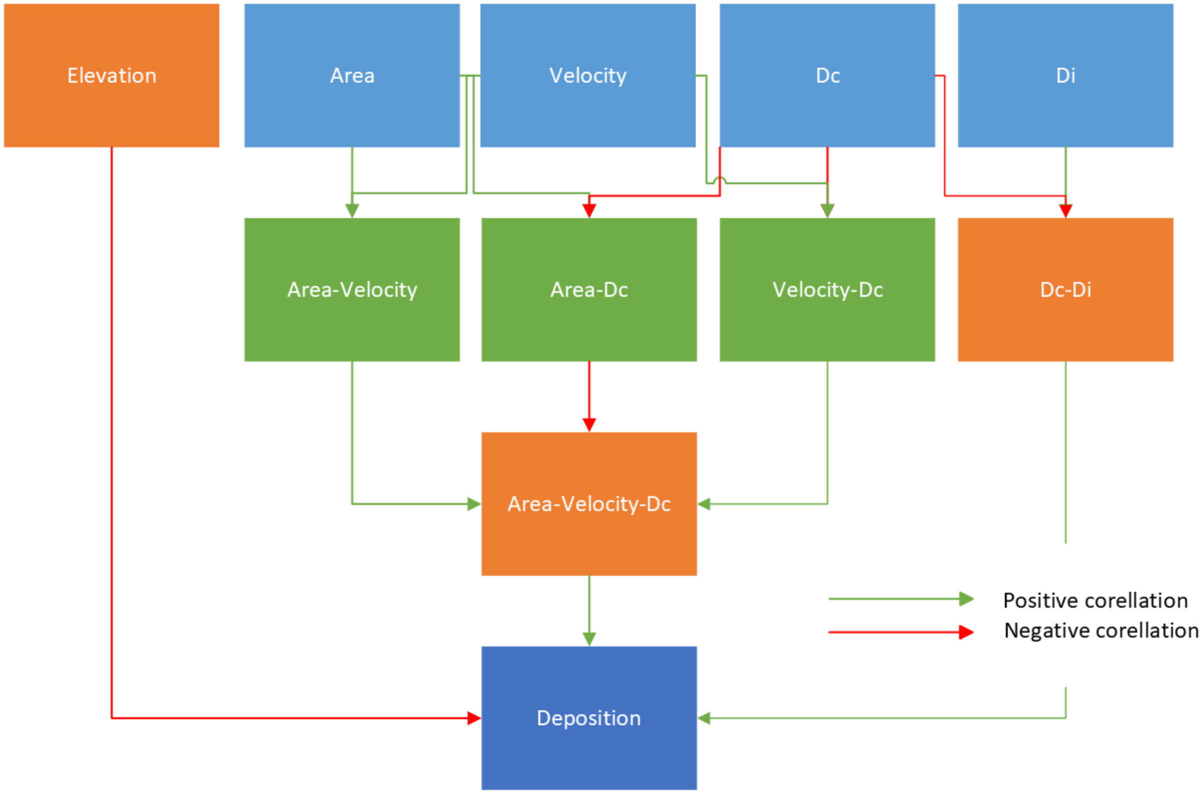

Figure 3.26. Conceptual chart of Area/Velocity model terms and positive/negative correlation, where Dc is distance from creek and Di is distance from inlet.

CHAPTER 4 DISCUSSION

The results of this study showed the interconnectivity of the hydrodynamics, topography, and sediment patterns through similar spatial and temporal variations, statistically linking associated variables. This chapter will further define these connections and statistics by discussing the temporal variations of hydrologic variables at the inlet and spatial and temporal variations of deposition on the marsh surface. These will then be related with channel data to show the connection between inlet hydrodynamics and deposition patterns on the marsh surface. It will then be discussed how this connection can be used to model deposition, and how this changed over Year 2 and Year 3 of restoration at the Converse site. Model validation, limitations, potential improvements, and future use of the models will be discussed.

4.1 Temporal Variations of Inlet Hydrologic Variables and Morphology

Temporal variations of water surface elevation (WSE) shaped the visual and statistical analyses of this study, helping describe the hydrologic-topographic interactions on the managed realignment (MR) site and analyze the use of predicted tides for deposition models. The temporal variations of the other inlet variables showed the effects of the morphological changes at the inlet on the hydrology as the MR site developed over one year of restoration. Variables affecting SSC and the sediment flux included the size of the tides, the velocity affected by the tide height and cross-sectional area that changed over the study period, and precipitation.

4.1.1 Water Surface Elevation Interactions with Topography

Initial observations show the change in WSE, as well as velocity changes, were inconsistent over time, with visible distortions in the bankfull to full site range. This change in hydrodynamics was more visible in the velocity data, as the tide interacted with the site topography, commonly seen in natural marshes (Bayliss-Smith et al., 1979; Davidson-Arnott et al., 2002; Hill et al., 2013; O'Laughlin & van Proosdij, 2013; Reed et al., 1999; van Proosdij, 2001). Keulegan (1967) first explained that narrow, shallow, and long basins have a non-uniform change in water level due to the incoming tidal water being affected by the basin shape. This describes the Converse site in both the topography in relation to the tidal range, and the change in WSE patterns seen at the inlet, as well as the surrounding area in the Bay of Fundy. The reflections of the interactions of the tide with the topography of the site merited further investigation into the use of inlet conditions for sediment modelling on MR sites.

Tides that flooded the whole site had similar inundation times despite having different maximum WSE's. This indicated that there are interactions between the tide and the shape of the bay and river before the tide reaches the site. These observations led to the use of the cumulative value of the variables for each tide for the statistical models, resulting in the Hydro/Topo models explaining ~80% of the deposition.

4.1.2 The Use of Predicted Maximum Tide Height for Models

The predicted maximum tide height (PMTH) has a large dataset, available from the Canadian Hydrographic Service for 12 months into the future, making this variable useful for predicting cumulative deposition over a longer time period. However, it is not as accurate as describing the tide using measured variables. Depending on how far the predicted tide station is from the MR site, the PMTH is likely less accurate due to tide-basin interactions, storm surges, atmospheric conditions, and other environmental factors. This is demonstrated in Figure 4.1, where the PMTH values corresponding to the deployment tides are shown with the actual measured maximum WSE values. The 1:1 ratio line shows the differences between the predicted and measured values, showing that the PMTH is somewhat reliable for statistical models, but has clear error due to environmental factors. The PMTH differed from the expected tide height by ~ 0.4 m to –0.2 m. The maximum tide height was also shown to be a less accurate representation of the tide for the purposes of the statistical models in this study, further arguing PMTH is less accurate for model use. Despite this and the predicted versus measured error, the PMTH model with topographic variables still accounted for 75% of the variability of deposition for fixed and random variables and 64% for just the fixed variables. This shows PMTH is usable for deposition prediction but requires assessment of error.

In a literature review, no studies were found using predicted tide heights from a station off-site for predicting deposition. Previous deposition and accretion models use on-site measured, reported, or estimated hydrologic variables and/or SLR estimates (Best et al., 2018; Butzeck et al., 2015; D’Alpaos et al., 2011; Schile et al., 2014; Temmerman et al., 2003). The rougher longer-term deposition estimates that can be provided by the PMTH model are further discussed in section 4.5.2.

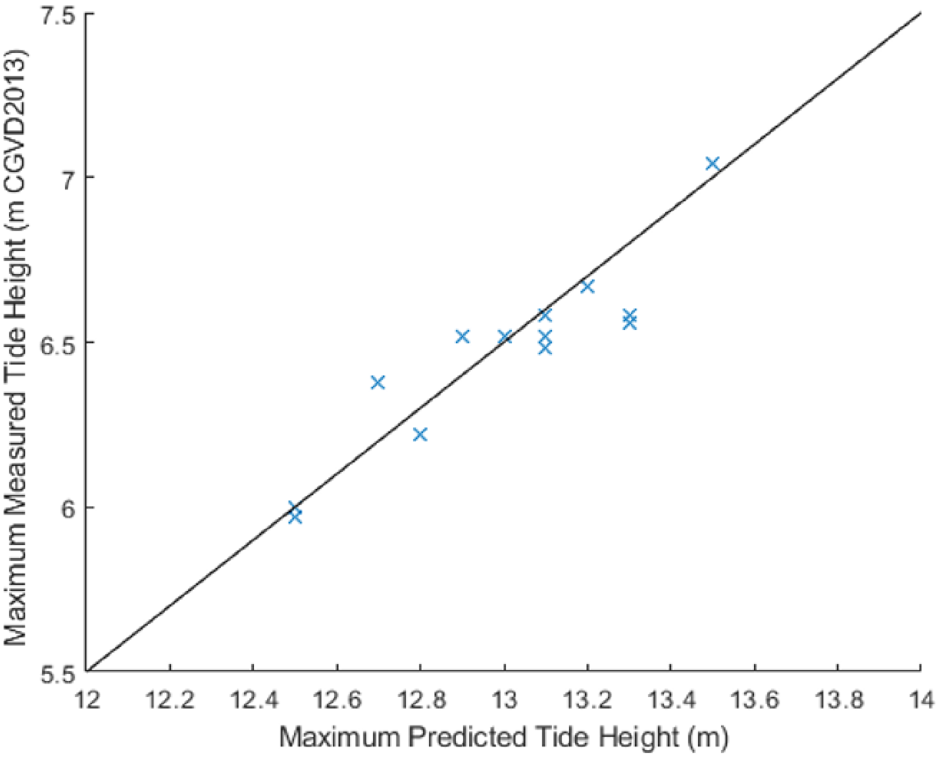

Figure 4.1. Maximum measured WSE versus PMTH with 1:1 ratio comparison.

4.1.3 Temporal Variations of Inlet Cross-Sectional Area, Velocity, and Discharge

The Converse Restoration site experienced visible erosion and measurable changes in inlet size during the study period as well as changes in velocity. In natural tidal basins, velocity will also increase with larger tides causing a larger head of water from the restriction of the creeks (Bayliss-Smith et al., 1979; Friess et al., 2014; O'Brien, 1969). Velocity will also change over time as the inlet cross-sectional area changes (Boon & Byrne, 1981; van de Kreeke, 2004). MR sites see large changes in cross sectional area of the inlet and channels each year after development (Friess et al., 2014; Lewis, 2022; van Proosdij et al., 2010), meaning this pattern could be even more prominent if the site was studied for a longer time period.

Although there were changes in velocity and cross-sectional area over the study period, there was little visual change to the discharge data when plotted. This indicates there was no visually noticeable changes to the tidal prism over the study period. On natural marshes, inlets and basins restricted by artificial fill or sedimentation, reducing the flow area, can have a reduced tidal prism (O'Brien, 1969), increasing as the inlet erodes and the area moves toward an equilibrium state. However, infilling in shallower areas can reduce the tidal prism of an area as well (Boon & Byrne, 1981). At the Converse site, within the study period, the hypothesized increase in capacity of the tidal prism from a wider inlet and channels, may be counteracted by infilling in the shallower areas of the site demonstrated in Figure 3.15, further discussed in section 4.4.2. This may not be the case for all sites, and this may change as Converse or other sites develop. There may also have been changes in Year 1 of restoration, before the study period.

4.1.4 Temporal Variations of Velocity in Relation to Graded Dykes

At the Converse MR site, water will fully flood the marsh before reaching the top of the inlet. The largest tide (November Tide 4), after fully flooding the site, continued rapidly increasing in velocity at the inlet before the shift to ebb tide. This was the only tide to flood over top of the areas of the dyke that had been graded during the initial dyke realignment. As a result, velocity slowed down as the water reached the graded dyke elevation, overtopping the graded dykes. This shows the breach(es) on a MR site continue to promote higher velocities after the water had flooded past bankfull levels, until the graded dykes are overtopped. The overtopping of these areas may also bring in, erode, or resuspend more sediment. The tides that reached this height made up approximately 9% of the tides in 2020 to 2021. This pattern may change as dykes continue to erode and more water can flood over these areas on the largest tides.

4.1.5 Temporal Variations of Suspended Sediment Concentrations

4.1.5.1 Temporal Variations of Velocity, Precipitation, and Suspended Sediment Concentration

Temporal variations of the changing inlet and channels, and therefore velocity, also affect the SSC, affecting the transport of sediment on multiple levels. Higher velocities result in higher SSC from resuspension (Hill et al., 2013), during tides with peak velocities around 1 to 1.2 $m \cdot s^{-1}$ (O'Laughlin & van Proosdij, 2013). Higher amplitude tides cause higher SSC values on natural marshes (Christiansen, 1998; Voulgaris & Meyers, 2004), because of these higher velocities (Chen et al., 2006; O'Laughlin & van Proosdij, 2013). SSC also increases from the erosion of channels experiencing high velocities. Xie et al. (2010) modelled inlet erosion, where the erosion intensity was affected by the current velocities in the order of 1 $m \cdot s^{-1}$. Also, velocities up to >2.5 $m \cdot s^{-1}$ were recorded during the initial breach of the MR site in Friess et al. (2014), equated to the initial erosion at the site.

At the Converse site, velocities reached up to 2 $m \cdot s^{-1}$, so SSC was likely increased by erosion and resuspension. This is supported by the SSC data directly inside the inlet being higher than the inlet SSC data. The highest velocities were recorded during August, having the narrowest inlet, and during the highest perigean-spring tide in November. As the channels eroded over the deployments, SSC levels should have reduced with the decreasing velocity, depending on the size of the tide. By this logic, the highest SSC should have been in August closer to when the site was breached and November when the highest tides occurred.

November had the highest SSC values, however, August, with tides comparable in size to July, had the lowest values. The expected SSC pattern was likely disrupted due to a large rain event before the July deployment, increasing SSC levels and causing a larger fraction of finer material in the suspended and deposited sediment. The effects of rain events can last two to three days following a large rainfall more than 1 to 2 mm·hr^{-1} (Dale et al., 2018), most evident when mudflats have been exposed to the rain, eroding the exposed mud surface (Murphy & Voulgaris, 2006). Law et al. (2021) also reported that in the Bay of Fundy a 64.9mm rainfall doubled the total suspended matter, increasing the fine-grained sediment and floc sizes, gradually decreasing 2.5 days later. With a total of 61mm over two days, rainfall effect can be seen in this dataset.

Two days before the July 2021 deployment, the maximum rate of precipitation was 7.9 mm·hr^{-1}. There were 10 consecutive hours of rainfall greater than 1 mm·hr^{-1}, with a total of eight hours above 2 mm·hr^{-1}. With ~12-hour cycle tides, bare sediment was likely exposed to this rainfall in the 10-hour period, adding to the effects of precipitation. Because of precipitation causing elevated SSC levels in July, it cannot be shown in this dataset that higher velocities from a smaller inlet and less developed MR site cause higher SSC.

4.1.5.2 Other Factors Affecting Suspended Sediment Concentrations

Studies have previously attributed higher SSC and deposition to certain seasons because of weather and biological factors (Carriére-Garwood, 2013; Garwood et al., 2015; Law et al., 2019; Poirier, 2014). In this thesis a statistical analysis was performed, comparing the deployment to a null model, where the month was not found to be a significant factor. Additionally, there were no visible seasonal precipitation or wind patterns through the study period at the Converse site. However, there may be potentially underlying seasonal or other factors that were not captured in this dataset.

Vegetation on natural marshes has been shown to attenuate wave and flow energy, affecting SSC (Leonard & Luther, 1995; Davidson-Arnott et al., 2002; van Proosdij et al., 2006;

van Proosdij et al., 2013). There were only two stations in the vegetated foreshore marsh, and one station with agricultural vegetation, however, two of these stations were at the highest station elevations. These stations received few deposition samples, so there were no noticeable patterns associated with vegetation in the data.

4.1.6 Temporal Variations of Sediment Flux and Effects of Inlet and Channel Evolution

It was previously stated that limited research has been done on the impacts of MR site evolution on tidal prisms and sediment flux. Previous work that produced a model for a natural tidal inlet had demonstrated that both narrow and wide inlets can import a lot of sediment, where narrow inlets cause higher SSC, and wider inlets allow more water carrying sediment into the site (Dissanayake et al., 2009). However, if a site infills enough with this eroded and imported sediment, the tidal prism is reduced (Friedrichs & Perry, 2001). In this dataset velocities decreased and the inlet and channels widened, but the discharge data had no noticeable change over the study period. With a relatively constant tidal prism and reduced velocities, this may have resulted in a reduction in SSC and therefore the sediment flux and deposition over the study period. However, this would have been overshadowed by the effects of precipitation. To test this hypothesis, the hydrologic and morphodynamic factors would need to be measured without the effects of precipitation. This could also change over the restoration period, so a longer study would be needed to see the full picture of the effects of MR site evolution on sediment flux. Changes may also occur as the graded dykes further erode at the site, allowing larger tides to enter the site more easily and bring in more sediment.

4.2 Spatial and Temporal Variations of Deposition on the Marsh Surface

4.2.1 Influence of Elevation, Distance from Channel, and Distance from Inlet

Elevation, Dc, and Di all played a role in the spatial distribution of sediment on the marsh surface. As elevation increased, deposition decreased, as shown in past studies (Chmura et al., 2001; Hill et al., 2013; Reed et al., 1999; Richard, 1978). Elevation may interact with other variables, such as the sum of depths, where inundation time and depth would be derived from their interaction (Temmerman et al., 2003). In the final models in this study, however, elevation was not found to predict deposition better when interacting with other variables, except for the PMTH model. The distance from source has also previously been found to have an impact on deposition (Butzeck et al., 2015; Davidson-Arnott et al., 2002; Leonard et al., 1995; Temmerman et al., 2003; van Proosdij, 2001). One form of this is the distance from creek, which was a very strong predictor of sediment deposition in this dataset, interacting with distance from inlet, cross-sectional area, velocity, and SSC. Di was the weakest predictor of all variables, however, its interaction with Dc shows its importance in predicting deposition at a point on a marsh surface.

Dc and Di both had polynomial relationships with deposition where the highest deposition was in the range of 150 to 350m from the inlet, and three to eight metres from the channel, respectively. This is similar to van Proosdij et al. (2006) where the highest deposition values were measured five to ten metres away from the tributaries or margin, very close to the Dc values in this study. This may indicate similarities with natural or vegetated sites for the Dc and Di variables, though more data on vegetated sites would be needed for further conclusions. Dc and Di interacted, where the highest deposition was at the optimal distance of both variables.

4.2.2 Relic Natural versus Agricultural Drainage Areas

A certain area of the Converse MR site appeared to have very different spatial deposition patterns, with little correlation with the previously described topographic variables. As previously mentioned, RS6 and MH17 were located in an area with little drainage, seen in field observations and in Figure 4.2. The evidence from the coarser material, low floc fraction, and low deposition, despite the same availability of sediment as other stations, shows that sheet flow may be resuspending the flocculated layer on the ebb tide. This causes the coarser, unflocculated sediment to remain. On natural marshes, ebb pulses have already been shown to resuspend sediment (Hill et al., 2013; O'Laughlin, 2012). RS6 had less deposition with higher tides, likely from less water draining over the station on the ebb tide and possibly lower velocities, resulting in less resuspension. This shows that larger tides can result in less deposition in these areas.

The Converse site has areas with relic natural channels from the historical salt marshes before the dyking of the area as well as channels from agricultural ditching (Lewis, 2022). RS6 and MH17 were located in an area where the few drainage channels (Figure 4.2) were relic natural channels, unlike areas in the rest of the site. The features of the other areas of the marsh possibly enhanced sediment trapping on a larger scale due to less efficient drainage, resulting in the infilling seen in section 3.2.2. The more natural drainage area possibly has more efficient drainage than the agricultural areas and may achieve higher speeds and sheet flow, resulting in resuspension, indicating this area may be at an equilibrium already, but may change with vegetation.

Figure 4.2. Station areas of RS6 in picture a) and MH17 in picture b), showing surrounding topography, taken on July 23rd, 2021 (TransCoastal Adaptations, 2021).

4.3 Connecting Inlet Conditions to Marsh Surface Conditions

4.3.1 Spatiotemporal Variations of Velocity

Velocity was shown to reduce further into the site, where velocity reduction around high tide was more prominent further from the inlet. There was also a slope in the water surface, highest at the inlet, shown in the reduction of the maximum WSE between the inlet and each channel hydrology station. This indicated the channels were restricting flow, causing the velocity reduction. The data shows similar velocity trends as natural marshes (Bayliss-Smith et al., 1979; Davidson-Arnott et al., 2002), though the patterns may change as the site further develops, changing spatiotemporal patterns of deposition.

4.3.2 Spatiotemporal Variations of Suspended Sediment Concentrations and Grain Sizes

SSC showed very similar patterns as velocity through the site, where both velocity and SSC decreased further from the inlet. The SSC at station V1, furthest from the inlet, was a little over half of the SSC at the R1 station, just inside the inlet. V1 also had much lower velocities than stations closer to the inlet. The RSB SSC was also lower than the inlet SSC, where only on larger tides, RSB SSC increased. This means tides need to be large enough to maintain velocities and therefore a higher SSC through the site. Less sediment will settle on the way to the point on the marsh surface, providing a higher availability of sediment for deposition, further from the inlet and channels. Reed et al. (1999) previously showed there is a reduction in SSC caused by settling on the marsh surface, and Leonard et al. (1995) showed this was from the decreasing velocities on the marsh surface.

The reduction of velocity and SSC further from the inlet is also reflected in the grain size data, where both suspended sediment and deposition grain size was finer, further from the inlet and channels as larger grains fell out of suspension as velocities reduced. Grain sizes have also been shown to progressively get finer with an increasing distance from creek on natural marshes (Christiansen et al., 2000; Poirier et al., 2017).

A clear example of the impact of just the distance from the inlet on the velocity and SSC, and therefore the amount of deposition, would be the RSB stations lining the water flow path from the inlet through the borrow pit. In Figure 4.3, the inlet and RSB stations on the path are shown on the map, where RS3 is the closest to the inlet, and RS1 is the furthest from the inlet. In the deposition versus initial SSC plots, both variables decrease further from the inlet. Grain size also becomes finer in both the RSB SSC and deposition samples (with the exception of the coarse RS2 RSB sample, where high velocities from November Tide 4 caused coarse samples across the marsh). This demonstrates settling between these stations as available sediment reduces and becomes finer, further from the inlet with the reduction of velocity.

This data showed that the distance from inlet and distance from channel variables act similarly and interact with each other. This supports the model results in this thesis and previous work by Temmerman et al. (2003) on their natural marsh model, where the two variables interact. At the MR site in Dale et al., (2017) there was constant deposition near the single inlet, but periodic accretion further inland of the site. Though this area has 450 ha (also with a single inlet), where the Converse site was 15 ha, it still shows a lack of deposition further from the inlet. On a MR site, these interactions may change over time as the site evolves and the hydrology of the site changes. In section 3.2.2, infilling of agricultural ditching resulted in changes of SSC patterns over the tides within the study period, which may indicate measurable changes to the spatiotemporal variations of sediment deposition over the course of the marsh restoration.

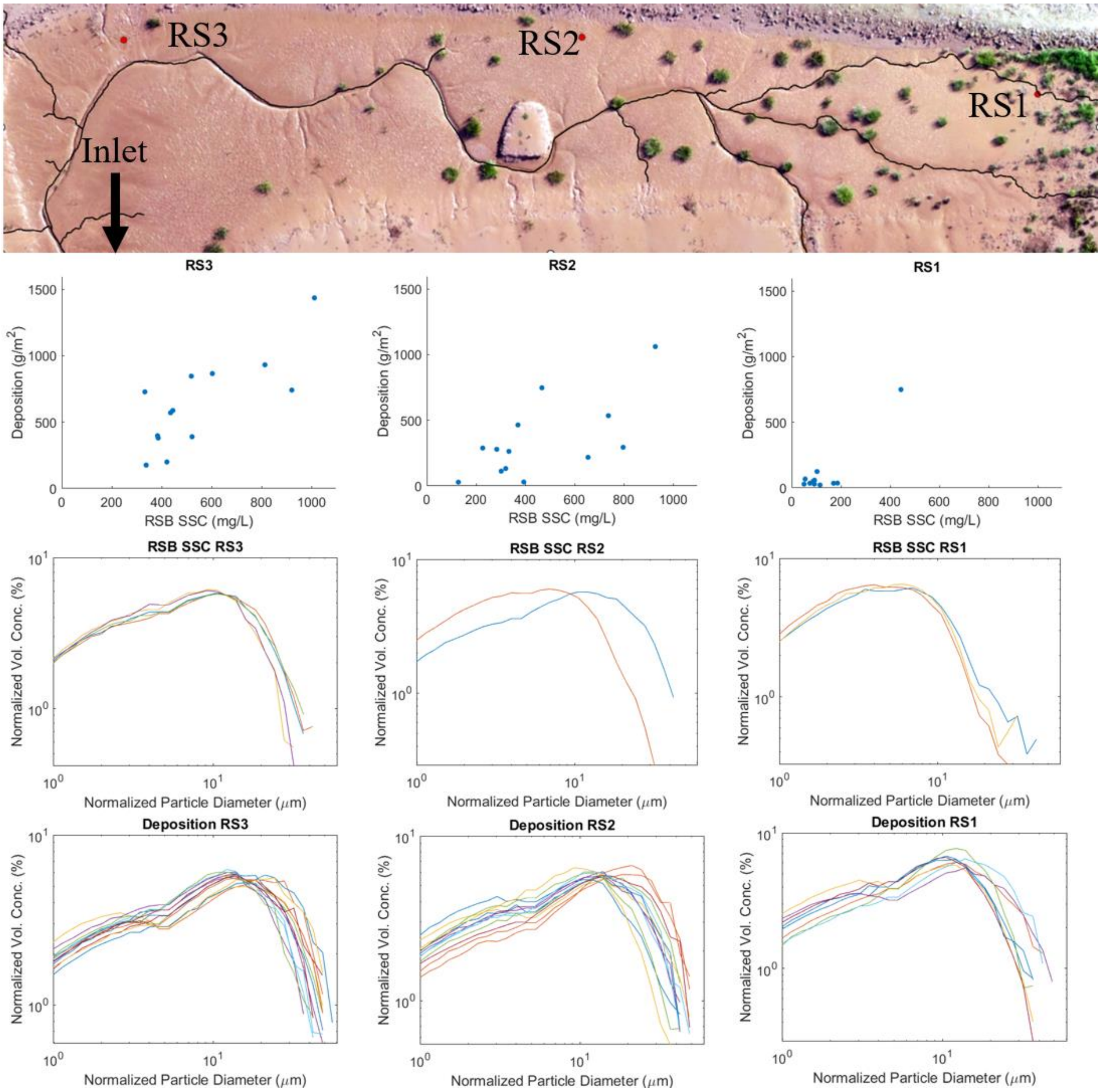

Figure 4.3. RS3 to RS1 borrow pit area, demonstrating coarser particle settling between stations as velocity slows further from the inlet.

4.4 Overall Effects of Hydrology, Topography, and Morphology on Deposition Patterns

4.4.1 Summary of Interactions Between Hydrodynamics and Topography and Spatiotemporal Patterns of Deposition

The interactions between the hydrodynamics and topography dominated the spatiotemporal variations of deposition at this MR site and allowed the prediction of deposition from topographic and inlet hydrologic variables. Larger tides created higher velocities, which increased the SSC through erosion and resuspension. These higher velocities carried sediment further into the site, resulting in a larger import of sediment and higher deposition overall, and higher deposition further from the inlet and channels. The largest tide also flooded over the graded dykes, reducing velocity at the inlet, but possibly introducing sediment in other parts of the site. This means the biggest changes to the sites will be around the perigean-spring tides.

This supports another study in the Bay of Fundy on a natural marsh, where the largest tides increased the sediment supply and redistributed the most sediment (O'Laughlin, 2012). Around 9% of all tides through the study period were greater than or around the size of the largest tide recorded, meaning those 9% of tides will have the largest impact on the site.

4.4.2 Summary of Managed Realignment Changes and their Effects on the Hydrodynamic-Topographic Interactions and Spatiotemporal Patterns of Deposition

The discharge data and tidal prism appeared to be unchanged through the study period, despite the widening inlet. As the inlet widened, velocity decreased. The slope of the water from the inlet to the velocity stations in the site was indicative that the inlet was restricting the incoming potential water. This did not appear to have large changes during the study period, further indicating no change to the rate of water entering the site. The inlet may need to widen further until the velocity reduces to velocity levels outside the breach, where any further widening of the inlet would not cause further velocity reductions, allowing higher discharge rates.

The infilling documented in Lewis (2022) and shown in Figure 3.15 affected ebb SSC patterns, seen at V3, showing its effects on the spatiotemporal patterns of SSC and possibly deposition. Infilling is also known to reduce tidal prisms (Friedrichs & Perry, 2001). The infilling during the study period was either not enough to see an effect on the tidal prism, or the volume of sediment lost at the inlet was transported further into the site. This would mean the total holding capacity for water in the site would remain unchanged. The discharge is controlled by the inlet restriction rather than the surface area of the marsh available to be flooded, so any potential impacts on the discharge data would be masked by the effects of the inlet restriction.

Lewis (2022) showed with the surface volume changes in the site that the erosion of the inlet and channels may help feed the site, though the extent of the contributions from the inlet area could not be determined. Dale (2018) showed sediment was imported into the large site in their study, but greater levels of SSC inside the site showed that sediment was being redistributed within the site. This supports that erosion of the inlet and channels is contributing to infilling on the site. Infilling may be occurring in the less efficient flow paths, particularly agricultural ditching, where more efficient flow paths, such as the relic natural channels around MH17 and RS6, resuspension occurred, which may possibly indicate these areas are closer to an equilibrium. Old dykes will also further erode in the future, possibly changing the hydrologic and sedimentation patterns of the highest tides of the year.

4.5 Application and Future Work of Models

4.5.1 Validating and Applying Deposition Models

To validate the Hydro/Topo and PMTH model formulas, they must be tested against other deposition or equivalent variables from different datasets taken at the site. In Brunetta (2022), a co-occurring study at Converse, deposition data was collected near the stations in this dataset, as well as a few other stations, on the same tides during the July 2021 deployment. This deposition data would have the same hydrodynamic data and different topography points, allowing validation of the model formulas.

The model formulas would then be applied to each point on a raster of the topographic variables, using the hydrodynamic data for a single tide to get a deposition value. In Lewis (2022), elevation and distance from channel rasters were made, however distance from inlet rasters would need to be generated. These rasters can be used, along with the hydrodynamic data from this study to create a deposition map. Once deposition maps are made, they can be compared to the elevation change maps in Lewis (2022) for validation, which may help analyze the elevation change maps themselves, seeing what changes can be attributed to accretion.

4.5.2 Long-term Models: Using Predicted Maximum Tide Height Models

Since the Hydro/Topo models are not feasible in the long term due to the resources needed, the PMTH model can use the predicted tides discussed in 4.1.2 and the topographic data. The resulting equation can be used in the same way to make a deposition map. Only tides able to inundate the surface would be used, where in 2020 and 2021, approximately 15% of tides reached over bankfull level, based on the PMTH of the tides captured in the deployments.

Additionally, if water level measurements are taken at the site, site-specific predictions can be made. The Converse site had a water level recorder first installed in 2019, but there were issues with the instrument (Bowron et al., 2020).

4.5.3 Long-term Models: Predicting Accretion

The long-term goal of the models in this study is to predict accretion rather than just deposition, as cumulative deposition does not equate to the accretion. To convert deposition to accretion, bulk density samples were taken in July 2021 at each station for future data processing for this site. Accretion conversions would need to be calculated for each station by using Equation 4-1 from Butzeck et al. (2015) where AR is accretion rate per year, SDR is sediment deposition rate per year, and BD is the bulk density, though in this case AR and SDR would be per tide. The final models would need to be re-run to accommodate this change, to acquire new coefficients needed to predict accretion at a given point on the marsh. With these new coefficients, the application of the equation from this model would be applied to the topographic raster to generate an accretion map for a single tide. These values would then be used for a cumulative accretion map, to have a total predicted accretion map, and validated with the marker horizon accretion data.

Equation 4-1. Accretion calculation using deposition and bulk density (Butzeck et al., 2015).

$$AR\ (cm\ year^{-1}) = SDR(g\ cm^{-2} year^{-1})/BD\ (g\ cm^{-3})$$

Because accretion is a longer-term variable measured on a yearly basis, there is more likelihood for error in the models and cumulative accretion values, due to additional factors such as ice rafting sediment, causing patches of high deposition and scouring the marsh surface (Argow et al., 2011; FitzGerald et al., 2020; Gordon & Desplanque, 1983; Ollerhead et al., 1999) or storms causing high accretion rates, sometimes in conjunction with ice rafts (FitzGerald et al., 2020).

4.6 Summary of Limitations and Future Recommendations

4.6.1 Managed Realignment Studies

The rainfall in July showed the effects of precipitation on SSC in MR sites, however, to confirm the hypothesis that SSC and sediment flux and therefore deposition decrease as the MR site evolves, another deployment at the Converse site like the ones described in this study would likely clarify this. Additionally, continuation of the monitoring of the cross-sectional areas of channels and site topography paired with channel hydrologic data may benefit future studies. This may confirm that less water can move further into the site as the marsh surface infills with the eroded material from the channels and inlet and the ambient SSC. This would mean the water volume capacity is reduced further into the site but increases in the eroding channels, maintaining a similar water volume capacity for the site. Another deployment would also show if this would change deposition patterns on the surface of the site over time. It may also be beneficial to study the few, large tides of the year in future work, as the largest tide had the largest impacts on the site. The next steps for observing hydrologic and deposition patterns would be to include vegetated or partially vegetated sites, and other MR sites in the Bay of Fundy, and determining the impact of eroding dykes.

4.6.2 Statistical Models

The creation of the statistical models themselves have limitations, where statistical modelling and assessing the models is evolving. More observations would allow better prediction, however the Hydro/Topo formulas already account for ~80% of the variation in deposition, and the PMTH models account for 64% for just the fixed effects. The models did not reflect the RS6 and MH17 area since these stations were not included in the models. This type of area clearly has different deposition patterns and would need a separate analysis with more data points.

Since MR sites share some of the same qualities with the Converse site, the models and findings of this study may be useful at other MR sites in macrotidal environments. After applying and validating the models, the models could be re-run and tested to see how applicable the formula is to other MR sites in varying stages of restoration in the Bay of Fundy with existing or future datasets. These other sites may have vegetation or multiple inlets, possibly affecting the applicability of the models. The same variables and combinations of those variables may still apply, however other parameters pertaining to additional features like multiple inlets may need to be incorporated.

CHAPTER 5 CONCLUSIONS

This thesis demonstrates the need for sediment dynamics research on MR sites, particularly in the Bay of Fundy, to contribute to more informed restoration trajectory and accretion models. MR site inlets and channels can erode rapidly causing relatively fast-paced changes to the hydrodynamics on the site. The data collected in this study allowed the observation of interactions between the hydrology of the tides and topography of the MR site, resulting in the spatiotemporal deposition patterns. These patterns changed during the restoration process, and showed how MR sites stabilize.

Hydrodynamic conditions at the inlet varied temporally over each tide and between deployments during one year of site evolution. Overall, velocity decreased over the deployments as the inlet and channels widened and evolved, with little change to the discharge or tidal prism. The larger perigean-spring tides had higher velocity and SSC values, thus having a higher influx of sediment through the inlet. Evidence also suggested a noticeable increase of SSC due to inlet scouring, corresponding with higher velocities from a smaller inlet and higher tides. Reductions in SSC and sediment flux as the site developed and velocities decreased could not be confirmed due to precipitation before the last deployment raising ambient SSC.

Deposition varied temporally between tides and deployments. Spatial variations of deposition depended on topographic variables including the elevation, the distance from channel, and distance from inlet. An area of the marsh with little drainage did not follow these patterns, where there was resuspension that increased with larger tides, caused by more sheet flow over the area. This area had relic natural channels, where much of the rest of the site had less efficient flow paths such as agricultural ditching that had infilling over the study period.

The hydrologic variables worked in conjunction with the topographic variables. It is this interaction with the hydrology and topography that dominated the spatiotemporal variations of deposition at this MR site and allowed the prediction of deposition from topographic and inlet hydrologic variables. The large perigean-spring tide recorded resulted in the largest import of sediment and redistribution within the site. As the site evolved, the lack of change in the tidal prism with eroded channels, lower velocities, and infilling indicated sediment volume lost at the inlet may have shifted further into the site, infilling less efficient flow paths, most helped by the perigean-spring tides.

These observations legitimized and guided a statistical analysis aimed at predicting deposition at the Converse site, for the purpose of assisting future accretion models. Models were produced that could predict deposition at a point on a marsh using hydrologic and topographic variables explaining up to ~80% of the variation of deposition for just the fixed effects, where the predicted tide models accounted for ~64%.

These findings and models can be compared and applied to vegetated or partially vegetated and more developed MR sites to further determine how they can contribute to restoration trajectory and accretion models. This will help to determine timelines for accretion and elevation changes due to sedimentation as the marshes grow and shift back into their original protective coastal landscape.

REFERENCES

Akyol, R. (2020). *Mapping and quantifying early tidal wetland evolution using remotely piloted aircraft system imagery and object-based image analysis*. [Master's thesis, Saint Mary's University]. Saint Mary's University Institutional Repository. https://library2.smu.ca/handle/01/29339

Amos, C. L., & Mosher, D. C. (1985). Erosion and deposition of fine-grained sediments from the Bay of Fundy. *Sedimentology*, *32*(6), 815–832. https://doi.org/10.1111/j.1365-3091.1985.tb00735.x

Amos, C. L., Tee, K. T., & Zaitlin, B. A. (1991). The post-glacial evolution of Chignecto Bay, Bay of Fundy, and its modern environment of deposition. *Clastic Tidal Sedimentology*, 59–89.

Anderson, M. E., & Smith, J. M. (2014). Wave attenuation by flexible, idealized salt marsh vegetation. *Coastal Engineering*, *83*, 82–92. https://doi.org/10.1016/j.coastaleng.2013.10.004

Argow, B. A., Hughes, Z. J., & FitzGerald, D. M. (2011). Ice raft formation, sediment load, and theoretical potential for ice-rafted sediment influx on northern coastal wetlands. *Continental Shelf Research*, *31*(12), 1294–1305. https://doi.org/10.1016/j.csr.2011.05.004

Augustin, L. N., Irish, J. L., & Lynett, P. (2009). Laboratory and numerical studies of wave damping by emergent and near-emergent wetland vegetation. *Coastal Engineering*, *56*(3), 332–340. https://doi.org/10.1016/j.coastaleng.2008.09.004

Bates, D., Mächler, M., Bolker, B. M., & Walker, S. C. (2015). Fitting linear mixed-effects models using lme4. *Journal of Statistical Software*, *67*(1), 1–48. https://doi.org/10.18637/jss.v067.i01

Bayliss-Smith, T. P., Healey, R., Lailey, R., Spencer, T., & Stoddart, D. R. (1979). Tidal flows in salt marsh creeks. *Estuarine and Coastal Marine Science*, *9*(3), 235–255. https://doi.org/10.1016/0302-3524(79)90038-0

Best, S. N., Van der Wegen, M., Dijkstra, J., Willemsen, P. W. J. M., Borsje, B. W., & Roelvink, D. J. A. (2018). Do salt marshes survive sea level rise? Modelling wave action, morphodynamics and vegetation dynamics. *Environmental Modelling and Software*, *109*, 152–166. https://doi.org/10.1016/j.envsoft.2018.08.004

Blott, S. J., & Pye, K. (2001). GRADISTAT: A grain size distribution and statistics package for the analysis of unconsolidated sediments. *Earth Surface Processes and Landforms*, *26*(11), 1237–1248. https://doi.org/10.1002/esp.261

Bolker, B. M., Brooks, M. E., Clark, C. J., Geange, S. W., Poulsen, J. R., Stevens, M. H. H., & White, J. S. S. (2009). Generalized linear mixed models: a practical guide for ecology and evolution. *Trends in Ecology and Evolution*, *24*(3), 127–135. https://doi.org/10.1016/j.tree.2008.10.008

Boon, J. D., & Byrne, R. J. (1981). On basin hyposmetry and the morphodynamic response of coastal inlet systems. *Marine Geology*, *40*(1–2), 27–48. https://doi.org/10.1016/0025-3227(81)90041-4

Bowron, T. M., Graham, J., Ellis, K., Kickbush, J., McFadden, C., Poirier, E., Lundholm, J., & Proosdij, D. (2020). *Post-restoration monitoring (Year 1) of the Converse Salt Marsh Restoration (NS044) – 2019-20 summary report.* (Publication No. 59). Prepared for the Department of Fisheries and Oceans and Nova Scotia Department of Agriculture.

Bowron, T., Neatt, N., van Proosdij, D., Lundholm, J., & Graham, J. (2011). Macro-tidal salt marsh ecosystem response to culvert expansion. *Restoration Ecology*, *19*(3), 307–322. https://doi.org/10.1111/j.1526-100X.2009.00602.x

Brunetta R. (2022). Evolution of restoration projects of coastal wetlands: from tidal flat to salt marsh. [Ph.D. thesis, Department of Physics and Earth Sciences, Coastal Study Unit Ferrara, University of Ferrara, Italy].

Butzeck, C., Eschenbach, A., Gröngröft, A., Hansen, K., Nolte, S., & Jensen, K. (2015). Sediment deposition and accretion rates in tidal marshes are highly variable along estuarine salinity and flooding gradients. *Estuaries and Coasts*, *38*, 434–450. https://doi.org/10.1007/s12237-014-9848-8

Byers, S. E., & Chmura, G. L. (2007). Salt marsh vegetation recovery on the Bay of Fundy. *Estuaries and Coasts*, *30*(5), 869–877. https://doi.org/10.1007/BF02841340

Cahoon, D. R., Lynch, J. C., Perez, B. C., Segura, B., Holland, R. D., Stelly, C., Stephenson, G., & Hensel, P. (2002). High precision measurements of wetland sediment elevation: II. The rod surface elevation table. *Journal of Sedimentary Research*, *72*(5), 734–739. https://doi.org/10.1306/020702720734

Campbell Scientific INC. (2014). *OBS-3+ and OBS300 Suspended Solids and Turbidity Monitors*. https://s.campbellsci.com/documents/au/manuals/obs-3+.pdf.

Carriére-Garwood, J. (2013). *Seasonal variation and biological effects on mudflat erodibility in the minas basin, bay of fundy*. [Master's thesis, Dalhousie University]. DalSpace Institutional Repository. http://hdl.handle.net/10222/42733

Cazenave, A., & Nerem, R. S. (2004). Present-day sea level change: Observations and causes. *Reviews of Geophysics*, *42*(3), RG3001. https://doi.org/10.1029/2003RG000139

Chen, S. L., Zhang, G. A., Yang, S. L., & Shi, J. Z. (2006). Temporal variations of fine suspended sediment concentration in the Changjiang River estuary and adjacent coastal waters, China. *Journal of Hydrology*, *331*(1–2), 137–145. https://doi.org/10.1016/j.jhydrol.2006.05.013

Chmura, G. L., Coffey, A., & Crago, R. (2001). Variation in surface sediment deposition on salt marshes in the Bay of Fundy. *Journal of Coastal Research*, *17*(1), 221–227.

Christiansen, T. (1998). *Sediment Deposition on a Tidal Salt Marsh*. [Ph.D. thesis, University of Virginia]. https://www.vcrlter.virginia.edu/thesis/Christiansen98.pdf

Christiansen, T., Wiberg, P. L., & Milligan, T. G. (2000). Flow and sediment transport on a tidal salt marsh surface. *Estuarine, Coastal and Shelf Science*, *50*(3), 315–331. https://doi.org/10.1006/ecss.2000.0548

Curran, K. J., Hill, P. S., Schell, T. M., Milligan, T. G., & Piper, D. J. W. (2004). Inferring the mass fraction of floc-deposited mud: Application to fine-grained turbidites. *Sedimentology*, *51*(5), 927–944. https://doi.org/10.1111/j.1365-3091.2004.00647.x

D’Alpaos, A., Mudd, S. M., & Carniello, L. (2011). Dynamic response of marshes to perturbations in suspended sediment concentrations and rates of relative sea level rise. *Journal of Geophysical Research: Earth Surface*, *116*(4), 1–13. https://doi.org/10.1029/2011JF002093

Dale, J. (2018). The evolution of the sediment regime in a large open coast managed realignment site: a case study of the Medmerry Managed Realignment Site, UK. [Ph.D. thesis, School of Environment and Technology, University of Brighton]. https://cris.brighton.ac.uk/ws/portalfiles/portal/4784884/JDale_Thesis_Final.pdf

Dale, J., Burgess, H. M., & Cundy, A. B. (2017). Sedimentation rhythms and hydrodynamics in two engineered environments in an open coast managed realignment site. *Marine Geology*, *383*, 120–131. https://doi.org/10.1016/j.margeo.2016.12.001

Dale, J., Burgess, H. M., Nash, D. J., & Cundy, A. B. (2018). Hydrodynamics and sedimentary processes in the main drainage channel of a large open coast managed realignment site. *Estuarine, Coastal and Shelf Science*, *215*(October), 100–111. https://doi.org/10.1016/j.ecss.2018.10.007

Davidson-Arnott, R. G. D., Proosdij, D. van, Ollerhead, J., & Schostak, L. (2002). Hydrodynamics and sedimentation in salt marshes: examples from a macrotidal marsh, Bay of Fundy. *Geomorphology*, *48*, 209–231.

Desplanque, C., & Mossman, D. J. (2004). Tides and their seminal impact on the geology, geography, history, and socio-economics of the Bay of Fundy, eastern Canada. *Atlantic Geology*, *40*(1). https://doi.org/10.4138/729

Dissanayake, D. M. P. K., Roelvink, J. A., & van der Wegen, M. (2009). Modelled channel patterns in a schematized tidal inlet. *Coastal Engineering*, *56*(11–12), 1069–1083. https://doi.org/10.1016/j.coastaleng.2009.08.008

Doody, J. P. (2004). 'Coastal squeeze'— an historical perspective. *Journal of Coastal Conservation*, *10*(1), 129–138. https://doi.org/10.1007/bf02818949

Ellis, K., Graham, J. M., Bowron, T. M., van Proosdij, D., & Ollivier, B. (2018). *Pre-construction monitoring (baseline) of the Converse Marsh (NS044) Restoration Project – Summary report*.

FitzGerald, D. M., Fenster, M. S., Argow, B. A., & Buynevich, I. V. (2008). Coastal impacts due to sea-level rise. *Annual Review of Earth and Planetary Sciences*, *36*, 601–647. https://doi.org/10.1146/annurev.earth.35.031306.140139

FitzGerald, D. M., Hughes, Z. J., Georgiou, I. Y., Black, S., & Novak, A. (2020). Enhanced, climate-driven sedimentation on salt marshes. *Geophysical Research Letters*, *47*(10). https://doi.org/10.1029/2019GL086737

French, P. W. (1999). Managed retreat: A natural analogue from the Medway estuary, UK. *Ocean and Coastal Management*, *42*(1), 49–62. https://doi.org/10.1016/S0964-5691(98)00079-9

French, P. W. (2006). Managed realignment – The developing story of a comparatively new approach to soft engineering. *Estuarine, Coastal and Shelf Science*, *67*(3), 409–423. https://doi.org/10.1016/J.ECSS.2005.11.035

Friedrichs, C. T., & Perry, J. E. (2001). Tidal Salt Marsh Morphodynamics: A Synthesis. *Journal of Coastal Research*, *27*, 7–37. http://www.jstor.org/stable/25736162%5Cnhttp://www.jstor.org/page/

Friess, D. A., Möller, I., Spencer, T., Smith, G. M., Thomson, A. G., & Hill, R. A. (2014). Coastal saltmarsh managed realignment drives rapid breach inlet and external creek evolution, Freiston Shore (UK). *Geomorphology*, *208*, 22–33. https://doi.org/10.1016/J.GEOMORPH.2013.11.010

Gardiner, S., Hanson, S., Nicholls, R., Zhang, Z., Jude, S., Jones, A., Richards, J., Williams, A., Spencer, T., Cope, S., Gorczynska, M., Bradbury, A., McInnes, R., Ingleby, A., & Dalton, H. (2007). The habitats directive, coastal habitats and climate change - Case studies from the south coast of the UK. *Coastal Management - Proceedings of the Two-Day International Conference Organised by the Institution of Civil Engineers, ICE*, 193–202.

Garwood, J. C., Hill, P. S., MacIntyre, H. L., & Law, B. A. (2015). Grain sizes retained by diatom biofilms during erosion on tidal flats linked to bed sediment texture. *Continental Shelf Research*, *104*, 37–44. https://doi.org/10.1016/j.csr.2015.05.004

Gedan, K. B., Kirwan, M. L., Wolanski, E., Barbier, E. B., & Silliman, B. R. (2011). The present and future role of coastal wetland vegetation in protecting shorelines: Answering recent challenges to the paradigm. *Climatic Change*, *106*(1), 7–29. https://doi.org/10.1007/s10584-010-0003-7

Gordon, D. C. Jr., & Desplanque, C. (1983). Dynamics and environmental effects of ice in the Cumberland Basin of the Bay of Fundy. *Canadian Journal of Fisheries and Aquatic Science 40*(9), 1331-1342. https://doi.org/10.1139/f83-156

Government of New Brunswick, Government of Nova Scotia, Wood Company, & Stantec. (2022). *Chignecto Isthmus climate change adaptation comprehensive engineering and feasibility study*. https://www2.gnb.ca/content/dam/gnb/Departments/trans/Chignecto/chignecto-isthmus-project-report-e.pdf

Graczyk, D. J., Robertson, D. M., Rose, W. J., & Steur, J. J. (2000). Comparison of water-quality samples collected by siphon samplers and automatic samplers in Wisconsin. *USGS Fact Sheet 067-00, July*, 0–3. https://pubs.er.usgs.gov/publication/fs06700

Green, M. O., & Coco, G. (2014). Review of wave-driven sediment resuspension and transport in estuaries. *Reviews of Geophysics*, *52*(1), 77–117. https://doi.org/10.1002/2013RG000437

Greenberg, D. A., Blanchard, W., Smith, B., & Barrow, E. (2012). Climate change, mean sea level and high tides in the bay of fundy. *Atmosphere - Ocean*, *50*(3), 261–276. https://doi.org/10.1080/07055900.2012.668670

Guo, C., He, Q., Guo, L., & Winterwerp, J. C. (2017). A study of in-situ sediment flocculation in the turbidity maxima of the Yangtze Estuary. *Estuarine, Coastal and Shelf Science*, *191*, 1–9. https://doi.org/10.1016/j.ecss.2017.04.001

Hill, P. S., Newgard, J. P., Law, B. A., & Milligan, T. G. (2013). Flocculation on a muddy intertidal flat in Willapa Bay, Washington, Part II: Observations of suspended particle size in a secondary channel and adjacent flat. *Continental Shelf Research*, *60*, 1–12. https://doi.org/10.1016/j.csr.2012.06.006

Hinkel, J., Lincke, D., Vafeidis, A. T., Perrette, M., Nicholls, R. J., Tol, R. S. J., Marzeion, B., Fettweis, X., Ionescu, C., & Levermann, A. (2014). Coastal flood damage and adaptation costs under 21st century sea-level rise. *Proceedings of the National Academy of Sciences of the United States of America*, *111*(9), 3292–3297. https://doi.org/10.1073/pnas.1222469111

James, T. S., Henton, J. A., Leonard, L. J., Darlington, A., Forbes, D. L., & Craymer, M. (2014). *Relative Sea-level Projections in Canada and the Adjacent Mainland United States*. Geological Survey of Canada, Open File 7737. https://doi.org/10.4095/295574

James, T. S., Robin, C., Henton, J. A., & Craymer, M. (2021). *Relative sea-level projections for Canada based on the IPCC Fifth Assessment Report and the NAD83v70VG national crustal* *velocity model.* Geological Survey of Canada, Open File 8764. https://doi.org/10.4095/327878

Keulegan, G. H. (1967). *Tidal flow in entrances; water-level fluctuations of basins in communication with seas*. (Technical Bulletin No. 14). Committee on Tidal Hydraulics, U.S. Army Corps of Engineers.

Kirwan, M., & Temmerman, S. (2009). Coastal marsh response to historical and future sea-level acceleration. *Quaternary Science Reviews*, *28*(17–18), 1801–1808. https://doi.org/10.1016/j.quascirev.2009.02.022

Kranck, K. (1980). Experiments on the significance of flocculation in the settling of fine-grained sediment in still water. *Canadian Journal of Earth Sciences*, *17*(11), 1517–1526. https://doi.org/10.1139/e80-159+

Kranck, K., & Milligan, T. G. (1992). Characteristics of suspended particles at an 11-hour anchor station in San Francisco Bay, California. *Journal of Geophysical Research*, *97*(C7), 373–382. https://doi.org/10.1029/92jc00950

Law, B. A., Hill, P. S., Milligan, T. G., & Zions, V. (2019). Temporal and spatial changes in grain size on a macro-tidal channel-flat complex: results from Kingsport, Nova Scotia, Bay of Fundy. *Ocean Dynamics*, *69*(2), 239–252. https://doi.org/10.1007/s10236-018-1237-6

Law, B. A., Milligan, T. G., Hill, P. S., & Bugden, G. L. (2021). The effect of concentration on particle settling in the Minas Basin, Nova Scotia. *Continental Shelf Research*, *223*(May), 104448. https://doi.org/10.1016/j.csr.2021.104448

Le Bars, D. (2018). Uncertainty in sea level rise projections due to the dependence between contributors. *Earth's Future*, *6*(9), 1275–1291. https://doi.org/10.1029/2018EF000849

Leonard, L. A. (1997). Controls of sediment transport and deposition in an incised mainland marsh basin, southeastern North Carolina. *Wetlands*, *17*(2), 263–274. https://doi.org/10.1007/BF03161414

Leonard, L. A., Hine, A. C., & Luther, M. E. (1995). Surficial sediment transport and deposition processes in a Juncus roemerianus Marsh, west-central Florida. *Journal of Coastal Research*, *11*(2), 322–336.

Leonard, L. A., & Luther, M. E. (1995). Flow hydrodynamics in tidal marsh canopies. *Limnology and Oceanography*, *40*(8), 1474–1484. https://doi.org/10.4319/lo.1995.40.8.1474

Leonardi, N., Carnacina, I., Donatelli, C., Ganju, N. K., Plater, A. J., Schuerch, M., & Temmerman, S. (2018). Dynamic interactions between coastal storms and salt marshes: A review. *Geomorphology*, *301*, 92–107. https://doi.org/10.1016/j.geomorph.2017.11.001

Lewis, S. (2022). *Characterizing the evolution of a restoring salt marsh landscape with low altitude aerial imagery and photogrammetric techniques*. [Master's thesis, Saint Mary's University]. Saint Mary's University Institutional Repository. https://library2.smu.ca/handle/01/30893

Lund-Hansen, L. C., Petersson, M., & Nurjaya, W. (1999). Vertical sediment fluxes and wave-induced sediment resuspension in a shallow-water coastal lagoon. *Estuaries, 22*(1), 39–46. https://doi.org/10.2307/1352925

Lynch, J. C., Hensel, P., & Cahoon, D. R. (2015). *The surface elevation table and marker horizon technique: A protocol for monitoring wetland elevation dynamics.* (1078) Natural Resource Report NPS/NCBN/NRR.

MacDonald, G. K., Noel, P. E., van Proosdij, D., & Chmura, G. L. (2010). The legacy of agricultural reclamation on channel and pool networks of Bay of Fundy salt marshes. *Estuaries and Coasts, 33*(1), 151–160. https://doi.org/10.1007/s12237-009-9222-4

Milligan, T., & Kranck, K. (1991). Electroresistance particle size analyzers. In J. Syvitski (Ed.), *Principles, Methods and Application of Particle Size Analysis*, (pp. 109-118). Cambridge: Cambridge University Press. http://doi.org/10.1017/CBO9780511626142.011

Milligan, T. G., & Loring, D. H. (1997). The effect of flocculation on the size distributions of bottom sediment in coastal inlets: Implications for contaminant transport. *Water, Air and Soil Pollution, 99*, 33–42.

Mitrovica, J. X., Tamisiea, M. E., Davis, J. L., & Milne, G. A. (2001). Recent mass balance of polar ice sheets inferred from patterns of global sea-level change. *Nature, 409,* 1026–1029.

Murphy, S., & Voulgaris, G. (2006). Identifying the role of tides, rainfall and seasonality in marsh sedimentation using long-term suspended sediment concentration data. *Marine Geology, 227*(1–2), 31–50. https://doi.org/10.1016/j.margeo.2005.10.006

Narayan, S., Beck, M. W., Reguero, B. G., Losada, I. J., Van Wesenbeeck, B., & Pontee, N. (2016). The Effectiveness, Costs and Coastal Protection Benefits of Natural and Nature-Based Defences. *PLoS ONE, 11*(5), 154735. https://doi.org/10.1371/journal.pone.0154735

Newgard, John (2012). *MergeProcessor*. [MATLAB script, files, and functions]. https://github.com/JessCG/MS3

Nordin, C. F. Jr., & Dempster, G. R. Jr., (1963). *Vertical distribution of velocity and suspended sediment middle Rio Grande New Mexico*. Geological Survey, Professional Paper 462-B. https://doi.org/10.3133/pp462B

Norris, G. S., Virgin, S. D. S., Schneider, D. W., McCoy, E. M., Wilson, J. M., Morrill, K. L., Hayter, L., Hicks, M. E., & Barbeau, M. A. (2022). Patch-level processes of vegetation underlying site-level restoration patterns in a megatidal salt marsh. *Frontiers in Ecology and Evolution, 10*. https://doi.org/10.3389/fevo.2022.1000075

Nortek (2018). *Storm*. [Post-processing software]. https://www.nortekgroup.com/softwarelicense/storm

Nyman, J. A., Walters, R. J., Delaune, R. D., & Patrick, W. H. (2006). Marsh vertical accretion via vegetative growth. *Estuarine, Coastal and Shelf Science, 69*(3–4), 370–380. https://doi.org/10.1016/j.ecss.2006.05.041

O'Brien, M. P. (1967). Equilibrium Flow Areas of Tidal Inlets on Sandy Coasts. *Journal of the Waterways and Harbor Division*, *95*(1), 43–52. https://doi.org/10.1061/9780872620087.039

O'Laughlin, C. (2012). *The effect of changing tidal energy over the spring-neap cycle on net sediment deposition in a hypertidal Bay of Fundy salt marsh creek*. [Master's thesis, Saint Mary's University]. Saint Mary's University Institutional Repository. https://library2.smu.ca/handle/01/25205

O'Laughlin, C., & van Proosdij, D. (2013). Influence of varying tidal prism on hydrodynamics and sedimentary processes in a hypertidal salt marsh creek. *Earth Surface Processes and Landforms*, *38*(5), 534–546. https://doi.org/10.1002/esp.3340

O'Laughlin, C., van Proosdij, D., & Milligan, T. G. (2014). Flocculation and sediment deposition in a hypertidal creek. *Continental Shelf Research*, *82*, 72–84. https://doi.org/10.1016/j.csr.2014.02.012

Ollerhead, J., van Proosdij, D., & Davidson-Arnott, R.G.D. (1999). *Ice as a mechanism for contributing sediments to the surface of a macro-tidal saltmarsh, Bay of Fundy*. [Conference Proceedings]. 1999 Canadian Coastal Conference, Canadian Coastal Science and Engineering Association. 345-358.

Oppenheimer, M., Glavovic, B. C., Hinkel, J., van de Wal, R., Magnan, A. K., Abd-Elgawad, A., Cai, R., Cifuentes-Jara, M., DeConto, R. M., Ghosh, T., Hay, J., Isla, F., Marzeion, B., Meyssignac, B., & Sebesvari, Z. (2019). Sea Level Rise and Implications for Low-Lying Islands, Coasts and Communities. H.-O. Pörtner, D. C. Roberts, V. Masson-Delmotte, P. Zhai, M. Tignor, E. Poloczanska, K. Mintenbeck, A. Alegría, M. Nicolai, A. Okem, J. Petzold, B. Rama, & N. M. Weyer (Eds.), *IPCC Special Report on the Ocean and Cryosphere in a Changing Climate*. 321-445. https://doi.org/10.1017/9781009157964.012

Pereira, Daniel (2023). *Wind Rose*. MATLAB Central File Exchange. [MATLAB script and functions]. https://www.mathworks.com/matlabcentral/fileexchange/47248-wind-rose

Poirier, E. (2014). *Seasonal influences on the ecomorphodynamics of a hypertidal salt marsh and tidal creek system*. [Master's thesis, Saint Mary's University]. Saint Mary's University Institutional Repository. https://library2.smu.ca/handle/01/26271

Poirier, E., van Proosdij, D., & Milligan, T. G. (2017). The effect of source suspended sediment concentration on the sediment dynamics of a macrotidal creek and salt marsh. *Continental Shelf Research*, *148*, 130–138. https://doi.org/10.1016/J.CSR.2017.08.017

Pontee, N. I. (2013). Assessing Coastal Habitat Loss: The Role of Coastal Squeeze. *Bulletin of the Chartered Institute of Ecology and Environmental Management, 80*, 31–34.

Portet, S. (2020). A primer on model selection using the Akaike Information Criterion. *Infectious Disease Modelling*, *5*, 111–128. https://doi.org/10.1016/j.idm.2019.12.010

Purcell, J. (2020). *Application of managed dyke realignment and hydrodynamic modelling for flood mitigation in Truro, Nova Scotia*. [Master's thesis, Saint Mary's University]. Saint Mary's University Institutional Repository. https://library2.smu.ca/handle/01/29490

Reed, D. J., Spencer, T., Murray, A. L., French, J. R., & Leonard, L. (1999). Marsh surface sediment deposition and the role of tidal creeks: Implications for created and managed coastal marshes. *Journal of Coastal Conservation, 5*(1), 81–90. https://doi.org/10.1007/BF02802742

Richard, G. A. (1978). Seasonal and Environmental Variations in Sediment Accretion in a Long Island Salt Marsh. *Estuaries*, *1*(1), 29–35. https://doi.org/10.2307/1351647

Schile, L. M., Callaway, J. C., Morris, J. T., Stralberg, D., Thomas Parker, V., & Kelly, M. (2014). Modeling tidal marsh distribution with sea-level rise: Evaluating the role of vegetation, sediment, and upland habitat in marsh resiliency. *PLoS ONE, 9*(2). https://doi.org/10.1371/journal.pone.0088760

Shepard, C. C., Crain, C. M., & Beck, M. W. (2011). The protective role of coastal marshes: A systematic review and meta-analysis. *PLoS ONE*, *6*(11). https://doi.org/10.1371/journal.pone.0027374

Sherren, K., Ellis, K., Guimond, J. A., Kurylyk, B., LeRoux, N., Lundholm, J., Mallory, M. L., Van Proosdij, D., Walker, A. K., Bowron, T. M., Brazner, J., Kellman, L., Turner, B. L., & Wells, E. (2021). Understanding multifunctional Bay of Fundy dykelands and tidal wetlands using ecosystem services-a baseline. *Facets*, *6*, 1446–1473. https://doi.org/10.1139/FACETS-2020-0073

Singh, K., Walters, B. B., & Ollerhead, J. (2007). Climate change, sea-level rise and the case for salt marsh restoration in the Bay of Fundy, Canada. *Environments, 35*(2), 71–84.

Temmerman, S., Govers, G., Wartel, S., & Meire, P. (2003). Spatial and temporal factors controlling short-term sedimentation in a salt and freshwater tidal marsh, scheldt estuary, Belgium, SW Netherlands. *Earth Surface Processes and Landforms, 28*(7), 739–755. https://doi.org/10.1002/esp.495

Torio, D. D., & Chmura, G. L. (2016). Assessing Coastal Squeeze of Tidal Wetlands. *Journal of Coastal Research, 29*(5), 1049–1061.

Traynum, S., & Styles, R. (2007). Flow, stress and sediment resuspension in a shallow tidal channel. *Estuaries and Coasts, 30*(1), 94–101. https://doi.org/10.1007/BF02782970

Valiela, I., Lloret, J., Bowyer, T., Miner, S., Remsen, D., Elmstrom, E., Cogswell, C., & Robert Thieler, E. (2018). Transient coastal landscapes: Rising sea level threatens salt marshes. *Science of the Total Environment, 640–641*, 1148–1156. https://doi.org/10.1016/j.scitotenv.2018.05.235

van de Kreeke, J. (2004). Equilibrium and cross-sectional stability of tidal inlets: Application to the Frisian Inlet before and after basin reduction. *Coastal Engineering, 51*(5–6), 337–350. https://doi.org/10.1016/j.coastaleng.2004.05.002

van Proosdij, D. (2001). *Spatial and Temporal Controls on the Sediment Budget of a Macrotidal Saltmarsh*. [PhD thesis, The University of Guelph]. University of Guelph Institutional Repository. https://atrium.lib.uoguelph.ca/xmlui/handle/10214/24801

van Proosdij, D., Davidson-Arnott, R. G. D., & Ollerhead, J. (2006). Controls on spatial patterns of sediment deposition across a macro-tidal salt marsh surface over single tidal cycles. *Estuarine, Coastal and Shelf Science*, *69*(1–2), 64–86. https://doi.org/10.1016/j.ecss.2006.04.022

van Proosdij, D., Elliott, M., Lewis, S., Graham, J., Nichols, K., & Bowron, T. (2023). *Influence of hydrodynamic and sedimentary processes on tidal wetland landscape evolution for Making Room for Wetlands in the Bay of Fundy*. [Conference Abstract]. EGU General Assembly 2023, Vienna, Austria, 24–28 Apr 2023, EGU23-15798. https://doi.org/10.5194/egusphere-egu23-15798.

van Proosdij, D., Lundholm, J., Neatt, N., Bowron, T., & Graham, J. (2010). Ecological re-engineering of a freshwater impoundment for salt marsh restoration in a hypertidal system. *Ecological Engineering, 36*(10), 1314–1332. https://doi.org/10.1016/j.ecoleng.2010.06.008

van Proosdij, D., O'Laughlin, C., Milligan, T., Law, B., & Spooner, I. (2013). *Effects of Energy Extraction on Sediment Dynamics in Intertidal Ecosystems of the Minas Basin*. Offshore Energy Environmental Research Association. https://oera.ca/sites/default/files/2019-05/Effects%20of%20Energy%20Extraction%20on%20Sediment%20Dynamics%20in%20Intertidal%20Ecosystems%20of%20the%20Minas%20Basin%20%E2%80%93%20Final%20Report.pdf

van Proosdij, D., & Page, S. (2012). *Best management practices for climate change adaptation in dykelands: Recommendations for Fundy ACAS sites*. Atlantic Climate Adaptations Solutions Association. https://atlanticadaptation.ca/objects/acasa_279.html van Proosdij, D., Ross, C., & Matheson, G. (2018). *Risk Proofing Nova Scotia Agriculture: Nova Scotia Dyke Vulnerability Assessment*. Prepared for the Nova Scotia Federation of Agriculture. https://nsfa-fane.ca/wp-content/uploads/2018/08/Nova-Scotia-Dyke-Vulnerability-Assessment.pdf

Virgin, S. D. S., Beck, A. D., Boone, L. K., Dykstra, A. K., Ollerhead, J., Barbeau, M. A., & McLellan, N. R. (2020). A managed realignment in the upper Bay of Fundy: Community dynamics during salt marsh restoration over 8 years in a megatidal, ice-influenced environment. *Ecological Engineering*, *149*, 105713. https://doi.org/10.1016/j.ecoleng.2020.105713

Voulgaris, G., & Meyers, S. T. (2004). Temporal variability of hydrodynamics, sediment concentration and sediment settling velocity in a tidal creek. *Continental Shelf Research, 24*(15), 1659–1683. https://doi.org/10.1016/j.csr.2004.05.006

Vrieze, S. I. (2012). Model selection and psychological theory: A discussion of the differences between the Akaike Information Criterion (AIC) and the Bayesian Information Criterion (BIC). *Psychological Methods*, *17*(2), 228–243. https://doi.org/10.1037/a0027127

Vuik, V. (2019). *Building safety with nature salt marshes for flood risk reduction.* [PhD thesis, Delft University of Technology]. https://doi.org/10.4233/uuid:9339474c-3c48-437f-8aa5-4b908368c17e

Wang, Y. P., Voulgaris, G., Li, Y., Yang, Y., Gao, J., Chen, J., & Gao, S. (2013). Sediment resuspension, flocculation, and settling in a macrotidal estuary. *Journal of Geophysical Research: Oceans*, *118*(10), 5591–5608. https://doi.org/10.1002/jgrc.20340

Winterwerp, J. C. (1998). A simple model for turbulence induced flocculation of cohesive sediment. *Journal of Hydraulic Research*, *36*(3), 309–326. https://doi.org/10.1080/00221689809498621

Winterwerp, J. C., Manning, A. J., Martens, C., de Mulder, T., & Vanlede, J. (2006). A heuristic formula for turbulence-induced flocculation of cohesive sediment. *Estuarine, Coastal and Shelf Science, 68*(1), 195–207. https://doi.org/10.1016/j.ecss.2006.02.003

Wollenberg, J. T., Ollerhead, J., & Chmura, G. L. (2018). Rapid carbon accumulation following managed realignment on the Bay of Fundy. *PLOS ONE 13*(3), e0193930. https://doi.org/10.1371/journal.pone.0193930

Xie, D., Gao, S., & Pan, C. (2010). Process-based modeling of morphodynamics of a tidal inlet system. *Acta Oceanologica Sinica*, *29*(6), 51–61. https://doi.org/10.1007/s13131-010-0076-1

APPENDIX A

Table A-1. Coordinates and elevation values of stations.

Station	Elevation (CGDV 2013)	Latitude (WGS84)	Longitude (WGS84)
RS1	5.87	45.8429	-64.2673
RS2	5.53	45.8432	-64.2678
RS3	5.14	45.8434	-64.2683
RS4	6.05	45.8426	-64.2694
RS5	5.64	45.8418	-64.2689
RS6	5.83	45.8426	-64.2685
MH17	5.76	45.8422	-64.2679
MH13	5.95	45.8404	-64.2687
MH2A	6.12	45.8409	-64.2687
MH09	6.40	45.8402	-64.2697
MH11	5.76	45.8411	-64.2703
MH03	5.88	45.8408	-64.2719
MH01	5.79	45.8398	-64.2732
MH05	6.36	45.8426	-64.2735

Table A-2. Deposition values of each station for each tide of all deployments in mg·m^{-2}.

Station	**August 2020**					**November 2020**				**July 2021**			
	T2	**T3**	**T4**	**T5**	**T6**	**T1**	**T2**	**T3**	**T4**	**T2**	**T3**	**T4**	**T5**
RS1	52.0	29.0	68.0	29.0	36.0	23.0	37.0	36.0	750.0	29.0	130.0	29.0	59.0
RS2	260.0	130.0	290.0	110.0	280.0	220.0	290.0	540.0	1100.0	29.0	750.0	30.0	460.0
RS3	590.0	380.0	400.0	200.0	570.0	390.0	930.0	740.0	1400.0	180.0	850.0	730.0	870.0
RS4	190.0	150.0	180.0	140.0	32.0	5.2	190.0	83.0	450.0		140.0		180.0
RS5	470.0	470.0	420.0	390.0	510.0	290.0	1000.0	510.0	1200.0	75.0	660.0	540.0	730.0
RS6	44.0	41.0	35.0	31.0	28.0	31.0	16.0	15.0	40.0	57.0	43.0	51.0	17.0
MH17	91.0	120.0	140.0	79.0	71.0	18.0	34.0	22.0	120.0	70.0	87.0	35.0	97.0
MH13	290.0	230.0	49.0	160.0	150.0	59.0	61.0	100.0	550.0	280.0	280.0	36.0	220.0
MH2A	200.0	67.0	140.0	100.0	75.0	22.0	320.0	180.0	620.0		60.0		87.0
MH09	39.0	27.0	34.0		56.0		42.0	5.8	250.0		18.0		21.0
MH11	420.0	280.0	330.0	270.0	250.0	150.0	490.0	420.0	640.0	91.0	440.0	170.0	380.0
MH03	210.0	150.0	190.0	120.0	78.0	26.0	220.0	160.0	570.0		120.0	19.0	93.0
MH01	360.0	79.0	260.0	180.0	120.0	120.0	160.0	290.0	510.0		740.0	90.0	450.0
MH05	27.0		21.0		30.0		34.0	140.0					15.0

Table A-3. Tidal scrape sample data for station RS1 with D50, floc fraction, and number of samples.

	Deposition			RSB		
Deployment	**D50 (µm)**	**Floc fraction**	**Number of Samples**	**D50 (µm)**	**Floc fraction**	**Number of Samples**
Aug 2020	7.4	0.91	3	4.9	0.93	1
Nov 2020	8.4	0.84	3			0
Jul 2021	7.0	0.92	2	4.4	0.94	2

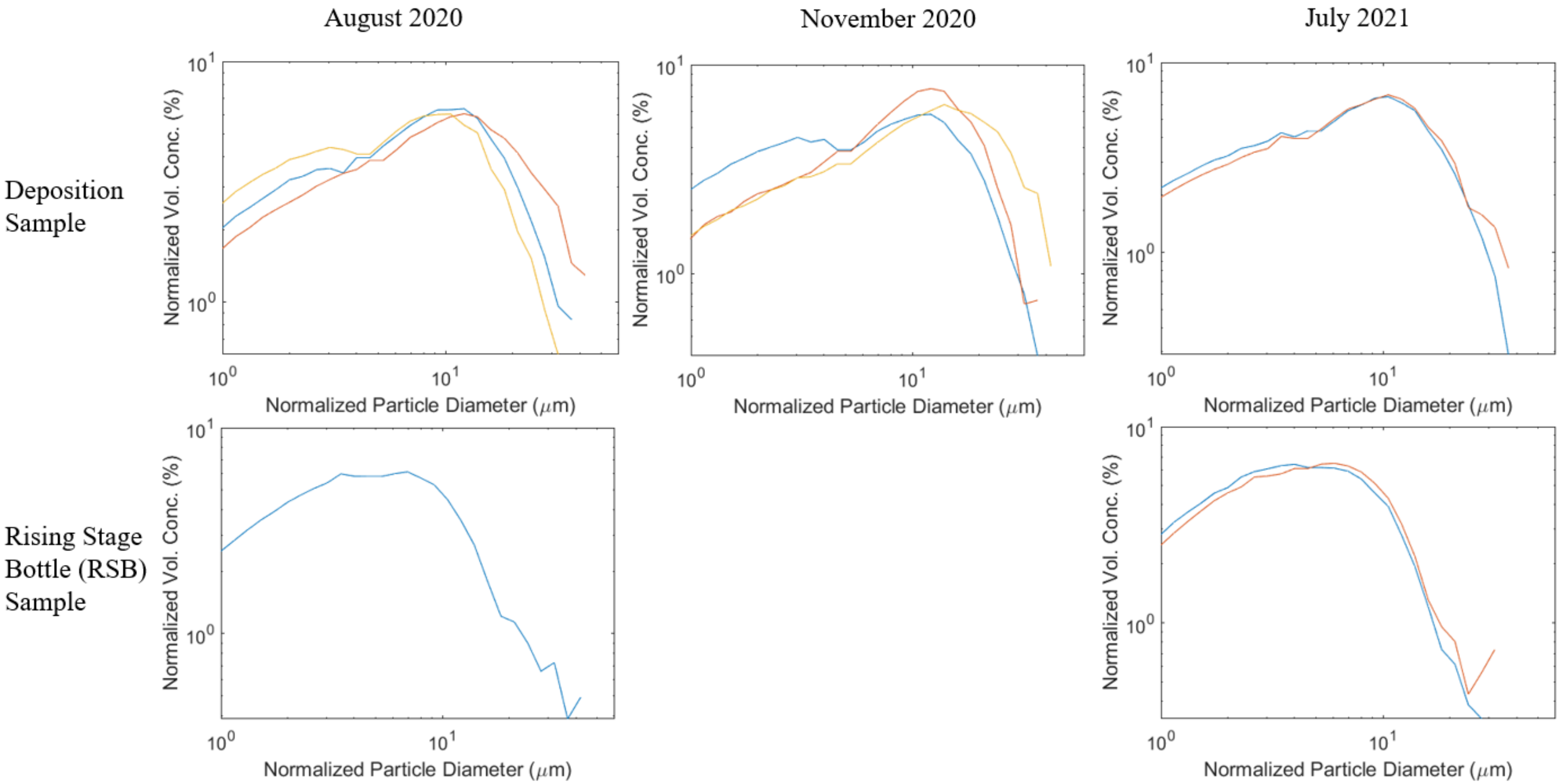

Figure A.1. Disaggregated inorganic grain size plots for station RS1, with different colours representing separate tides.

Table A-4. Tidal scrape sample data for station RS2 with D50, floc fraction, and number of samples.

	Deposition			RSB		
Deployment	**D50 (µm)**	**Floc fraction**	**Number of Samples**	**D50 (µm)**	**Floc fraction**	**Number of Samples**
Aug 2020	8.1	0.91	5			0
Nov 2020	9.6	0.90	3	8.7	0.92	1
Jul 2021	7.8	0.91	4	5.9	0.93	2

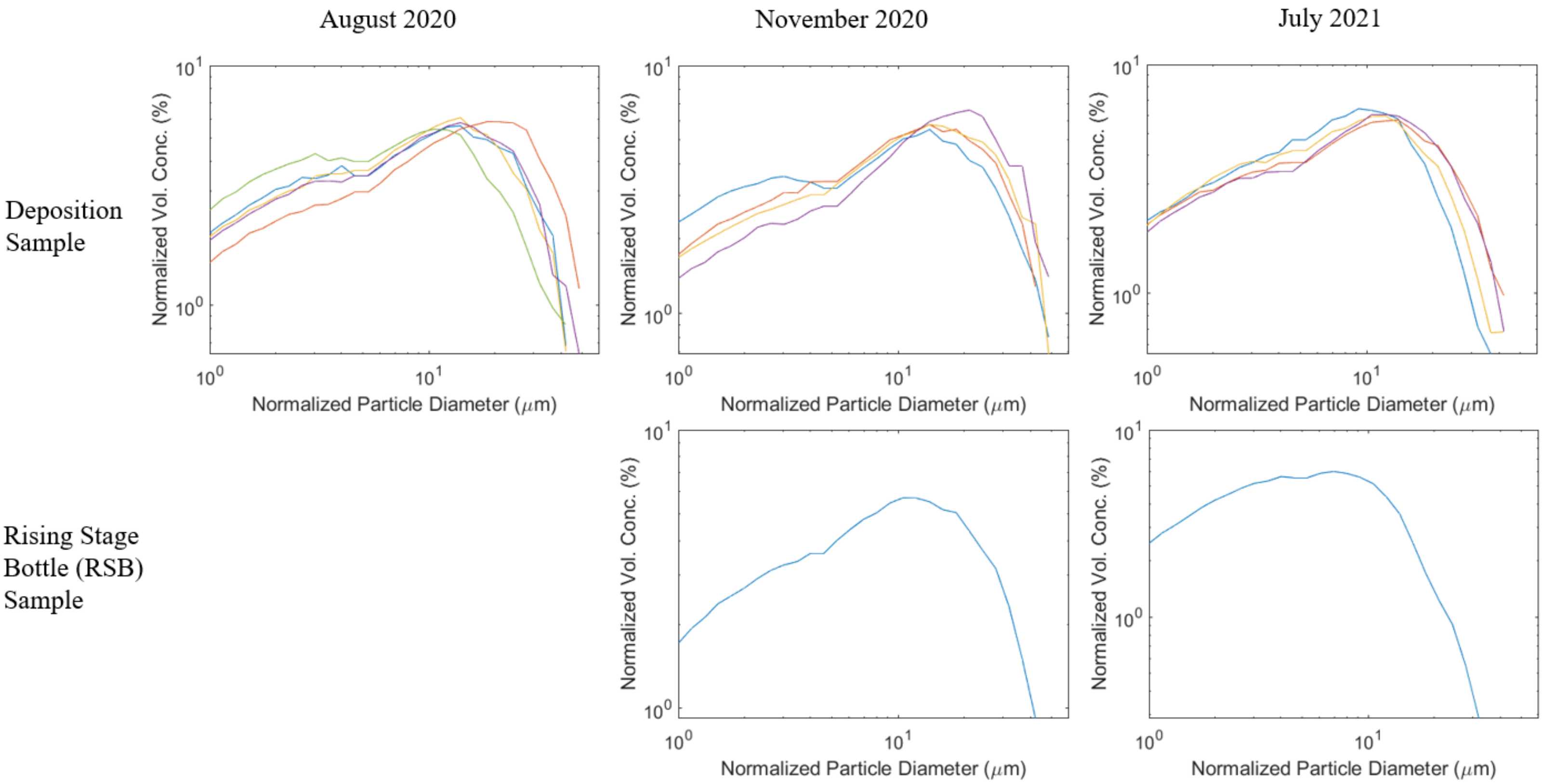

Figure A.2. Disaggregated inorganic grain size plots for station RS2, with different colours representing separate tides.

Table A-5. Tidal scrape sample data for station RS3 with D50, floc fraction, and number of samples.

	Deposition			RSB		
Deployment	**D50 (µm)**	**Floc fraction**	**Number of Samples**	**D50 (µm)**	**Floc fraction**	**Number of Samples**
Aug 2020	10.0	0.90	5	6.9	0.93	1
Nov 2020	9.4	0.90	4	7.1	0.90	1
Jul 2021	8.6	0.90	4	0.9	0.92	3

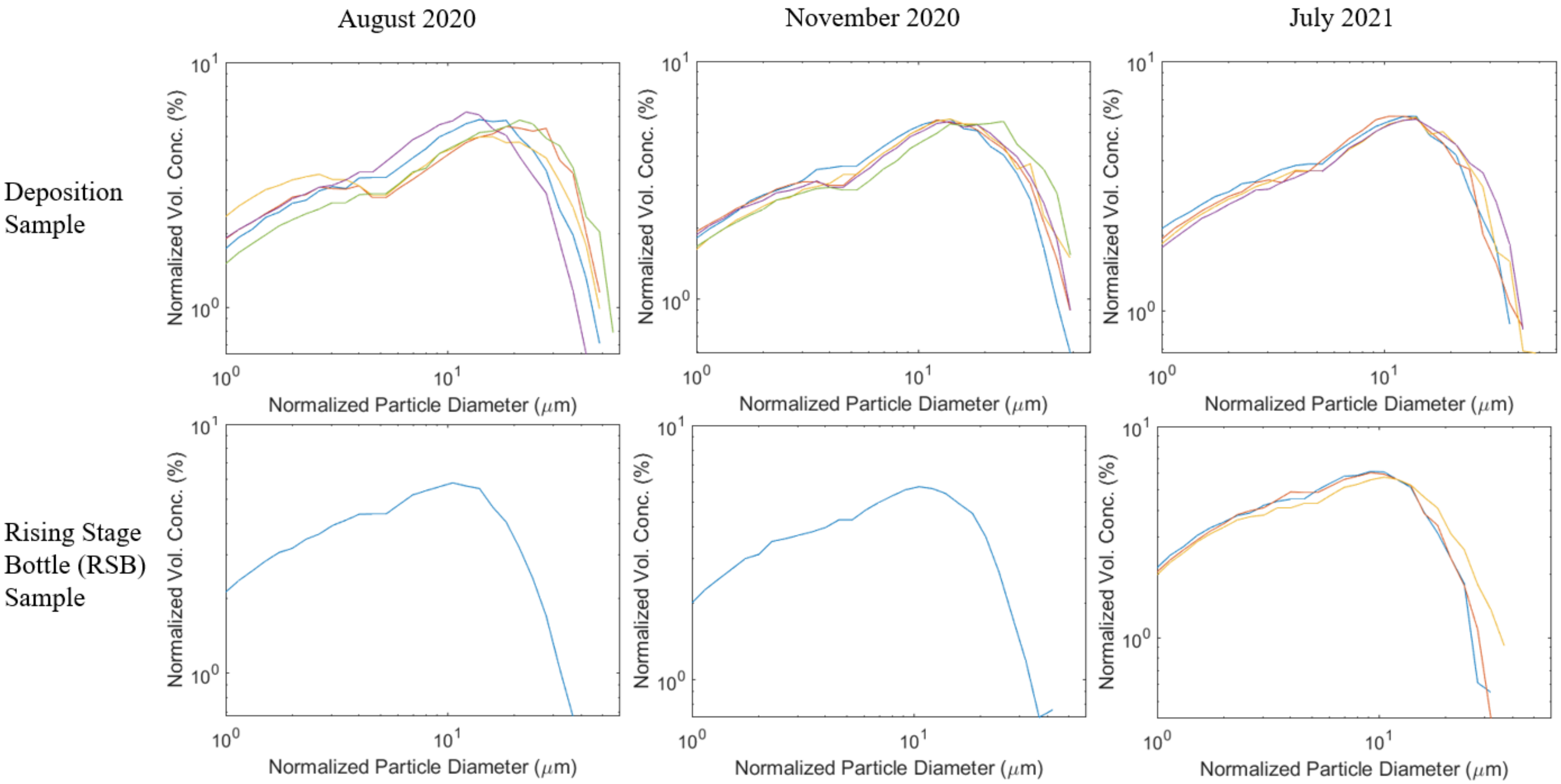

Figure A.3. Disaggregated inorganic grain size plots for station RS3, with different colours representing separate tides.

Table A-6. Tidal scrape sample data for station RS4 with D50, floc fraction, and number of samples.

	Deposition			**RSB**		
Deployment	**D50 (μm)**	**Floc fraction**	**Number of Samples**	**D50 (μm)**	**Floc fraction**	**Number of Samples**
Aug 2020	9.0	0.90	4	8.2	0.91	1
Nov 2020	11.2	0.90	3	8.4	0.91	1
Jul 2021	8.5	0.91	2	6.7	0.93	2

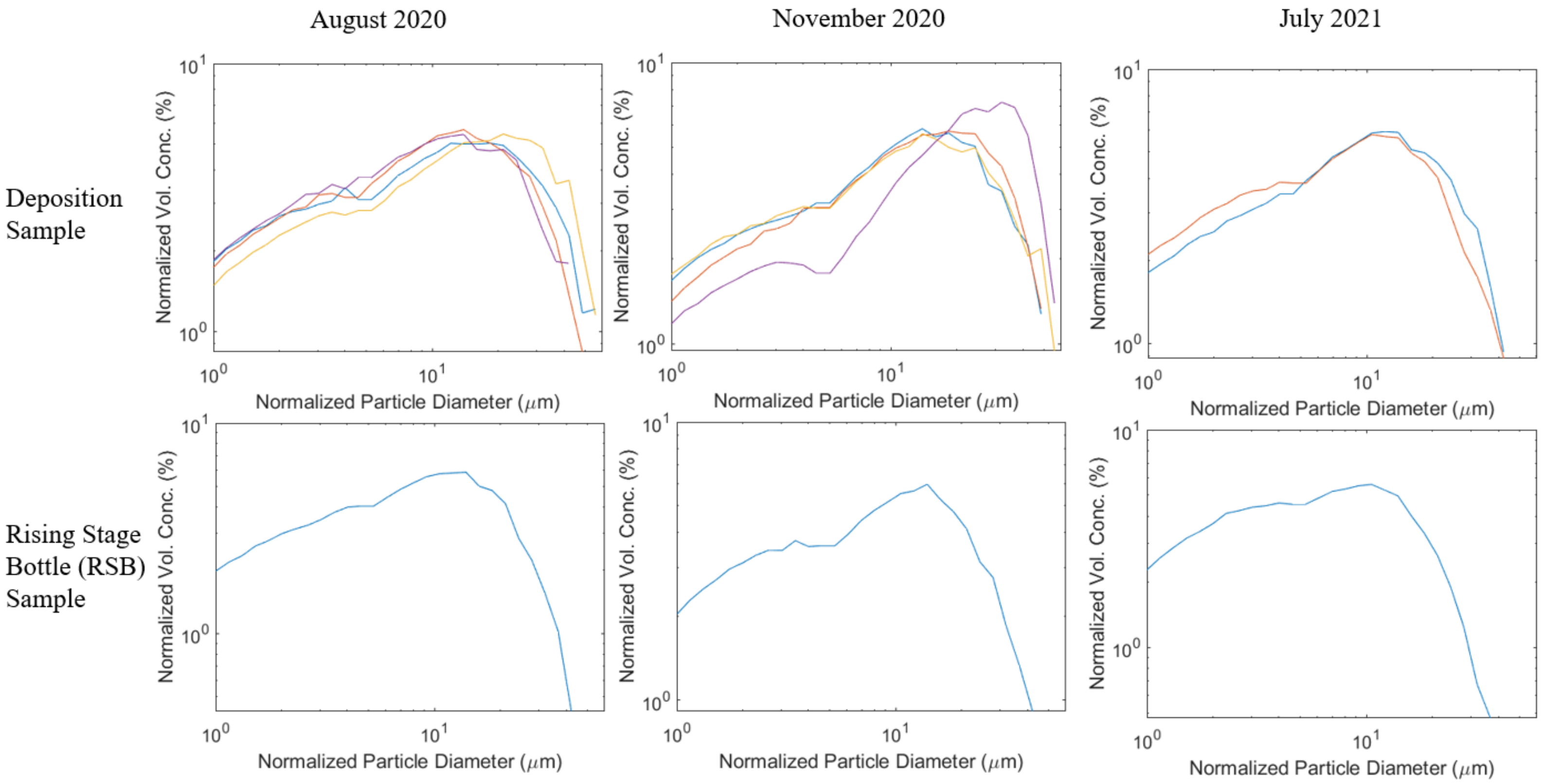

Figure A.4. Disaggregated inorganic grain size plots for station RS4, with different colours representing separate tides.

Table A-7. Tidal scrape sample data for station RS5 with D50, floc fraction, and number of samples.

	Deposition			RSB		
Deployment	**D50 (µm)**	**Floc fraction**	**Number of Samples**	**D50 (µm)**	**Floc fraction**	**Number of Samples**
Aug 2020	9.7	0.89	5			0
Nov 2020	11.4	0.80	3	9.4	0.89	1
Jul 2021	9.1	0.90	4	6.7	0.91	4

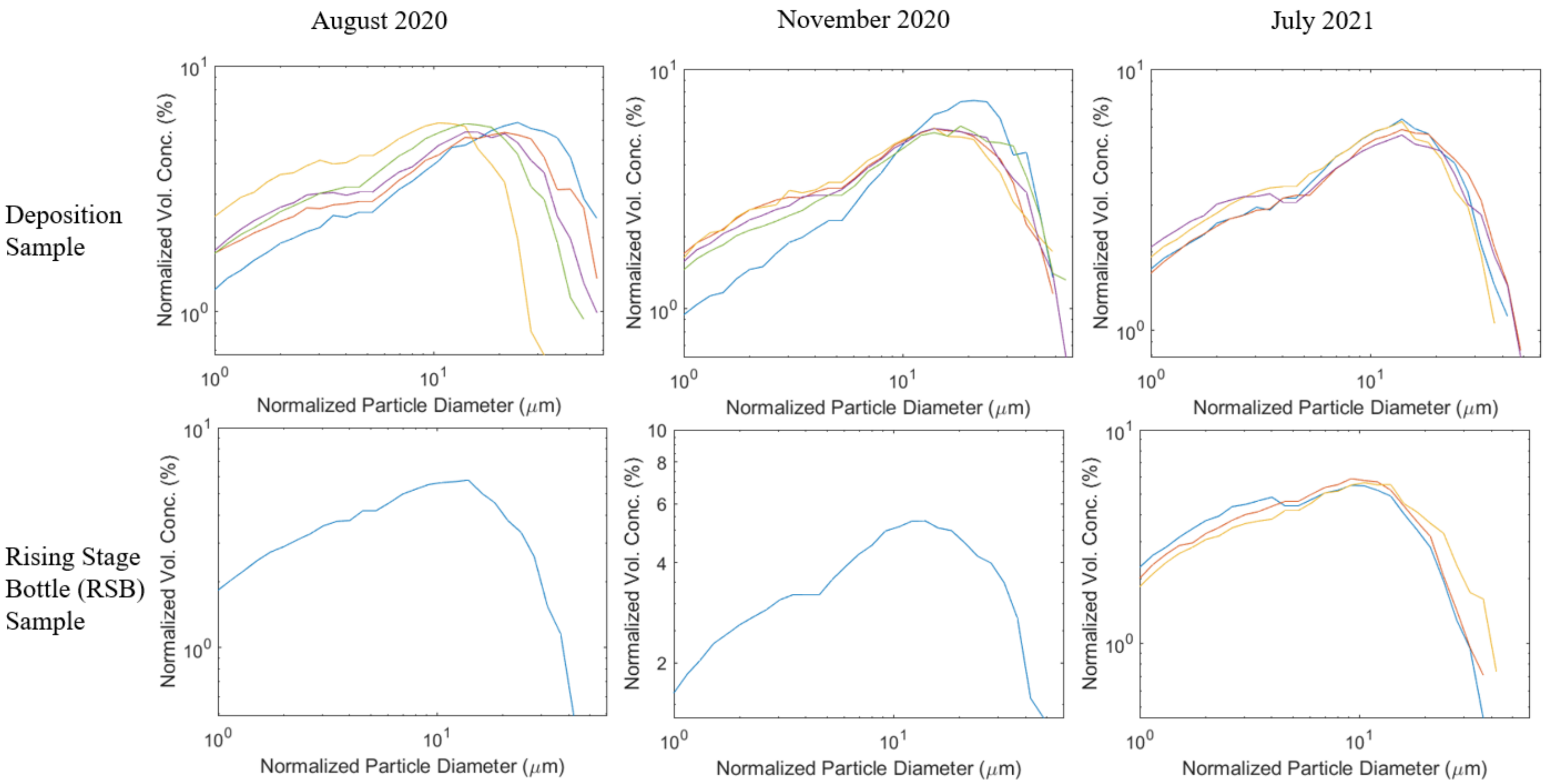

Figure A.5. Disaggregated inorganic grain size plots for station RS5, with different colours representing separate tides.

Table A-8. Tidal scrape sample data for station RS6 with D50, floc fraction, and number of samples.

	Deposition			**RSB**		
Deployment	**D50 (µm)**	**Floc fraction**	**Number of Samples**	**D50 (µm)**	**Floc fraction**	**Number of Samples**
Aug 2020	12.9	0.86	4	8.2	0.93	1
Nov 2020	16.4	0.60	3	6.9	0.92	1
Jul 2021	8.2	0.91	4	4.5	0.95	2

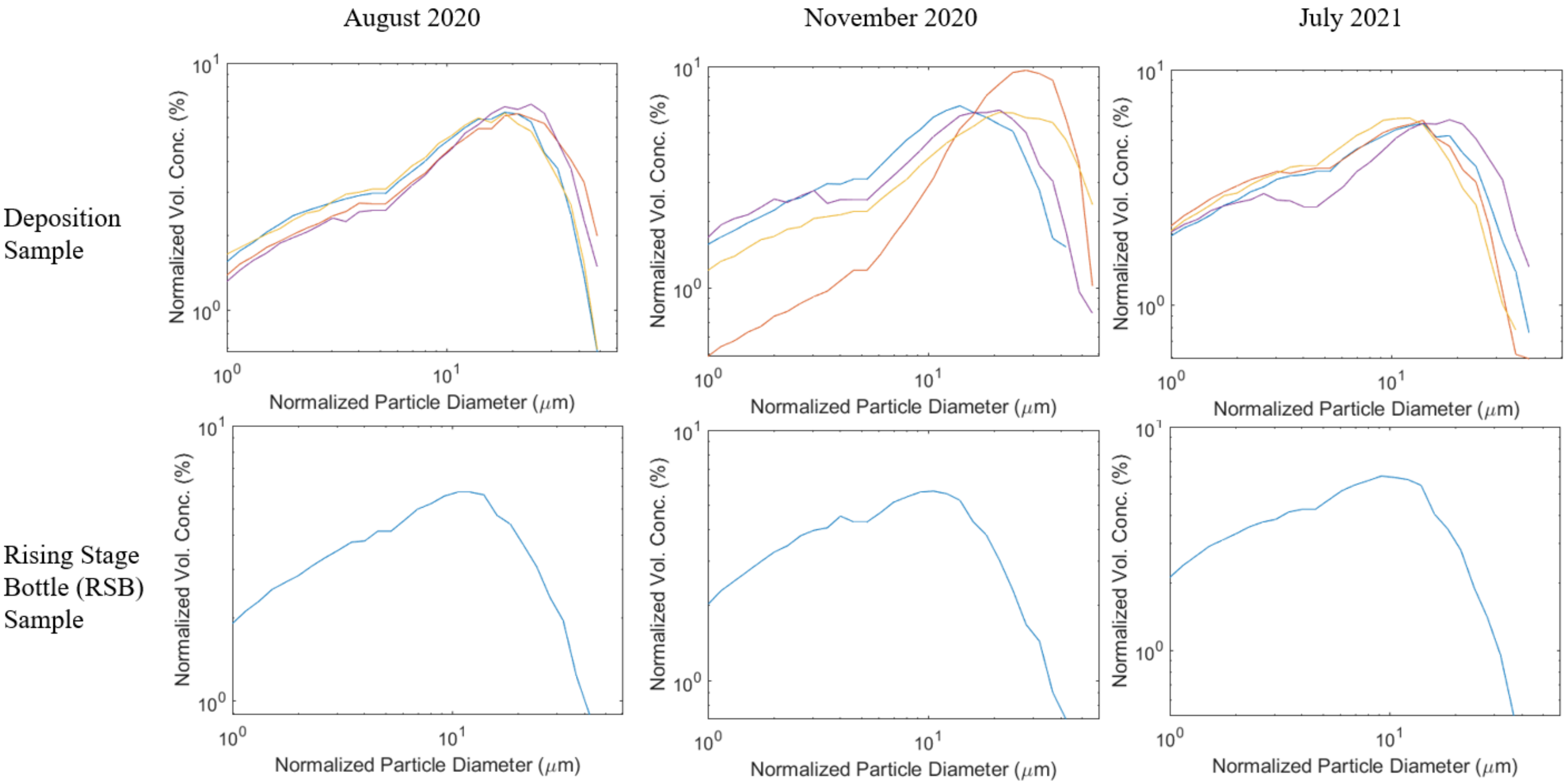

Figure A.6. Disaggregated inorganic grain size plots for station RS6, with different colours representing separate tides.

Table A-9. Tidal scrape sample data for station MH17 with D50, floc fraction, and number of samples.

Deployment	D50 (μm)	Floc fraction	Number of Samples
Aug 2020	13.6	0.77	4
Nov 2020	21.3	0.68	2
Jul 2021	8.3	0.90	3

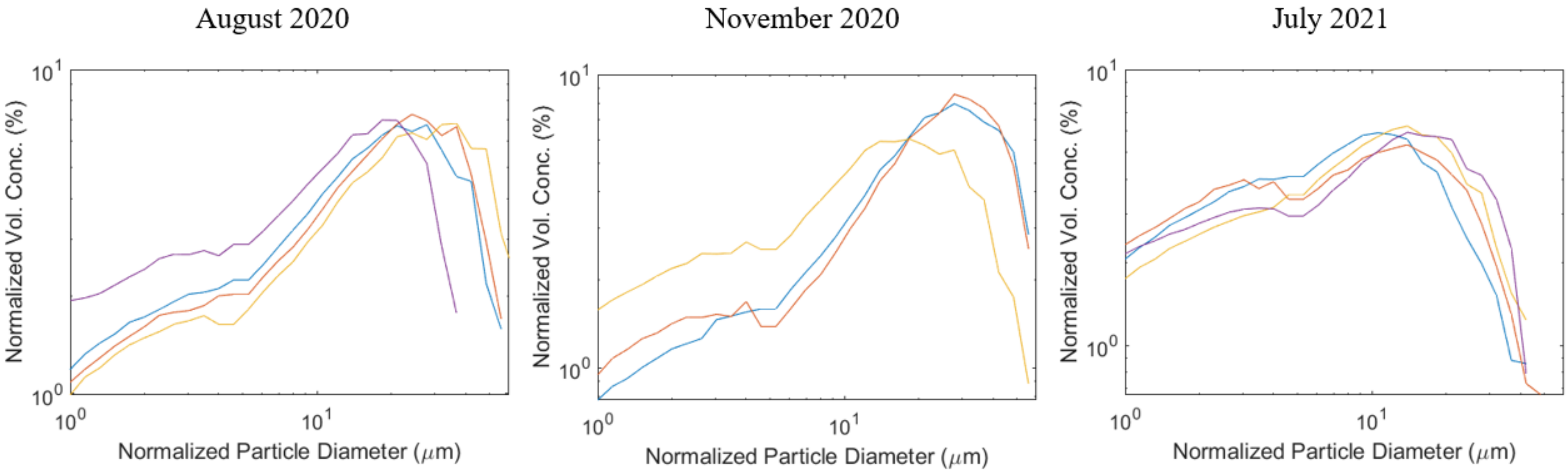

Figure A.7. Disaggregated inorganic grain size plots for station MH17, with different colours representing separate tides.

Table A-10. Tidal scrape sample data for station MH13 with D50, floc fraction, and number of samples.

Deployment	D50 (μm)	Floc fraction	Number of Samples
Aug 2020	8.7	0.90	5
Nov 2020	12.0	0.74	3
Jul 2021	7.9	0.85	3

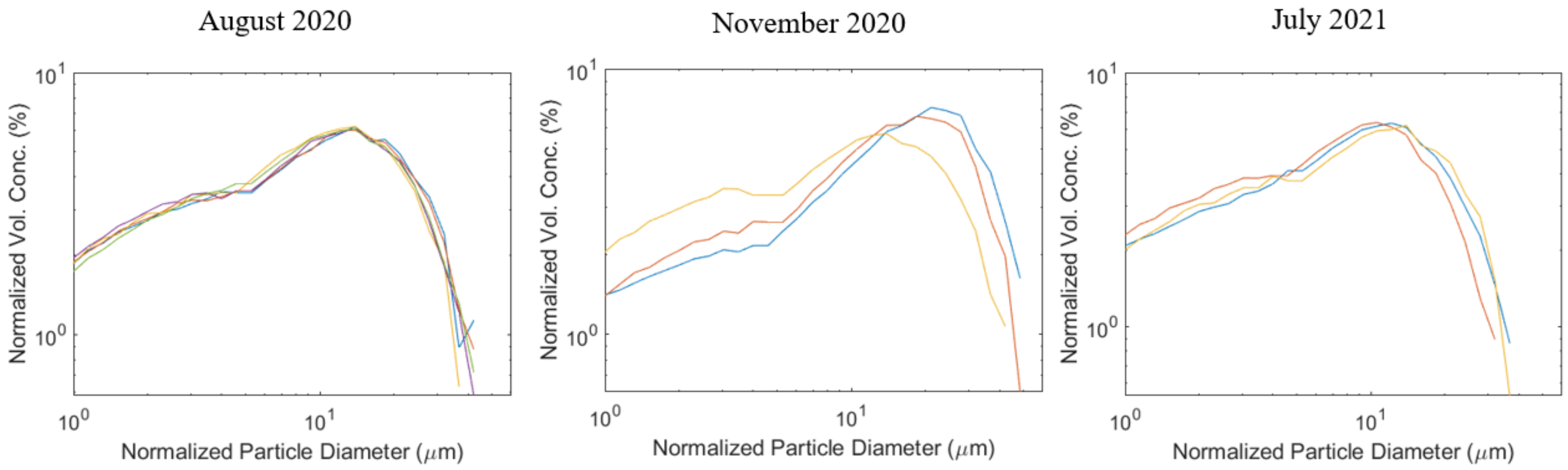

August 2020

November 2020

July 2021

Figure A.8. Disaggregated inorganic grain size plots for station MH13, with different colours representing separate tides.

Table A-11. Tidal scrape sample data for station MH11 with D50, floc fraction, and number of samples.

Deployment	D50 (μm)	Floc fraction	Number of Samples
Aug 2020	8.6	0.89	4
Nov 2020	10.5	0.85	4
Jul 2021	8.4	0.78	3

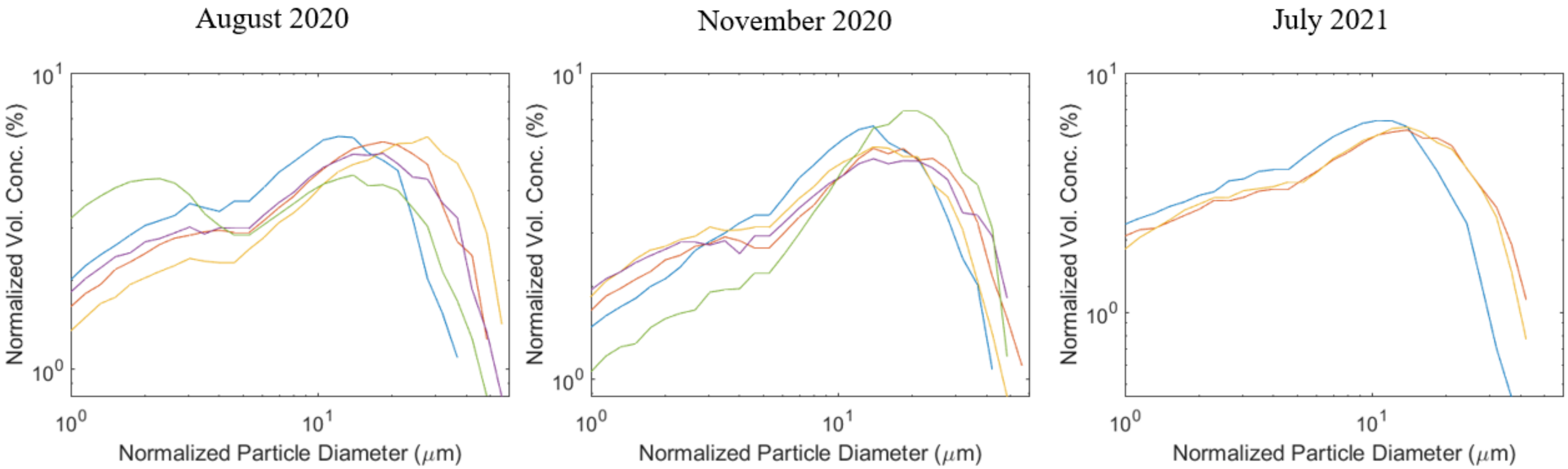

Figure A.9. Disaggregated inorganic grain size plots for station MH11, with different colours representing separate tides.

Table A-12. Tidal scrape sample data for station MH09 with D50, floc fraction, and number of samples.

Deployment	D50 (µm)	Floc fraction	Number of Samples
Aug 2020			0
Nov 2020	7.2	0.79	1
Jul 2021			0

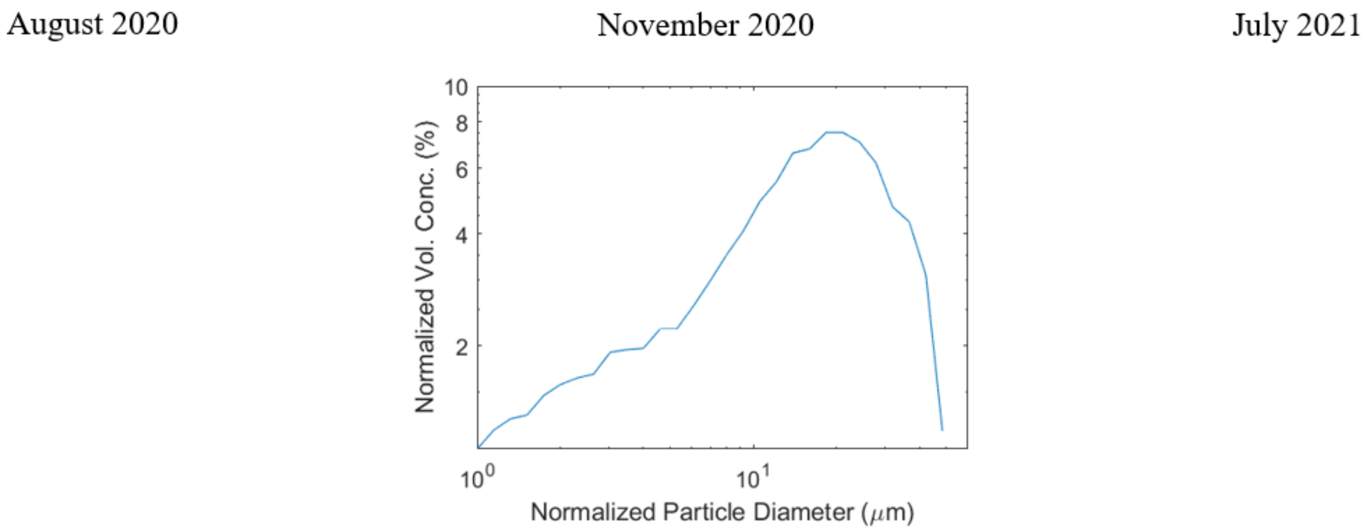

August 2020

November 2020

July 2021

Figure A.10. Disaggregated inorganic grain size plots for station MH09, with different colours representing separate tides.

Table A-13. Tidal scrape sample data for station MH05 with D50, floc fraction, and number of samples.

Deployment	D50 (µm)	Floc fraction	Number of Samples
Aug 2020			0
Nov 2020	8.5	0.80	1
Jul 2021			0

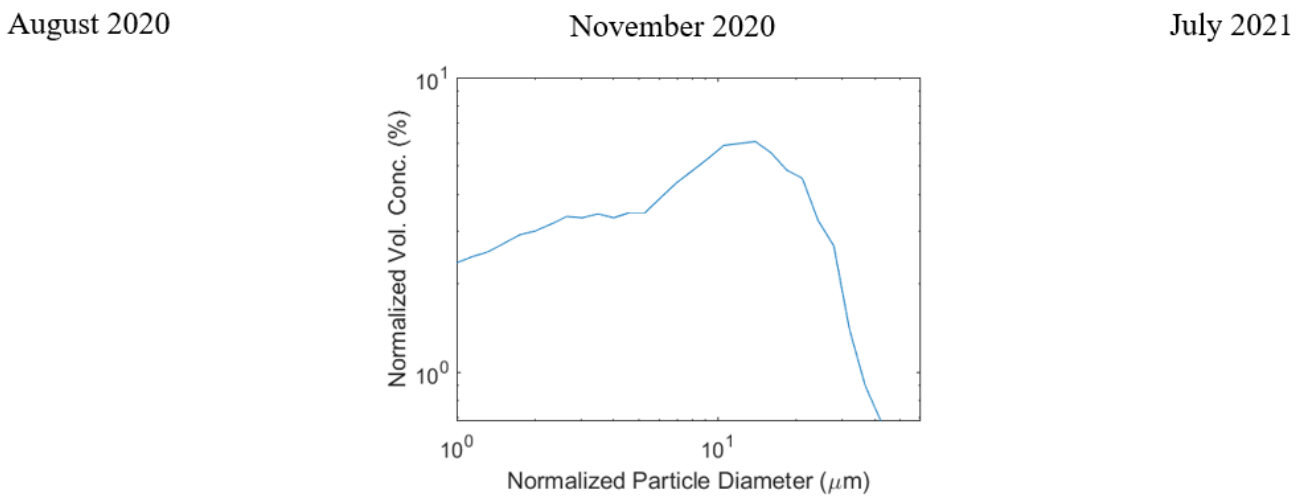

August 2020

November 2020

July 2021

Figure A.11. Disaggregated inorganic grain size plots for station MH05, with different colours representing separate tides.

Table A-14. Tidal scrape sample data for station MH03 with D50, floc fraction, and number of samples.

Deployment	D50 (μm)	Floc fraction	Number of Samples
Aug 2020	9.3	0.90	2
Nov 2020	8.7	0.91	3
Jul 2021	9.7	0.91	2

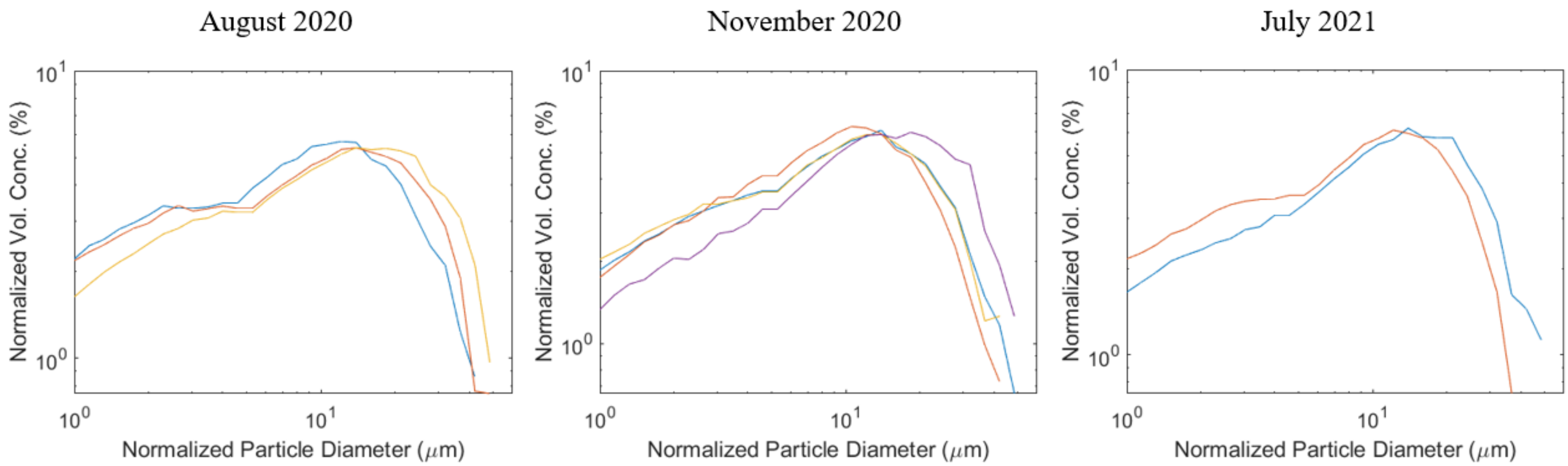

Figure A.12. Disaggregated inorganic grain size plots for station MH03, with different colours representing separate tides.

Table A-15. Tidal scrape sample data for station MH2A with D50, floc fraction, and number of samples.

Deployment	D50 (µm)	Floc fraction	Number of Samples
Aug 2020	10.6	0.89	1
Nov 2020	9.1	0.86	3
Jul 2021	6.5	0.91	1

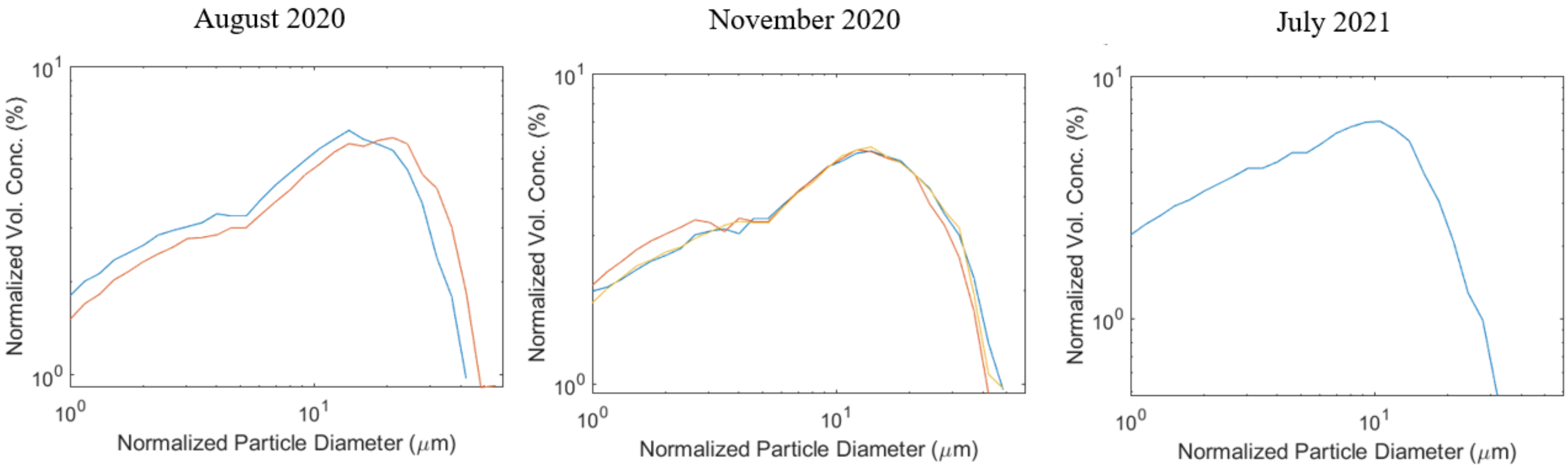

Figure A.13. Disaggregated inorganic grain size plots for station MH2A, with different colours representing separate tides.

Table A-16. Tidal scrape sample data for station MH01 with D50, floc fraction, and number of samples.

Deployment	D50 (μm)	Floc fraction	Number of Samples
Aug 2020	9.4	0.89	5
Nov 2020	8.3	0.90	4
Jul 2021	7.8	0.90	3

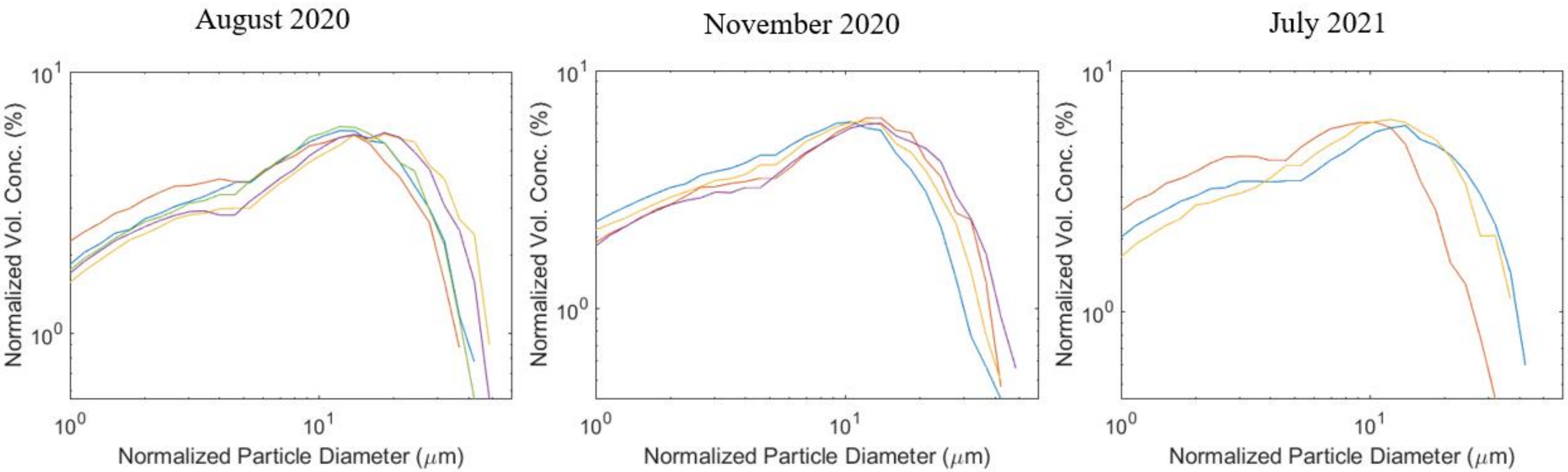

Figure A.14. Disaggregated inorganic grain size plots for station MH01, with different colours representing separate tides.

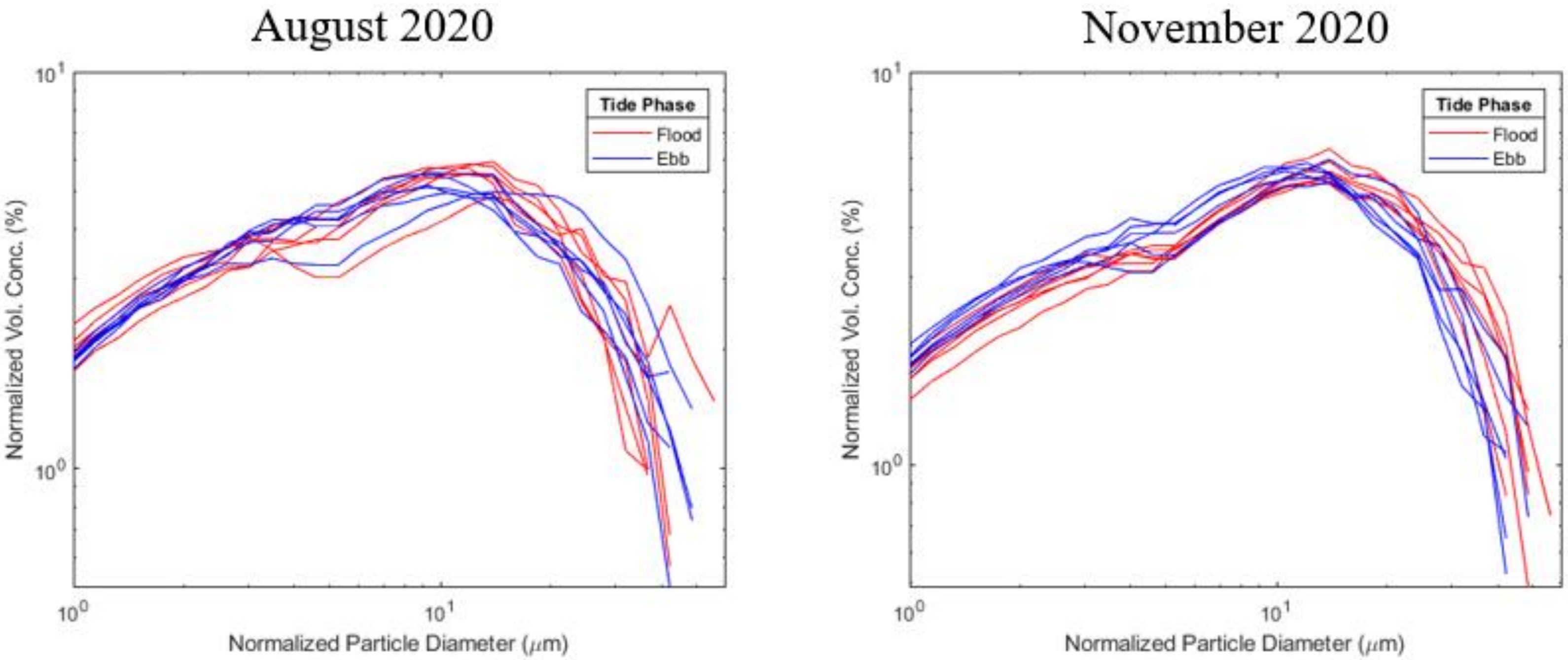

Figure A.15. Disaggregated inorganic grain size plots for ISCO samples at inlet in August 2020 and November 2020, separated by flood and ebb tides.

APPENDIX B

The tables in this section describe the combinations of variables that were tested in a more simplistic format, where some cells had multiple models, e.g., each cell for the hydrologic single variables (B-1) and hydrologic expressions (B-2, B-3, B-4, B-6) was tested with the flood and ebb cumulative values and net and average of the flood and ebb cumulative values. Multiple models are indicated in the table description.

Table B-1. Single variable regression test matrix. Flood and ebb cumulative values and net and average of flood and ebb cumulative values for this matrix were tested.

	Linear	**Polynomial second order**	**Polynomial third order**	**Exponential**	**Power**
$\boldsymbol{Depth}$	-	-	-	-	-
$\boldsymbol{Widths}$	-	-	-	-	-
$\boldsymbol{Area}$	-	-	-	-	-
$\boldsymbol{Velocity}$	-	-	-	-	-
$\boldsymbol{Discharge}$	-	-	-	-	-
$\boldsymbol{SSC}$	-	-	-	-	-
$\boldsymbol{Sediment\ Flux}$	-	-	-	-	-
$\boldsymbol{Elevation}$	-	-	-	-	-
$\boldsymbol{Dc}$	-	-	-	-	-
$\boldsymbol{Di}$	-	-	-	-	-
$\boldsymbol{PMTH}$	-	-	-	-	-

Table B-2. Level 1 hydrologic variable formula test matrix. Flood and ebb cumulative values and net and average of flood and ebb cumulative values for this matrix were tested.

	Linear	**Polynomial third order**
$\boldsymbol{Depth + Widths}$	-	-
$\boldsymbol{Depth * Widths}$	-	-
$\boldsymbol{Area}$	-	-

Table B-3. Level 2 hydrologic variable formula test matrix. Flood and ebb cumulative values and net and average of flood and ebb cumulative values for this matrix were tested.

		Linear	**Polynomial third order**
Primary	$Depth + Widths + Velocity$	-	-
	$Area + Velocity$	-	-
	$Depth * Widths * Velocity$	-	-
	$Area * Velocity$	-	-
	$Discharge$	-	-
Alternatives	$Depth + Velocity$	-	-
	$Widths + Velocity$	-	-
	$Depth * Velocity$	-	-
	$Widths * Velocity$	-	-

Table B-4. Level 3 hydrologic variable formula test matrix. Flood and ebb cumulative values and net and average of flood and ebb cumulative values for this matrix were tested.

		Linear	**Polynomial third order**
Primary	$Depth + Widths + Velocity + SSC$	-	-
	$Area + Velocity + SSC$	-	-
	$Discharge + SSC$	-	-
	$Sediment\ Flux$	-	-
	$Depth * Widths * Velocity * SSC$	-	-
	$Area * Velocity * SSC$	-	-
	$Discharge * SSC$	-	-
Level 1 Alternatives	$Depth + Widths + SSC$	-	-
	$Depth + Velocity + SSC$	-	-
	$Widths + Velocity + SSC$	-	-
	$Depth + SSC$	-	-
	$Widths + SSC$	-	-
	$Velocity + SSC$	-	-
	$Depth * Widths * SSC$	-	-
	$Depth * Velocity * SSC$	-	-
	$Widths * Velocity * SSC$	-	-
	$Depth * SSC$	-	-
	$Widths * SSC$	-	-
	$Velocity * SSC$	-	-
Level 2 Alternatives	$Area + SSC$	-	-
	$Area * SSC$	-	-

Table B-5. Topographic variable formula test matrix.

	Linear	**Polynomial third order**
$\boldsymbol{Elevation}$	-	-
$\boldsymbol{Dc}$	-	-
$\boldsymbol{Di}$	-	-
$\boldsymbol{Elevation + Dc}$	-	-
$\boldsymbol{Elevation \ast Dc}$	-	-
$\boldsymbol{Elevation + Di}$	-	-
$\boldsymbol{Elev \ast Di}$	-	-
$\boldsymbol{Dc + Di}$	-	-
$\boldsymbol{Dc \ast Di}$	-	-
$\boldsymbol{Elevation + Dc + Di}$	-	-
$\boldsymbol{Elevation \ast Dc \ast Di}$	-	-
$\boldsymbol{Elevation + Dc \ast Di}$	-	-
$\boldsymbol{Elevation \ast Dc + Di}$	-	-
$\boldsymbol{Elevation \ast Di + Di}$	-	-

Table B-6. Single topographic and single hydrologic variable test matrix. Flood and ebb cumulative values and net and average of flood and ebb cumulative values were tested. Each cell had a model with the variables multiplied and a model with the variables added.

	$\boldsymbol{Elevation}$	$\boldsymbol{Dc}$	$\boldsymbol{Di}$
$\boldsymbol{Depth}$	-	-	-
$\boldsymbol{Widths}$	-	-	-
$\boldsymbol{Area}$	-	-	-
$\boldsymbol{Velocity}$	-	-	-
$\boldsymbol{SSC}$	-	-	-

Table B-7. Test matrix for combining best topographic formula versus hydrologic formula, based on AIC number.

		$Dep \sim Elevation + (Dc + Dc^2 + Dc^3) * Di$
$Dep \sim Area + Area^2 + Area^3$	*	-
$Dep \sim Area * Velocity$	*	-
$Dep \sim Widths + Depth + Velocity + SSC$	**	-
$Dep \sim Area * SSC$	*	-
$Dep \sim Widths + Depth + SSC$	*	-

*Average of cumulative flood and cumulative ebb values of variables
**Net of cumulative flood and cumulative ebb values of variables

Table B-8. Test matrix of solo polynomial terms within full models for polynomial reduction step.

	Variable	**Variable^2**	**Variable^3**	**Variable + Variable^3**	**Variable + Variable^2**	**Variable^2 + Variable^3**
Dc	-	-	-	-	-	-
$PMTH$	-	-	-	-	-	-
$Area$	-	-	-	-	-	-

Table B-9. Area/Velocity Model Coefficient Estimates, where all variables are scaled in R.

Model Terms	**Coefficient Estimate**
$Dc * Di$	43.000
$Dc^2 * Di$	23.000
$Dc^3 * Di$	7.100
$Velocity_{avg} * Dc^3$	2.400
$Velocity_{avg} * Dc^2$	1.600
Di	1.400
$Area_{avg} * Velocity_{avg} * Dc^2$	1.000
$Velocity_{avg} * Dc$	0.610
$Area_{avg}$	0.370
$Area_{avg} * Velocity_{avg} * Dc^3$	0.360
$Area_{avg} * Velocity_{avg} * Dc$	0.110
$Area_{avg} * Velocity_{avg}$	0.046
$Velocity_{avg}$	0.015
$Elevation$	-0.340
$Area_{avg} * Dc$	-0.630
$Area_{avg} * Dc^2$	-1.100
$Area_{avg} * Dc^3$	-2.400
Dc	-6.400
Dc^2	-26.000
Dc^3	-45.000

Table B-10. Area/SSC Model Coefficient Estimates, where all variables are scaled in R.

Model Terms	**Coefficient Estimate**
$Dc * Di$	45.0000
$Dc^2 * Di$	24.0000
$Dc^3 * Di$	7.2000
Di	1.4000
$Area_{avg} * SSC_{avg} * Dc^2$	1.3000
$Area_{avg} * SSC_{avg} * Dc^3$	0.3700
$Area_{avg}$	0.3200
$Area_{avg} * SSC_{avg} * Dc$	0.1400
$Area_{avg} * SSC_{avg}$	0.0710
SSC_{avg}	-0.0062
$SSC_{avg} * Dc$	-0.0900
$Area_{avg} * Dc$	-0.2100
$Area_{avg} * Dc^3$	-0.2700
Elevation	-0.3600
$Area_{avg} * Dc^2$	-0.6000
$SSC_{avg} * Dc^2$	-0.6100
$SSC_{avg} * Dc^3$	-0.7000
Dc^3	-6.4000
Dc^2	-26.0000
Dc	-47.0000

Table B-11. PMTH Model Coefficient Estimates, where all variables are scaled in R.

Model Terms	**Coefficient Estimate**
$PMTH^2 * Di * Dc^3$	5800.000
$PMTH * Dc^3$	4100.000
$PMTH^3 * Dc^3$	4100.000
$PMTH$	1500.000
$PMTH^3$	1500.000
$PMTH^2 * Elevation$	590.000
$PMTH^2 * Di$	580.000
$Di * Dc^3$	-0.048
Di	-0.120
$PMTH^3$	-0.200
$Elevation$	-0.420
$PMTH^3 * Di$	-290.000
$PMTH * Di$	-290.000
$PMTH^3 * Elevation$	-290.000
$PMTH * Elevation$	-300.000
$PMTH^3 * Di * Dc^3$	-2900.000
$PMTH * Di * Dc^3$	-2900.000
$PMTH^2$	-3000.000
$PMTH^2 * Dc^3$	-8100.000